

LEIBNIZ UNIVERSITY OF HANNOVER

FACULTY OF MATHEMATICS AND PHYSICS

Atomic Layer Deposition for High Power Laser Applications: Al_2O_3 and HfO_2

➤ Hao Liu

Atomic Layer Deposition for High Power Laser Applications: Al₂O₃ and HfO₂

Von der Fakultät für Mathematik und Physik
der Gottfried Wilhelm Leibniz Universität Hannover

zur Erlangung des Grades
Doktor der Naturwissenschaften
Dr. rer. nat.

Genehmigte Dissertation

von

M. E. Hao Liu

geboren am 27. März 1986 in China

2018

Referent:	Prof. Dr. Detlev Ristau
Koreferent:	Prof. Dr. Boris Chichkov
Tag der Promotion: 17.12. 2018	

Kurzzusammensassung

Optisch Stichten sind wesentliche Komponenten für optischen Systemen, um Licht zu reflektieren oder transmittieren. Die Laserkomponenten erfordern komplexere Eigenschaften von optische Schichten, wie z. B. genaue Dicke, Gleichmäßigkeit über große Fläche, geringe Absorption, hohe LIDT (Laser Induced Damage Threshold), kleine Spannung, hohe Filmdichte und so weiter.

Der ALD-Prozess wird untersucht, um Al_2O_3 und HfO_2 Schichten abzuscheiden. Die Filmeigenschaften wurden untersucht und mit IBS (Ion Beam Sputtering) Al_2O_3 und HfO_2 Schichten verglichen. Antireflexschichten für 1ω - 4ω des Nd: YAG lasers wurden mit ALD $\text{HfO}_2/\text{Al}_2\text{O}_3$ Doppelfilmschichten hergestellt. Die Antireflexschichten wurden charakterisiert und mit den Schichten verglichen, die mit IBS $\text{HfO}_2/\text{Al}_2\text{O}_3$ hergestellt wurden.

Sowohl ALD HfO_2 als auch Al_2O_3 haben Dicken mit hoher Auflösung aufgrund der selbstbegrenzten Eigenschaft. Dünne Schichten können durch Zählen der Zykluszahl gesteuert werden. Beide Schichten haben Gleichförmigkeit $>99\%$ in einem Bereich von 60 mm. Bei 1064 nm zeigen die ALD Schichten geringe Absorption um 3.7 ppm und ähnliche LIDT wie IBS-Filme. Annealing bei 300/400 °C erhöht die LIDT von ALD Al_2O_3 um 30%, aber erhöht nicht die LIDT von ALD HfO_2 . Für 1ω - 4ω des Nd: YAG lasers haben die ALD Antireflexschichten im Allgemeinen höhere LIDT als IBS Schichten. Die LIDT der Antireflexschichten ist durch die ALD HfO_2 Filmschicht begrenzt. Die Schädigung von sowohl ALD Einzelschichten als auch Antireflexschichten wird durch Defekte hervorgerufen.

ALD Filme, sowohl Einzelschichten als auch Mehrfachsichten, wiesen eine starke Zugspannung auf. Ein Modell für den Ursprung der Filmspannung wird erstellt. Unter Ausnutzung der hohen LIDT und Gegenspannung von ALD und IBS Schichten wurde ein Konzept vorgeschlagen, um hohe LIDT und kompensierte Spannung mit ALD Al_2O_3 und IBS SiO_2 zu entwickeln. Nach diesem Konzept wurde eine aus 4 Schichten bestehende Antireflexschichten hergestellt. Die kompensierte Spannung ist viel kleiner als entweder ALD Al_2O_3 oder IBS SiO_2 Einzelschichten. Die LIDT der Mehrfachsicht ist niedriger als die Einzelschichten aufgrund der Defekte, die während der Fortbewegung zwischen den ALD und IBS Beschichtungskammern eingeführt werden. Die Konzept hat Potenzial für Hochleistungslaserkomponenten, wenn eine geeignete Beschichtungsanlage erfunden wird.

ALD Schichten haben eine hohe Dichte und könnten daher als Deckschicht gegen Vakuum-Luft-Verschiebung in der Weltraumoptik verwendet werden, wenn sich die Umgebung ändert. Der Capping-Effekt von ALD Al_2O_3 auf aufgedampften $\text{Ta}_2\text{O}_5/\text{SiO}_2$ Multischichten wurde untersucht und diskutiert. Die Anwendung von ALD Schichten in Nanolaminaten und gechirpten Spiegeln wird diskutiert. Die Studie in dieser Arbeit zeigt die hohe Vielseitigkeit von ALD Schichten für Anwendungen in Hochleistungsbeschichtungen.

Stichworte: atomic layer deposition, Al_2O_3 , HfO_2 , Antireflexschichten, geringe Absorption, laser induced damage, Spannung, Filmdichte

Abstract

Optical coatings are essential components reflecting or transmitting light in optical systems. Laser components demand more complex properties of optical coatings, such as precise thickness, uniformity over large area, weak absorption, high laser induced damage threshold (LIDT), low stress, high film density and so on.

ALD process is investigated to deposit Al_2O_3 and HfO_2 thin films. The film properties are studied and compared to Ion Beam Sputtering (IBS) Al_2O_3 and HfO_2 single layer films. Anti-reflection coatings for 1ω - 4ω of Nd: YAG laser are prepared with ALD $\text{HfO}_2/\text{Al}_2\text{O}_3$ double layers. The anti-reflection coatings are characterized and compared to the coatings prepared by IBS $\text{HfO}_2/\text{Al}_2\text{O}_3$.

Both ALD HfO_2 and Al_2O_3 have thickness with high resolution due to the self-terminating feature. Thin films can be controlled by counting the cycle number. Both ALD films have uniformity >99% in $\phi 60$ mm area. At 1064 nm, the ALD single layer films show absorption as weak as 3.7 ppm, and similar LIDT compared to the IBS films. Annealing at 300/400 °C promote the LIDT of ALD Al_2O_3 by 30%, but does not promote that of ALD HfO_2 . For 1ω - 4ω of Nd: YAG laser, the ALD anti-reflection coatings have generally higher LIDT than IBS coatings. The LIDT of the ALD anti-reflection coating is limited by HfO_2 film layer. The damage of both ALD single layers and anti-reflection coatings are induced by defects.

ALD films, both single layers and multilayers, were found to have severe tensile stress. A model for the origin of the film stress is established. Taking advantage of the high LIDT and opposite stress of ALD and IBS films, a concept is proposed to develop high LIDT and stress compensated coatings with ALD Al_2O_3 and IBS SiO_2 . An anti-reflection coating consisting of 4 layers was prepared following this concept. The compensated stress is much smaller than either ALD Al_2O_3 or IBS SiO_2 single layer. The LIDT of the multi-layer is lower than the single layers because of the defects introduced during shift between the ALD and IBS coating chambers. This concept has potential application in high power laser components if a proper coating plant is developed to reduce the defects.

ALD films have high density, thus could be used as capping layer against vacuum-air-shift when the environment changes. The capping effect of ALD Al_2O_3 on evaporated $\text{Ta}_2\text{O}_5/\text{SiO}_2$ multilayers was studied and discussed. The application of

ALD films in nanolaminates and chirped mirror is discussed. The study in this thesis indicates the high versatility of ALD films for applications in high-power coatings.

Key words: atomic layer deposition, Al_2O_3 , HfO_2 , anti-reflection coating, weak absorption, laser-induced damage, stress, film density

Table of Contents

1. Introduction	1
1.1 Optical coatings.....	1
1.2 Requirements on modern optical coatings	1
2. Background	7
2.1 Mechanism of optical films	7
2.2 Current coating techniques	9
2.3 State of the art of Atomic layer deposition (ALD)	12
3. Experiment	21
3.1 Film deposition	21
3.2 Film characterization	23
4. Deposition of ALD Al₂O₃ and HfO₂	25
4.1 Growth kinetics of ALD.....	25
4.2 Parameters for the growth of ALD Al ₂ O ₃ and HfO ₂	30
4.3 Discussion.....	34
4.4 Problems encountered and solved.....	35
4.5 Summary.....	36
5. Characterization of ALD Al₂O₃ and HfO₂ single layers	37
5.1 Comparison of ALD and IBS Al ₂ O ₃ single layers.....	37
5.2 Comparison of ALD and IBS HfO ₂ single layers.....	45
5.3 Annealed ALD Al ₂ O ₃ and HfO ₂ single layers.....	51
5.4 Comparison of ALD Al ₂ O ₃ and HfO ₂ with commonly used films.....	56
5.5 Summary.....	59
6. ALD anti-reflection coatings for harmonics of Nd: YAG lasers	61
6.1 Coating design	61
6.2 Spectral characterization.....	61
6.3 Stress.....	63
6.4 Absorption.....	63
6.5 LIDT	63

6.6 Damage Morphology	65
6.7 Discussion.....	66
6.8 Summary.....	68
7. ALD Al₂O₃ acting as capping layer against vacuum-air-shift.....	69
7.1 Experiment.....	69
7.2 Results	70
7.3 Analysis.....	74
7.4 Summary.....	75
8. Stress compensated high power antireflection coatings.....	77
8.1 Introduction	77
8.2 Stress analysis of IBS and ALD coatings	78
8.3 Design of the stress-compensated AR coating	82
8.4 Experimental details	84
8.5 Results and analysis	84
8.6 Discussion.....	89
8.7 Conclusion	92
9. Other applications	93
9.1 Nanolaminates	93
9.2 GDD film	96
9.3 Conclusion	99
10. Summary and Conclusions.....	100
List of figures	102
List of tables.....	106
Reference	107
List of original publications	123
Appendix I – Damped harmonic oscillator	124
1. Solution of damped harmonic oscillator	124
2. Mean position of the oscillator	126
Declaration	128

Curriculum.....	129
Acknowledgements	130

1. Introduction

1.1 Optical coatings

Optical coatings are nowadays essential components in most optical systems. An optical coating is composed of one or more thin layers of material deposited on a substrate, usually a lens or mirror, to form a component which alters the way in which it reflects and transmits light.

Anti-reflection (AR) coating is one of the most widely used optical coatings. It reduces unwanted reflections at certain wavelength or wavelength range from an optical surface. According to the Fresnel's laws [1], fused silica has refractive index 1.46 at visible wavelengths, resulting in 4% reflection at each interface. If the system contains many transmitting optical elements such as a laser facility, applying an AR coating on each interface will increase the throughput of the system and reduce hazards caused by reflections.

More complex optical coatings are high-reflection (HR) coating, splitter, dichroic optical filter, band pass optical filter, and so on, which exhibit certain transmission or reflection over certain range of wavelengths.

The theory of optical coatings is based on Fresnel's laws, which govern the amplitude and phase of light reflected and transmitted at a single boundary [1]. Though thin metal films were known from very early times, optical coatings became rapidly developed since the 20th century. The invention of photography, telescopes and other optical systems brought a need for optical coatings. The introduction of oil diffusion pump paved the way towards vacuum deposition of optical coatings. Since then, tremendous strides have been made.

Modern optics without coating is unthinkable. It is almost impossible to imagine an optical instrument that would not rely on optical coatings to ensure its performance. Filters with more than 100 layers are not uncommon, and applications have been found for them in almost every branch of science and technology.

1.2 Requirements on modern optical coatings

According to the Fresnel Equations, the spectral property of an optical coating is dependent on the refractive index and optical thickness of each film layer composing the coating. The extinction coefficient of common dielectric material is omitted. Most

1.2. Requirements on modern optical coatings

of the optical materials exhibit very good stability in terms of refractive index. It is practical, therefore, for thin film designers to produce a design to meet a given spectral specification, once the coating materials have been chosen and their properties are known. However, there are still further difficulties to overcome in the construction of modern optical coatings, as listed in Table 1.

Table 1. Requirements on optical coatings of modern applications.

Precise thickness	High Uniformity	Low absorption	High LIDT	Low stress	High density
-------------------	-----------------	----------------	-----------	------------	--------------

1.2.1 Precise thickness

Precise thickness is one of the most important required properties as it determines the optical thickness, dominating the transmittance and reflectance according to the Fresnel equations. A systematic thickness error of several nm would lead to a shift of the spectrum, and a random thickness error would result in unpredictable spectral error.

Film thickness can be measured and controlled by different methods. The Quartz-Crystal Monitor (QCM) is one of the most widely used methods for coating depositions. QCM measures the change in resonance frequency of a slice of quartz crystal as the film deposits on its face and changes the total mass. QCM has an error about 2%, which is adequate for most optical coatings. Unfortunately, QCM measures mass but not optical thickness, it must be calibrated separately for each material used. Moreover, the sensitivity of the crystal decreases with increasing build-up of mass and the total amount of material is limited before the crystal becomes exhausted [2].

Optical monitoring (OM) consists of a light source illuminating a test substrate and a detector analyzing the reflected or transmitted light. It is the common method since the very beginning of coating history. Single-point monitoring was used for multilayer stacks where all the layers were quarter-waves, because the end of each layer corresponds to an extreme value in transmittance or reflectance. The error is usually 5% or better. Moreover, multilayers with non-quarter-wave layers are difficult to be monitored.

The modern method is made practical by advances in electronics and data analysis, that is, measuring the spectral characteristic with broad band monitor (BBM).

BBM could reach an accuracy as high as 0.5 nm [3][4]. High precision methods are still under development, as more complex coating designs are in pursue.

1.2.2 Uniformity over large aperture

It is of undoubting importance to deposit uniform layer over the area of the substrate. A flat plate held directly above the evaporating source, according to Holland and Steckelmacher's model [5], has a film thicker at the center than at the rim. The difference could be as large as 40%. This uniformity is not suitable for any accurate work unless the substrate is extremely small and in the center of the machine.

A number of techniques have been adopted to improve the uniformity.

In physical vapor deposition (PVD) processes, it is standard to maintain the pressure within the chamber sufficiently low to ensure a large free path of the evaporant molecules, which prevents the unpredicted collision of the evaporant molecules with air. An arrangement where the substrates lie on the surface of a sphere gives better uniformity. A higher degree of uniformity involves rotation of the substrate carrier. As the surface rotates, the thickness deposited at any point will be equal to the average of the thickness that would be deposited on a stationary substrate around a ring centered on the axis of rotation, provided always that the number of revolutions during the deposition is sufficiently great to omit an incomplete revolution. Another option is to adjust the height of substrate holder during deposition.

It is possible to make corrections to distribution by careful use of baffles in front of the substrates. The baffles are cut so that they modify the radial distribution of thickness. A further degree of freedom was introduced by reference [6] in the form of a rotating mask.

A synthetically application of the above techniques could produce uniformity larger than 99% over 600 mm substrate.

1.2.3 Weak absorption

Absorption is one kind of optical loss as the light passes the component, usually expressed in % or *ppm* (part per million). The lost energy is taken up typically by the electrons of an atom, and transformed into internal energy of the absorber, mostly thermal energy. Optical coatings consisting of dielectrics often have distinctively weaker absorption than those containing metal layers. A typical dielectric mirror working at 1064 nm has absorption on the scale of ppm.

1.2. Requirements on modern optical coatings

However, the remaining absorption might cause severe problems, thus extremely low loss (below 1 ppm) is demanded in high-precision optical systems such as: the gyroscopic ring laser [7], the laser interferometer gravitational-wave observatory (LIGO) [8], the cavity ring-down spectroscopy [9], atomic clock [10], and so on.

1.2.4 High LIDT

Since the very beginning of laser history, scaling the laser output has been one of the main goals of laser development. Nowadays, a typical CO₂ laser working at wavelength 10.6 μm has power up to 20 kilowatt [11]. As to fiber lasers at wavelength 1080 nm, output power as high as several kilowatt is commercially available [12]. By use of pulse compressing techniques, commercial fiber lasers can output femtosecond pulses with peak power over 50 megawatt [13]. The largest and most energetic laser in the world today, the NIF (National Ignition Facility), is configured to deliver nanosecond pulse with an energy of 1.8 mega Joule into a 600 μm target [14]. The growing laser power has contributed to a number of industries such as: cutting and welding materials, 3D-printing, fiber-optic and free-space optical communication, laser surgery and skin treatments, etc. The pursuit of higher laser power is far from coming to an end.

However, the continuously growing power causes damage problems in the optical components that compose or deliver the laser. Optical coatings are one of the most fragile components that set an upper-limit of the laser power. A large number of papers have been reported studying the laser induced damage of optical thin-films [15]. An annual symposium dedicated to laser induced damage is held in Boulder, Colorado since 1968.

The laser resistant capability of a coating is usually described by laser induced damage threshold, expressed in J/cm^2 . The cause of laser damage in optical thin films is complex. Factors such as film stoichiometry, microstructure, crystalline structure, composition, defects from electronic to micron size, and band gap energy can all play a role in laser damage [16]-[19]. Promoting the laser resistance of optical coatings is a continuing challenge, because as new laser-damage resistant optical materials and fabrication technologies are developed, laser designers increase the system operating energies and powers to the limits of the components.

1.2.5 Low stress

Stress is the force σ per unit area that is acting on a surface of a solid, more commonly expressed in Pascals (Pa) or N/m^2 . Optical coatings are generally in a state of elastic mechanical stress during and after deposition. Without the application of externally imposed forces, the coating stress is characterized as an internal or residual stress. Residual stress can be compressive, which makes the film expand parallel to the surface, or tensile, which makes the film shrink. The substrate, however, prevents the expansion or shrink of the film. The equilibrium of forces and bending moments causes the substrate to bend convex or concave, which will be discussed in chapter 8 in detail.

The bending of optical components would cause distortion to the wave-front of beam passing through it, which is not favored in high-precision systems [20][21]. Apart from the wave-front distortion, cracking of a film or layer is possible when tensile stress develops, while buckling-driven delamination can occur if compressive stress accumulates [22]. Coatings with little stress or ways to mitigate the stress are desired.

1.2.6 High film density

Optical coatings with high density are desired as the porous microstructures are often found in traditionally evaporated films. The pores adsorb H_2O from the environment atmosphere, leading to a shift of the spectral response of the coating if the environment changes, named as vacuum-air-shift. The impacts caused by the vacuum-air-shift can be significant on instruments such as Doppler Wind Lidar [23][24]. The adsorption of H_2O in porous coating is also accompanied by changes in the stress level [25] and laser induced damage threshold [26]. It is clear that coatings in space should be fully densified to avoid the vacuum-air-shift.

1.2.7 Summary

The requirements on optical coatings of modern applications are summarized in Table 1. In particular applications, one or several among the requirements are demanded. For example, precise thickness and uniform film layers are generally required by most optical systems. The high power lasers need components with LIDT as high as possible, and low stress is always needed simultaneously for a better wavefront [27][28]. The space-borne applications emphasize on high density and

1.2. Requirements on modern optical coatings

high LIDT specifically [23]. The gravitational wave detectors need coatings with extremely low absorption [8]. It is promising to study all the characteristics concerning a new coating process.

In this thesis, the mechanism of optical coatings and general coating techniques are described in chapter 2. Atomic layer deposition (ALD) is studied to deposit Al_2O_3 and HfO_2 in chapter 3 and 4. The film properties concerned in Table 1 are studied in chapter 5 and compared to the IBS Al_2O_3 and HfO_2 single layer films. Anti-reflection coatings for Nd: YAG laser are prepared with ALD $\text{Al}_2\text{O}_3/\text{HfO}_2$ and studied in chapter 6 in comparison with IBS coatings. The application of ALD Al_2O_3 as capping layer is analyzed in chapter 7. A novel concept for developing high LIDT and compensated stress coatings is proposed in chapter 8.

2. Background

2.1 Mechanism of optical films

Optical materials are different from free space because they have a certain refractive index. The refractive index is defined as the ratio of the velocity of light in free space c and the velocity of light in that material v , denoted by N .

$$N = c / v = n - ik \quad (1)$$

Where n is the real part of refractive index (or often simply refractive index for most dielectric materials), and k the extinction coefficient. N is a function of wavelength.

Light can be described as electromagnetic wave. A plane, monochromatic light wave can be expressed as:

$$E = \exp\left[-\frac{2\pi k}{\lambda} z\right] \exp\left[i\left(\omega t - \frac{2\pi n}{\lambda} z\right)\right] \quad (2)$$

Where z is the distance along the direction of propagation, E the electric field and λ the wavelength of that light in free space. The extinction coefficient k is a measure of absorption in the medium. It is related to absorptance in the form $\alpha = 4\pi k / \lambda$.

At a boundary between two media, denoted by suffix 0 for the incident medium and by suffix 1 for the exit medium, the light beam can be either reflected, transmitted or lost by absorption, as indicated in Fig. 1. Scattering is a loss due to the roughness of the boundary, not considered here.

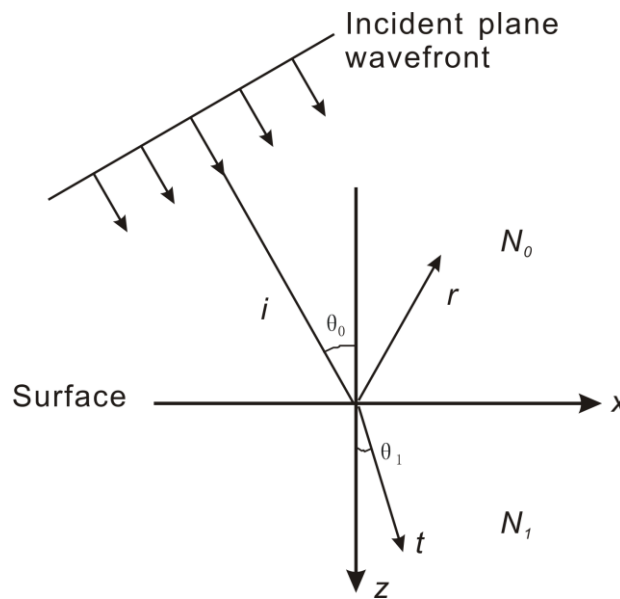


Fig. 1. Plane wavefront incident on a single surface.

The incident angle θ_0 and refractive angle θ_1 are governed by Snell's law.

$$N_0 \sin \theta_0 = N_1 \sin \theta_1 \quad (3)$$

The optical admittance of a material is defined as the ratio of the magnetic and electric fields. For the oblique incidence, the light is usually split into two linearly polarized components, TM for transverse magnetic field (p -polarized) and TE for transverse electric field (s -polarized). The tilted optical admittance η is given by:

$$\begin{aligned} \eta_p &= \frac{Ny_0}{\cos \theta} \\ \eta_s &= Ny_0 \cos \theta \end{aligned} \quad (4)$$

Where y_0 is the optical admittance in free space, with value $y_0=2.6544 \times 10^{-3} \text{ A}^2 \text{ s}^3 / \text{kgm}^2$, and N and θ denote either N_0 and θ_0 or N_1 and θ_1 as appropriate.

The reflection coefficient ρ and transmission coefficient τ of electric field on the boundary surface are governed by **Fresnel Equation**:

$$\begin{aligned} \rho &= \frac{|E_r|}{|E_i|} = \frac{\eta_0 - \eta_1}{\eta_0 + \eta_1} \\ \tau &= \frac{|E_t|}{|E_i|} = \frac{2\eta_0}{\eta_0 + \eta_1} \end{aligned} \quad (5)$$

The phase shift experienced by the wave as it propagates a distance d normal to the interface is given by:

$$\delta = \frac{2\pi}{\lambda} Nd \cos \theta_0 \quad (6)$$

For optical coatings with an assembly of interfaces, the reflectance is calculated through the concept of optical admittance. The multilayer is replaced by a single surface, which presents an admittance Y that is the ratio of the total tangential magnetic and electric fields and is given by:

$$Y = C / B \quad (7)$$

Where B and C are calculated by the **characteristic matrix**:

$$\begin{bmatrix} B \\ C \end{bmatrix} = \left\{ \prod_{r=1}^q \begin{bmatrix} \cos \delta_r & (i \sin \delta_r) / \eta_r \\ i \eta_r \sin \delta_r & \cos \delta_r \end{bmatrix} \right\} \begin{bmatrix} 1 \\ \eta_m \end{bmatrix} \quad (8)$$

η_m is the optical admittance of the substrate, q is the number of film layers.

Provided the real η_0 of the incident medium, the reflectance and transmittance are:

$$R = \left(\frac{\eta_0 B - C}{\eta_0 B + C} \right) \left(\frac{\eta_0 B - C}{\eta_0 B + C} \right)^* \quad (9)$$

$$T = \frac{4\eta_0 \operatorname{Re}(\eta_m)}{(\eta_0 B + C)(\eta_0 B + C)^*}$$

Equations (3)-(9) are essential to calculate the spectrum of a multilayer coating, and the fundamental for an optical coating design. Despite the apparent simplicity of the characteristic matrix, numerical calculations without some automatic aid are tedious in the extreme. Extended calculations are carried out with a program in this dissertation.

2.2 Current coating techniques

There are a considerable number of processes for the deposition of optical coatings. The most common processes take place under vacuum and can be classified as Physical Vapor Deposition (PVD). In these processes, the thin film condenses directly in the solid phase from vapor. The PVD processes can be further classified by the methods for producing the vapor phase. Another technique complementary to PVD is named as Chemical Vapor Deposition (CVD), in which the growing film is formed by a chemical reaction between precursors. The typical coating techniques are summarized in Table 2 followed by a description.

Table 2. Assessment of optical coating techniques.

	thickness monitor dependent	uniformity correction dependent	deposition rate	stress	film density
EBE	√	√	1-10 nm/s	tensile	poor
IAD	√	√	1-10 nm/s	controllable	good
IBS	√	√	0.1-1 nm/s	compressive	high
MS	√	√	0.5-1 nm/s	compressive	high
Sol-gel	process dependent	-	~100 nm/cycle	tensile	poor
PECVD	√	√	5-10 nm/s	controllable	good

Electron beam evaporation (EBE) is presently the most popular technique for optical coatings, in which the vapor is produced by heating the film material (or evaporant) locally with electron beam. The typical energies of evaporated molecules

are a few tenths of electron volt (eV). A large number of materials can be EBE deposited. The deposition rate can be 1 nm/s to several tens nm/s. The film thickness is monitored by either OM or QCM, and each layer is ended by shielding the evaporating source. The error of thickness depends on the monitor as well as the stability of evaporation. Usually an error within 5 nm is achieved. The uniformity over 99% on meter-scale flat substrates is guaranteed by lying them on the surface of a sphere, rotating the substrates, adjusting the height of substrates and further corrected by careful use of baffles in front of the substrates.

The main restrictions of EBE coatings are the stress and the columnar microstructures caused by the limited surface diffusion rate of the film molecules [29]. The columnar pores are adsorptive to moisture, therefore leading to vacuum-air-shift when environmental conditions are changed.

Ion beam assisted deposition (IAD) is a technique which combines the evaporated films with bombardment of a beam of energetic ions. The major benefit of the IAD energetic process is an increase in film molecule energy. It makes the film more bulk-like, improves film adhesion, reduces the moisture sensitivity and reduces the sometimes quite high tensile stress in the layers. The main disadvantage with IAD is the many processing parameters that must be controlled [30]-[34].

Magnetron Sputtering (MS) is another vapor deposition process, in which the target material is negatively charged and bombarded by the positively charged ions. The ions strike the target with energies hundreds of eV and eject atoms from it. The atoms form the vapor and condense on surfaces that are placed in proximity to the magnetron sputtering cathode. The MS films have higher density than EBE coatings. The main disadvantage is "target poisoning". The metallic target surface is oxidized, storing charge like a capacitor and breaks down as an arc. This arcing tends to produce molten droplets of material that are often embedded in the film [35].

Ion Beam Sputtering (IBS) uses a separate chamber to generate the ions that are then extracted and directed toward the target. It does not have the "poisoning" problem as in magnetron sputtering. The mobility of the IBS atoms is as high as several 10 eV [36]. The IBS atoms have large diffusion rate, forming an amorphous film with low loss, high density and stability. High reflecting mirrors produced with the IBS process can reach total losses about 1 ppm corresponding to a reflectivity of 99.999% at 1064 nm [37][38]. The IBS coatings were found to have

superior LIDT to EBE for 355 nm ns laser according to the damage competition held by SPIE in 2017 [39].

A further advantage of IBS process is the stable and rather slow rate compared to EBE. The depositing rate of IBS is typically 0.1 nm/s, therefore enables a precise control of film thickness if the monitor has enough precision. Complex coating designs such as rugate filters could be achieved by IBS [40]. IBS, however, is restricted in large components applications due to its non-uniformity and compressive stress problems [36].

Sol-gel process is a wet-chemical technique in which the sol (or solution) evolves gradually towards the formation of a gel-like network containing both liquid and solid phase. Sol-gel porous SiO₂ has lower refractive index ($n=1.22$ at 1064 nm) than substrate, and rather high LIDT among the available optical coatings [41]. Therefore, Sol-gel SiO₂ is mainly used as single layer anti-reflection coatings in high power lasers [41]-[44]. Sol-gel high-reflectors are not often used, though ZrO₂ can be Sol-gel fabricated. The main reason lies in the severe tensile stress of the Sol-gel process. Sol-gel films thicker than 500 nm are often reported to craze [45]. The film thickness of Sol-gel ZrO₂ is difficult to control, and the LIDT decreases tremendously as the layer number increases [46].

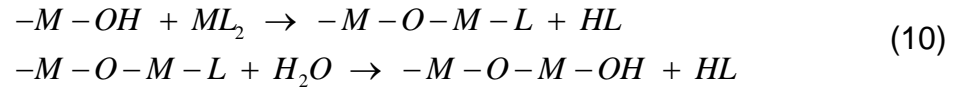
Plasma enhanced chemical vapor deposition (PECVD) produces coatings through chemical reaction amongst components of the vapor that surrounds the substrates. The binding of film molecules are enhanced by plasma so that the film is tough, hard and dense [47]. The film stress can be decreased from tensile to compressive as the ion bombarding energy increases. The main disadvantage of PECVD is the non-uniformity and un-precise thickness control, resulting in a spectral error when applied in optical coatings [48].

In general, PVD generates film adatoms or molecules through energy transfer while Sol-gel and PECVD produce film molecules by chemical reaction. The PVD as well as PECVD depositions are consecutive and most times inhomogeneous, therefore the film thickness needs to be monitored and the uniformity needs to be corrected. The film density and stress are highly related to the kinetics of the film molecules, and this would be further analyzed in chapter 8.

2.3 State of the art of Atomic layer deposition (ALD)

2.3.1 Introduction of ALD

Atomic layer deposition (ALD) is a film depositing technique based on the sequential use of self-terminating gas-solid reactions. The film layer is formed through exchange reactions between functional groups of precursors as illustrated in equation (10):



Where M represents metal and L ligand, respectively. MO such as Al_2O_3 , HfO_2 , TiO_2 , SiO_2 are the film molecules. The ligands can be $-CH_3$, $-CH_2CH_3$, $-Cl$, amino, and so on. ML_2 is usually called precursors. H_2O , O_3 or other oxidants are called reactants.

The growth of ALD film is illustrated in Fig. 2.

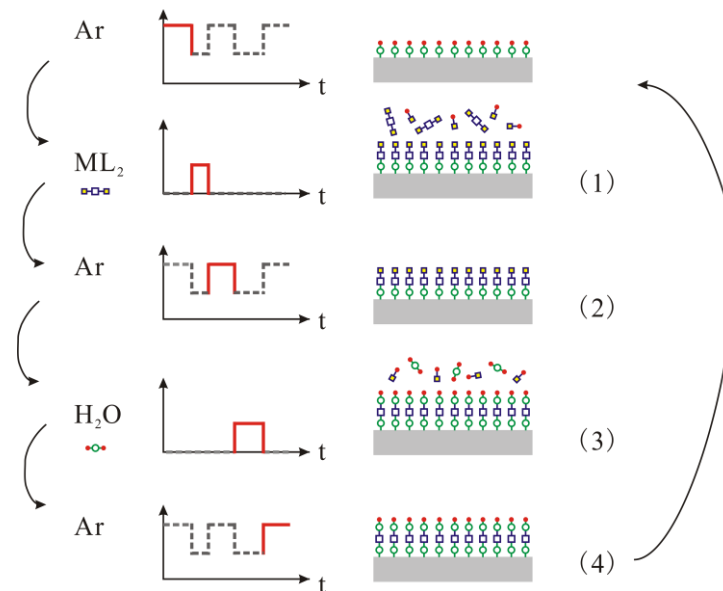


Fig. 2. Schematic of an ALD cycle. (1) exposure of precursor; (2) purging; (3) exposure of reactant; (4) purging.

One typical cycle of ALD consists of the following four steps:

- (1) Exposure of the precursor ML_2 ;
- (2) Purging;
- (3) Exposure of the reactant;
- (4) Purging.

Each cycle adds a certain amount of material to the surface, referred to as the growth per cycle (GPC). To grow a material layer, hundreds of reaction cycles are repeated until the desired amount of material has been deposited.

2.3. State of the art of Atomic layer deposition (ALD)

Due to the finite number of surface sites, each of the half reactions can only deposit a finite number of surface species, which is the **self-terminating** feature of ALD. One advantage of ALD resulting from the self-terminating feature is the *precise thickness* control at sub-nanometer level without thickness monitoring. The excessive precursors will desorb from the surface areas where the reaction has reached completion. Another advantage is the *uniform and pinhole-free* films over large substrate. The ALD precursors are gas phase molecules, and they fill all space independent of substrate geometry and do not require line-of-sight to the substrate. ALD films remain extremely smooth and conformal to the original substrate, because the reactions are driven to completion during every reaction cycle.

The main disadvantage of ALD is its slowness. In terms of a thickness increment per time unit, the growth rate of 0.01 nm/s is typically achieved by ALD, much smaller than other techniques listed in Table 2.

2.3.2 Mechanism of ALD

The film growth of ALD is based on the adsorption of precursor molecules. Adsorption can be generally divided into two classes on the basis of the strength of interaction between the adsorbing molecule and the solid surface: Physi-sorption and Chemi-sorption.

Physi-sorption originates from weak interactions, with minimal changes in the structure of the adsorbing molecule-surface pair. The fundamental interacting force of physi-sorption is caused by the Van-der-Waals force, the interaction energy of which is about ~0.01-0.1 eV. Van-de-Waals forces originate from the interactions between induced, permanent or transient electric dipoles. Physi-sorption is always reversible, because the thermal energy at room temperature is about 0.026 eV.

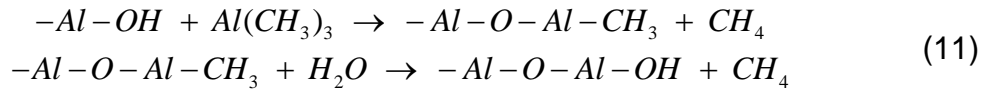
Chemi-sorption, in turn, involves the creation and optional breaking of chemical bonds. New chemical bonds are generated at the adsorbent surface. Chemi-sorption is characterized by much higher binding energies than the environmental thermal energy, and is therefore in general irreversible.

The chemi-sorption is essential for a stable ALD film, though both physi-sorption and chemi-sorption may be involved in the process. It is desired to annihilate the physi-sorption, as illustrated in the kinetics in chapter 4.

One of the studies that verify the chemi-sorption in ALD is the work of Ferguson [49]. In the experiment, the ALD deposition of Al_2O_3 using TMA ($\text{Al}(\text{CH}_3)_3$,

2.3. State of the art of Atomic layer deposition (ALD)

trimethylaluminium) and H₂O was monitored with an in-situ Fourier transform infrared spectroscopy (FTIR). The FTIR measured the transmission in a wavenumber range 500-4000 cm⁻¹ (wavelength 2,500-20,000 nm). After the exposure of TMA, the H-O-H feature at 3000-3711 cm⁻¹ was found to decrease, and the C-H feature at 2800-3000, 1464 and 1216 cm⁻¹ was found to increase. The opposite was observed after the exposure of H₂O. The consumption and introduction of reactive ligands certified the chemi-sorption as in equation (10), to be more specific, as following:



The work of Tsai verified the importance of functional groups on substrate surfaces in ALD Al₂O₃ deposition [50]. In the experiment, Si substrates terminated with -H, -N, and -OH were used for depositing Al₂O₃ film. A smooth, conformal atomic layer was found on the -OH terminated surface. In contrast, 30-40 cycles were required before the nucleation of ALD occurred on the -H or -N covered substrates. These experiments indicated the importance of chemi-sorption in ALD.

Widjaja investigated the thermochemistry and kinetics of the TMA and H₂O half reactions on the Al₂O₃ surface [51]. According to the potential energy surface of his results, the reaction of TMA and H₂O was about 1.5 eV exothermic. Chen investigated the kinetics of the TEMAH (tetraethylmethylaminohafnium, Hf[N(CH₃)₂]₄) and H₂O half reactions on the HfO₂ surface [52]. The conclusion was that the reaction of TEMAH and H₂O was about 1.1 eV exothermic. These studies supported the chemi-sorption in ALD.

2.3.3 ALD history and application in microelectronics

According to the commonly acknowledged origin, ALD was developed under the name "atomic layer epitaxy (ALE)" in Finland by Suntola and co-workers in 1977 [53]. In the patent [54], ALD growth was demonstrated for Zn/S process to grow ZnS, Sn/O₂ process to grow SnO₂, and Ga/P process to grow GaP [55][56]. Not until 1990s was the name "Atomic layer deposition (ALD)" commonly adopted over the world.

The original application of ALD was to control the precise growth of dielectric oxides for thin film electroluminescent (TFEL) displays [53][57]. The electroluminescent material emitted light in response to a strong electric field. ALD produced TFEL showed outstanding electrical and optical characteristics. The high

2.3. State of the art of Atomic layer deposition (ALD)

dielectric strength of the dielectrics, with an intrinsic pinhole-free feature, allowed effective excitation of the light-emitting ZnS: Mn layer. Reasonably high productivities could be achieved in spite of the low growth rates because of the large-batch/large-area capability [58].

Following the successful introduction of ALD, a great deal of research effort has been devoted to extending its use to other materials and applications such as MOSFET (metal oxide semiconductor field effect transistor) devices. ALD Al_2O_3 had suitable properties as a gate material such as high dielectric constant, low leakage current, high thermal stability and good interfacial property with Si, therefore gained promising application on miniaturizing the size of MOSFET [59]-[64]. Other high dielectric constant materials such as ZrO_2 , HfO_2 , Y_2O_3 , HfSi have been studied for applications as future CMOS (complementary metal oxide semiconductor) gate dielectrics [65]-[73].

Reference [55] has summarized the inorganic materials grown by ALD. Oxides have been grown for alkaline-earth metals, transition metals including lanthanoids, and group 13-15 elements. The reactants in oxide deposition has most typically been H_2O , or somewhat less often O_2 , O_3 , alcohols ROH, or O created through oxygen plasma. Nitrides have analogously most often been manufactured from the metal compound and ammonia NH_3 ; sulphides from hydrogen sulphide H_2S ; selenides from hydrogen selenide H_2Se ; and tellurides from Te. Some successes have also been booked in the deposition of pure elements, such as Tungsten.

2.3.4 ALD for optical coatings

Optical coating is one of the applications where the benefits of ALD make it a potential alternative to the presently used techniques. The basic requirements for optical films, precise thickness and sharp parallel interfaces, are well met by ALD. The fundamental properties of some ALD films have been reported, and summarized in Table 3. The materials are listed in decreasing order of refractive index. The transmittance region, precursors involved, growth temperature as well as the reported crystallinity are given. The properties of thin films are highly influenced by the deposition processes and the growth temperature. Therefore refractive indices given in Table 3 are meant only as guidance values. Detailed information is found from references included in the table.

2.3. State of the art of Atomic layer deposition (ALD)

Table 3. Part of ALD materials for optics.

Material	Transmit range (μm) from Ref.[1]	Precursor + reactant	Growth T ($^{\circ}\text{C}$)	Refractive index ($\lambda \sim 550\text{-}640 \text{ nm}$)	Film Structure	Ref.
TiO_2	0.35-12	$\text{TiCl}_4 + \text{H}_2\text{O}$	100-600	2.3-2.8	amorphous ($<140^{\circ}\text{C}$) polycrystalline ($>140^{\circ}\text{C}$)	[74]- [82]
Nb_2O_5	0.38-8	$\text{Nb}(\text{OC}_2\text{H}_5)_5 + \text{H}_2\text{O}$	150-300	2.2-2.4	amorphous	[83]
ZrO_2	0.34-12	$\text{ZrCl}_4 + \text{H}_2\text{O}$	150-500	2.2	amorphous	[84]
		$\text{Zr}[\text{OC}(\text{CH}_3)_3]_4 + \text{H}_2\text{O}$	150-300	2.0	crystallized	[85]
		$\text{ZrI}_4 + \text{H}_2\text{O}/\text{H}_2\text{O}_2$	250-500	2.1-2.2	crystallized	[86]
ZnS	0.38-25	$\text{ZnCl}_2 + \text{H}_2\text{S}$	320-500	2.3	crystallized	[87]
Ta_2O_5	0.3-10	$\text{TaCl}_5 + \text{H}_2\text{O}$	80-500	1.9-2.2	amorphous ($<300^{\circ}\text{C}$) crystallized ($>300^{\circ}\text{C}$)	[88]
Si_3N_4	0.32-7	$\text{SiCl}_4 + \text{NH}_3$	227-627	2.0	-	[89]
HfO_2	0.22-12	$\text{HfCl}_4 + \text{H}_2\text{O}$	500	2.1	monoclinic	[90]
		$\text{Hf}[\text{NCH}_3\text{C}_2\text{H}_5]_4 + \text{H}_2\text{O}$	150-325	2.1	amorphous ($<200^{\circ}\text{C}$) monoclinic ($>200^{\circ}\text{C}$)	[91]
		$\text{Hf}(\text{OCMe}_2\text{CH}_2\text{OMe})_4 + \text{H}_2\text{O}$	275-425	1.8-2.0	monoclinic	[92]
Sc_2O_3	0.35-13	$\text{Sc}(\text{C}_{11}\text{H}_{19}\text{O}_2)_3 + \text{O}_3$	175-500	2.0	crystalline	[93]
		$(\text{C}_5\text{H}_5)_3\text{Sc} + \text{H}_2\text{O}$			crystalline	
Y_2O_3	0.25-12	$\text{Y}(\text{C}_{11}\text{H}_{19}\text{O}_2)_3 + \text{O}_3$	200-425	1.7-1.9	amorphous ($<250^{\circ}\text{C}$) monoclinic ($>250^{\circ}\text{C}$)	[94]

2.3. State of the art of Atomic layer deposition (ALD)

ITO	0.4-1.5	$\text{InCl}_3 + \text{SnCl}_4$ + H_2O	300-500	1.8-1.9	crystallized	[95] [96]
La_2O_3	0.35-2	$\text{La}[\text{N}(\text{SiMe}_3)_2]_3$ + H_2O	150-250	1.6-1.9	amorphous	[97]
Al_2O_3	0.2-7	$\text{Al}(\text{CH}_3)_3$ + H_2O	100-300	1.6	amorphous	[98]
SiO_2	0.2-8	$\text{HSi}[\text{N}(\text{CH}_3)_2]_3$ + O_2 plasma	200	1.46	amorphous porous	[99]- [101]
		$\text{HSi}[\text{N}(\text{C}_2\text{H}_5)_2]_3$ + O_2 plasma				
CaF_2	0.15-12	$\text{Ca}(\text{C}_{11}\text{H}_{19}\text{O}_2)_2$ + TiF_4	300-450	1.43	crystallized	[102]
MgF_2	0.21-10	$\text{Mg}(\text{C}_{11}\text{H}_{19}\text{O}_2)_2$ + $\text{TiF}_4/\text{TaF}_5$	250-400	1.34-1.42	column structure	[103] [104]

The deposition of Al_2O_3 is one of the most representative processes for ALD, because of the high volatility and reactivity of precursors $\text{Al}(\text{CH}_3)_3/\text{H}_2\text{O}$, the thermally stable reaction and the rather safe by-product methane.

HfO_2 is a widely used material in laser applications due to its high refractive index and power handling capability. Aarik has investigated the influence of substrate temperature on ALD HfO_2 films, concluding that the film grown at 225 °C was amorphous, and that grown at 500 °C was monoclinic, had about 5% higher refractive index but more than an order of magnitude higher optical losses [90][105]. HfO_2 films grown at 880-940 °C had cubic phase due to crystallization [106].

ALD growth of TiO_2 has been studied by using various precursors [75]-[81], among which TiCl_4 was mostly reported. In TiO_2 ALD using TiCl_4 and H_2O , the by-product HCl was corrosive and toxic. TiO_2 films grown below 140 °C were amorphous while above 165 °C were anatase crystallized. Films containing anatase as well as rutile were grown at temperatures above 350 °C while containment of rutile was significantly increased with increasing growth temperature [77][82].

Ta_2O_5 is another widely studied material with high dielectric constant and chemical stability [107]-[109]. Kukli has studied ALD Ta_2O_5 film deposited with TaCl_5 and H_2O at different substrate temperatures [110]. The films deposited below 300 °C were predominantly amorphous, whereas those grown at higher temperatures were polycrystalline. The optical band gap was close to 4.2 eV for amorphous films.

2.3. State of the art of Atomic layer deposition (ALD)

SiO₂ was a desirable material for optical application, but only was grown successfully through ALD recently [99]-[101]. The precursors were HSi[N(CH₃)₂]₃ and O₂ plasma. The 300 nm SiO₂ film exhibited absorptance as low as 1.5 ppm at wavelength 1064 nm, however, the film seemed to have porous structure. Details are still under investigation.

The first ALD experiments on optical multilayers were ZnS and Al₂O₃, which were grown from the corresponding chlorides ZnCl₂/AlCl₃ and reactants H₂S/H₂O [58][87]. ZnCl₂ and AlCl₃ were evaporated from open boats held at 350 °C and 90 °C respectively, inside the reactor. They were pulsed by means of inert gas valving. The films were grown on glass substrates at 500 °C using 0.2 and 0.5 s exposure and purging sequences respectively. A high reflection coating with nine-layer structure (HL)⁴H/glass and a Fabry-Perot filter with 20-layer structure (HL)⁵-(LH)⁵/glass were prepared. The measured reflectance spectra of the high reflection coating matched the calculation well, while severe differences were observed between the measured and ideal spectra in the side band regions of the Fabry-Perot filter. The deviations were analyzed to be caused mainly by thickness variations in the uppermost layers. They attributed the thickness variation to the decreasing vapor pressure as the precursors were consumed.

Szeghalmi et al. has investigated ALD TiO₂/Al₂O₃ Narrowband Pass Filters (NBPF) centered at adjacent wavelengths [111]. The precursors applied were Al(CH₃)₃, Ti[OCH(CH₃)₂]₄, and H₂O. The filter was made of 15 layers of the H(LH)³(2L)(HL)³H type. Several conclusions have been drawn in their report. (1) Precise thickness control without *in-situ* control and good uniformity could be achieved with ALD, and further improvement was also possible; (2) The substrate material had a significant effect on the initial "seed" film, therefore the linear fit ($t=y+N*g$) of the film thickness (t) versus number of cycles (N) showed a considerable variation as large as 5 nm for the y-intercept values; (3) The bottom layers had a lower thickness than the corresponding upper ones, indicating the influence of the seed material on the growth rate.

Pfeiffer et al. deposited a double-sided broadband anti-reflection coating on N-SF8 glass with ALD HfO₂/SiO₂ [99]. The precursors involved were Hf[N(CH₃)₂]₄ + H₂O, and HSi[N(CH₃)₂]₃ + O₂ plasma. An average transmittance of 97% in a wavelength range from 390-1100 nm was demonstrated. Taking advantage of the uniformity of

2.3. State of the art of Atomic layer deposition (ALD)

ALD, they deposited anti-reflection coatings on hemispherical lens and aspherical lens [112]. The average reflectance was less than 0.3%. These results demonstrated that ALD was a promising technology for deposition of uniform optical layers on strongly curved lenses without complex in situ thickness monitoring.

Wei has studied anti-reflection coatings deposited with ALD TiO_2 and Al_2O_3 [113]. TiCl_4 , $\text{Al}(\text{CH}_3)_3$ and H_2O were used as precursors. Crystallinity was proven with the coatings deposited at 280 °C. The Nd:YAG laser damage was characterized at 1064 nm. The LIDT was found to be about 6.5 J/cm^2 with mainly peeling off morphology.

Li has presented the idea of depositing rugate Notch Filter using ALD TiO_2 and Al_2O_3 [114]. The main concept was to equivalent three thin layers as a single layer according to Herpin's theorem [115]. The refractive index could be adjusted by the thickness of the single layers. A rugate notch filter has been fabricated, though not much characteristics were discussed.

Jensen et al. has studied the power handling capability of ALD coatings consisting of TiO_2 and Al_2O_3 [116]. The precursors were TiCl_4 , $\text{Al}(\text{CH}_3)_3$ and H_2O , the process temperature was 280 °C, which was above the crystallizing temperature [77]. Both the high-reflection coatings and TiO_2 single layers exhibited large scattering and absorption (>900 ppm). Al_2O_3 single layer had much better optical characteristics with absorption 10-20 ppm (1064 nm laser) and LIDT of more than 20 J/cm^2 . In contrast, TiO_2 has LIDT of about 6 J/cm^2 . While crystallization might be one of the main causes of poor power handling capability, TiO_2 was considered not proper for high power laser applications. Wei has studied the laser damage property of ALD $\text{HfO}_2/\text{Al}_2\text{O}_3$ anti-reflection coating at 1064 nm, which was $14\text{-}18 \text{ J/cm}^2$ [117][118].

2.3.5 Summary

ALD has been successfully applied since its invention to fields such as microelectronics. The main advantage lies in its self-terminating process, which leads to thickness control without in-situ monitor and uniformity over large area, even on curved surfaces. It has also potential in optical applications. A number of papers have reported the fundamental properties such as refractive indices of ALD materials. However, the application of ALD coating in high power lasers is rarely reported.

Among the materials mentioned in Table 3, Al_2O_3 and HfO_2 have great potentials due to the safe by-products and controllable process. A full investigation is needed to

2.3. *State of the art of Atomic layer deposition (ALD)*

clarify their properties concerned in Table 1 and the application probabilities in high power lasers.

3. Experiment

3.1 Film deposition

ALD Al_2O_3 and HfO_2 were studied. The precursors involved were H_2O , TMA (Trimethylaluminum, $\text{Al}(\text{CH}_3)_3$, Dock Chemicals, Germany), and TEMAH (Tetraethylmethylaminohafnium, $\text{Hf}[\text{N}(\text{CH}_3\text{CH}_2\text{CH}_3)_2]_4$, Pegasus, UK). The deposition was carried out in a system (Aviza Pantheon Mainframe CVD304) illustrated in Fig. 3 (a). Two modules have been used in the experiments. The 1st module was built for ALD Al_2O_3 only, while the 2nd was built for depositing Al_2O_3 and HfO_2 simultaneously. The Al_2O_3 deposited in the 1st module was used for characterization and GDD study, while in the 2nd module was used for multilayer studies.

The precursors were in the bubblers and carried into the chamber by Ar. Ar was used as both carrier gas and purging gas. High-precision valves were employed to control the Ar flow rate, flow time, and flow path, either through precursor bubblers or directly into the chamber. The chamber pressure was maintained at 140 Pa by keeping the gas flow constant. The gas flow of the four steps in an ALD cycle (Exposure, purging, exposure and purging) for Al_2O_3 or HfO_2 is illustrated in Fig. 3 (b).

The valve systems for H_2O and TEMAH are illustrated in Fig. 3(c). TMA has similar valves to TEMAH and is therefore not displayed here for clarity. A different composition of valves was open in each step to form a gas flow path. The detailed composition for each step is listed in Table 4. The design of composition could keep the chamber pressure unchanged during step shift, which is essential for a stable ALD process. The Ar flowed into the chamber through the pipes. A shower head allocated the flow symmetrically onto the substrate surface.

Table 4. Valve recipes for an ALD HfO_2 cycle.

	Open valves
purging	V1 , V4, V5, V7, V13, V10, V12, V23
TEMAH exposure	V29, V31, V32 , V4, V5, V7, V13, V10 , V12, V23
H_2O exposure	V1, V4, V5, V7, V13, V9, V11 , V12, V23

Single layers were deposited on Si substrate for thickness measurement and elemental characterization. Fused silica substrates were used for characterizations

3.1. Film deposition

including transmission and reflection spectrum, deep-UV spectrum, stress, laser absorption and laser damage.

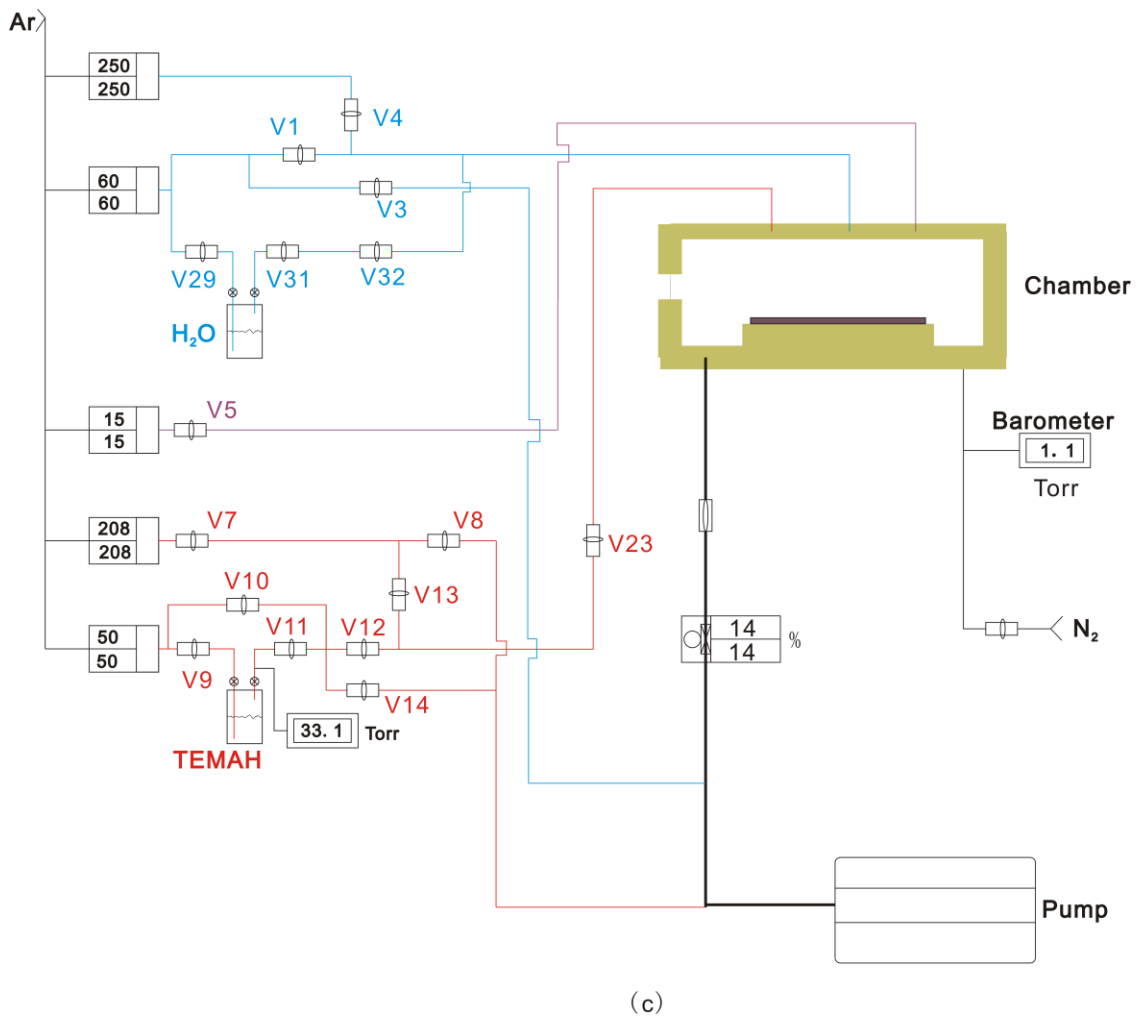
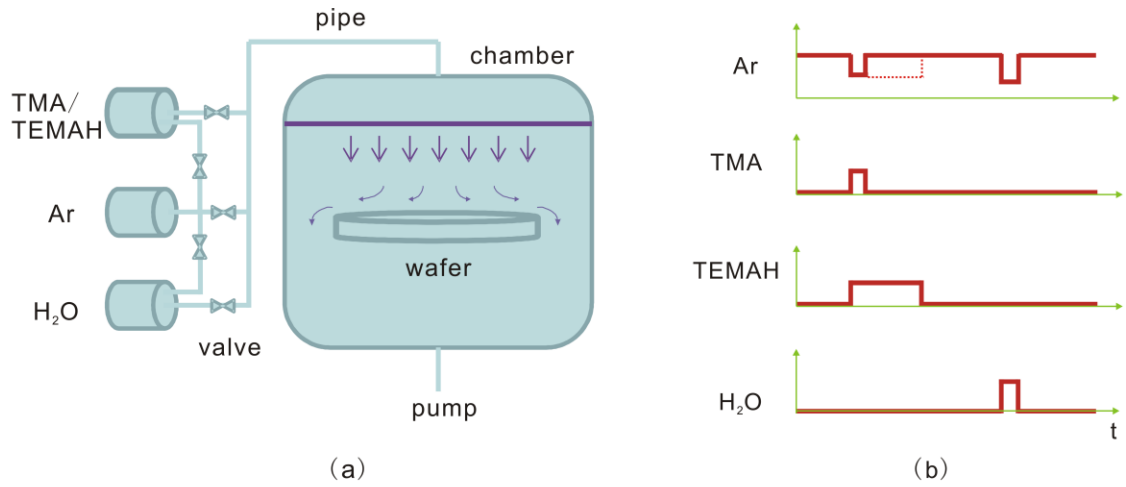


Fig. 3. (a) Schematic of ALD system; (b) Schematic of gas flow during one ALD cycle. The pressure was kept constant in the chamber. (c) Valve systems for H₂O and TEMAH.

3.2 Film characterization

The films were characterized by different methods. The reflectance and transmittance spectra were measured with lambda 1050 UV/Vis Spectrophotometer (PerkinElmer, MA, USA). The measured accuracy of transmittance was about $\pm 0.2\%$. The refractive indices and extinction coefficients of single layers were determined by fitting the indices of refraction and film thickness using the thin film software Spektrum (LZH, Hannover, Germany).

The film thickness was characterized with Ellipsometry (Sentech 800, Berlin, Germany). The error of thickness measurement was ± 0.5 nm, estimated by measuring the same sample several times, as illustrated in Fig. 4.

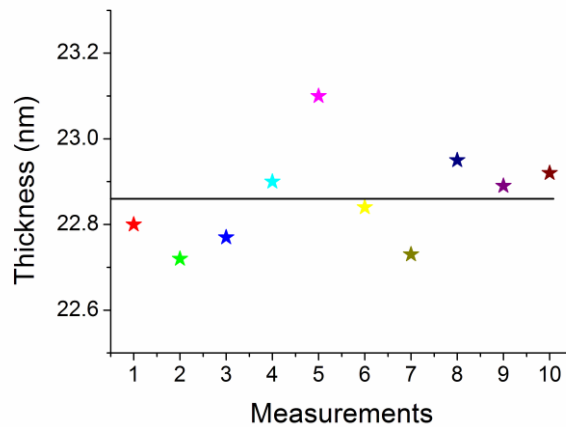


Fig. 4. Measuring the same sample with Ellipsometry.

The elemental composition was assessed by energy-dispersive X-ray Spectroscopy (FEI, OR, USA). H cannot be detected by this method due to the only one electron shell.

The Tauc plot method was used to determine the band gap of the single layer films. By measuring the transmittance and reflectance in the deep UV range, the absorption coefficient α around the absorption edge could be obtained. The Tauc plot shows the quantity $h\nu$ (the energy of photon) on the abscissa and the quantity $(\alpha h\nu)^{1/2}$ on the ordinate [119][120]. The band gap energy of a film was determined by extrapolating the linear region of the Tauc plot to the abscissa.

The profile of fused silica substrate was measured on interferometry (Zygo, Ametek, USA) both before and after coating, and the stress values were calculated following the Stoney's law [121][122].

Weak absorption was characterized using Laser Calorimetry according to ISO 11551 [123][124]. Absorptance below 1 ppm could be discriminated. The error was about 13%, mainly attributed to the uncertainty of the laser power.

S-on-1 LIDT values were measured with a test bench setup according to ISO 21254 [125]. The pulse width was adjusted to 10 ns, the repetition frequency was fixed to 100 Hz, and the beam was focused to an effective diameter of about 300 μm . Overall 154 sites were tested on each sample. Together with each site, the beam energy and detected scattering of each pulse were recorded. Damage was confirmed if the detected scattering exceeded a threshold value and reconfirmed by Nomarski microscope inspection after the test.

The LIDT was determined by extrapolating the fit of damage probability to the abscissa. The absolute error was about 20% and mainly governed by the fluence measurement [125].

Damage morphologies were characterized with either differential interference contrast (DIC) microscopy or confocal laser scanning microscopy (LSM).

4. Deposition of ALD Al_2O_3 and HfO_2

The deposition of ALD Al_2O_3 with TMA/ H_2O has been widely reported as one of the most representative ALD processes. However, the ALD HfO_2 using TEMAH and H_2O in references distinctively differ from each other [126]-[133]. It is necessary to understand the growth kinetics of ALD before the trial experiments.

4.1 Growth kinetics of ALD

The ALD chamber and bubbler are concisely illustrated in Fig. 5. During an exposure step, the precursor molecules are vaporized from the liquid in the bubbler and carried by Ar into the chamber, where adsorption and desorption occur. During a purging step, the molecules in the chamber are being evacuated by the pump.

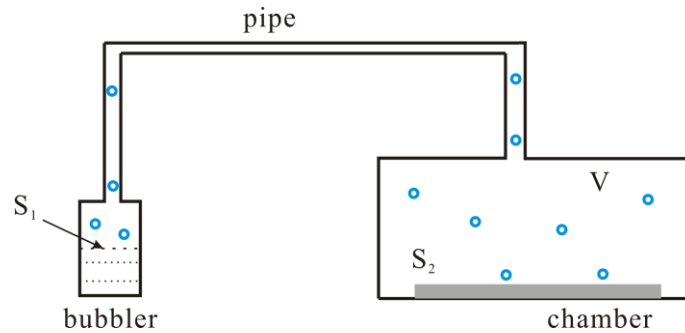


Fig. 5. The trace of precursor molecules.

The amount of precursor molecules N_t in the chamber can be expressed by equation (12). In a unit time, the variation of N_t equals the vaporized molecules from the bubbler (N_{vap}), minus the adsorbed molecules onto the surfaces such as chamber walls and substrates (N_{ads}), plus the desorbed molecules from the surfaces (N_{des}).

$$\frac{dN_t}{dt} = \frac{dN_{vap}}{dt} - \frac{dN_{ads}}{dt} + \frac{dN_{des}}{dt} \quad (12)$$

It is convenient to separately study the two processes: **vaporization, adsorption/desorption.**

The symbols used in this chapter are illustrated as follows:

N_t	The total number of molecules in the chamber
N_{vap}	number of molecules vaporized from the liquid
N_{ads}	number of molecules adsorbed onto the surfaces
N_{des}	number of molecules desorbed from the surfaces
P_v	vapor pressure

P_p	partial pressure in the chamber
S_1	cross section of the precursor bubbler
S_2	the area of substrate surface
V	volume of the chamber
T_1	bubbler temperature
T_2	chamber temperature
k	Boltzmann coefficient, $1.38 \times 10^{-23} \text{ m}^2\text{kg/s}^2\text{K}$
m	molecular mass, molecular number $\times 1.67 \times 10^{-27} \text{ kg}$
Q	surface coverage
ρ	density of adsorbent sites on surface
C_d	desorption rate

The physical properties of the precursors are summarized in Table 5.

Table 5. Physical properties of TMA, TEMAf and H₂O.

	TMA	TEMAf	H ₂ O
molecular number	40	212	18
melting point	15 °C	<20 °C	0 °C
vapor pressure	6.85 Torr	0.56 Torr	12.8 Torr
	@ 15 °C	@ 80 °C	@ 15 °C
boiling point	125 °C	248 °C	100 °C
decomposing point	-	~140 °C	-

4.1.1 Vaporization

The rate of vaporization is described by the Langmuir's evaporation equation (13).

$$\frac{dN_{\text{vap}}}{dt} = \frac{V}{kT} \frac{dP_p}{dt} = \frac{(P_v - P_p) S_1}{\sqrt{2\pi m k T_1}} \quad (13)$$

Solving the above equation, the partial pressure P_p in the chamber is determined by:

$$P_p = P_v \left[1 - \exp \left(-t \frac{S_1}{V} \sqrt{\frac{kT_1}{2\pi m}} \right) \right] \quad (14)$$

The partial pressure increases gradually with time t , approaching the vapor pressure P_v of the precursor. The time for a saturate vaporization is mainly dependent on:

- ♦ S_1 , Cross-section of the bubbler;

- ♦ V , volume of the chamber;
- ♦ T_1 , temperature of the bubbler.

The vaporization might also be influenced by the diffusion rate of molecules into the chamber, therefore affected by the flow of the carrier gas.

For the precursors TMA, TEMAH and H₂O in this experiment, the partial pressure versus time during vaporization is shown in Fig. 6. The saturation of partial pressure occurs after less than 0.06 s.

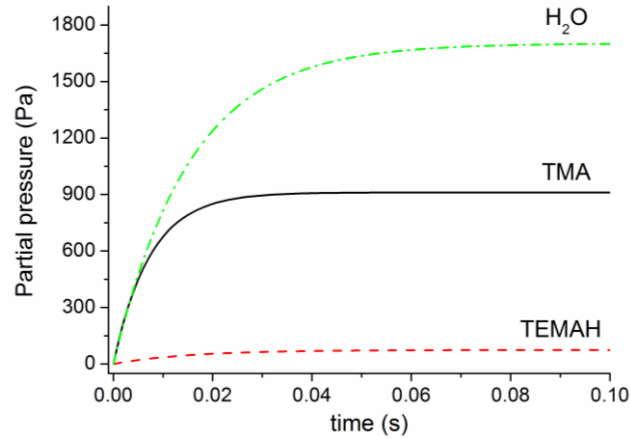


Fig. 6. Partial pressure during vaporization of different precursors.

4.1.2 Adsorption and desorption

The potential well on the substrate surface for an incident precursor molecule is depicted in Fig. 7. The incident molecule is adsorbed to the surface first, then it might be trapped in the potential, or diffused to a deeper potential, or desorbed from the surface. The chemi-sorption has much larger potential energy than physi-sorption. Though chemi-sorption is essential for the growth of ALD film, physi-sorption is a key role in determining the film thickness and uniformity.

Arrhenius equation (15) is often used to calculate the desorption rate, though it is an empirical equation. The desorption rates of typical physi-sorption and chemi-sorption on a 200 °C substrate are calculated, as shown in Table 6.

$$C_d = \exp\left(-\frac{E_{potential}}{kT}\right) \quad (15)$$

Table 6. Desorption rate in case of physi-sorption and chemi-sorption.

		Physi-sorption	Chemi-sorption
<i>potential depth</i>	$E_{potential}$	0.01-0.1 eV	1 eV
<i>desorption rate</i>	C_d	13%-81%	1.37×10^{-9}

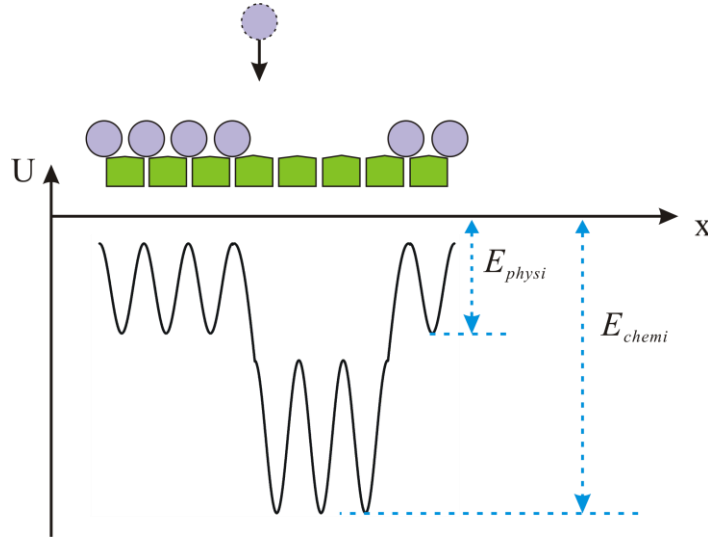


Fig. 7. The potential on the substrate surface.

The following conclusions can be drawn through analysis of Table 6 and the mechanism of adsorption:

- ♦ The adsorbent sites for chemi-sorption are limited, because the reactive adsorbent sites are consumed after the chemi-sorption, and not regenerated until the next cycle of ALD;
- ♦ The adsorbent sites for physi-sorption are limited. The desorption rate of physi-sorption is quite large, overlapped molecules have much smaller survival probabilities.

The coverage of adsorbent sites Q on the surface for each precursor can be expressed as in equation (16). In the exposure step, both adsorption and desorption occur, while in the purging step only desorption exists.

$$\left\{ \begin{array}{l} \rho \frac{dQ}{dt} = \frac{P_p(1-Q)}{\sqrt{2\pi mkT_2}} - \rho QC_d \quad \text{exposure} \\ Q|_{t=0} = 0 \\ \frac{dQ}{dt} = -QC_d \quad \text{purging} \end{array} \right. \quad (16)$$

The solution of equation (16) is:

$$\left\{ \begin{array}{l} Q = \frac{C_0}{C_0 + C_d} \{1 - \exp[-(C_0 + C_d)t]\} \quad \text{exposure} \\ Q = \frac{C_0}{C_0 + C_d} \exp(-C_d t) \quad \text{purging} \end{array} \right. \quad (17)$$

In which, $C_0 = P_p / \rho \sqrt{2\pi mkT_2}$ is applied for clarity.

For physi-sorption, the coverage increases gradually, approaching the saturate value in the exposure step, and returns to zero in the purging. For chemi-sorption, the coverage increases gradually to 100% in the exposure step, and keeps constant in the purging, as illustrated in Fig. 8(a). In an actual ALD half cycle, both physi-sorption and chemi-sorption exist, resulting in the coverage curve in Fig. 8(b).

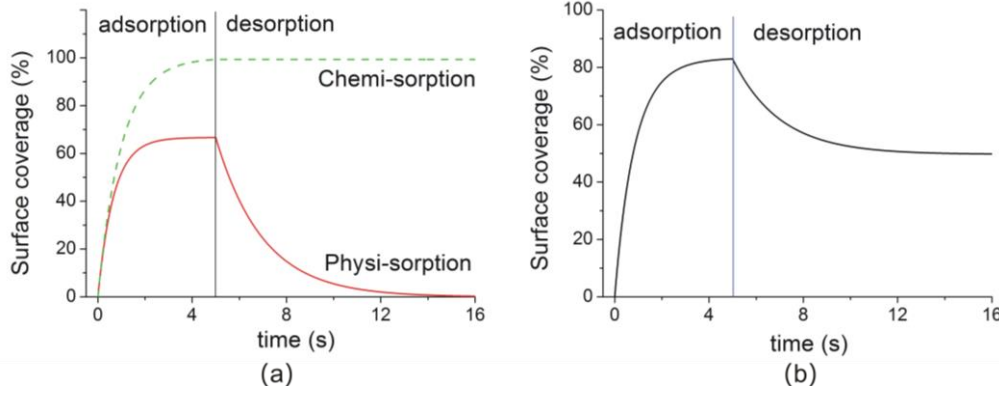


Fig. 8. Schematic of the surface coverage in an ALD exposure step. (a) physi-sorption and chemi-sorption; (b) actual adsorption.

The time for a saturate adsorption or desorption is important for determining the pulse length of the steps in an ALD cycle. The following conclusions can be drawn analyzing equation (17).

- ♦ The saturating time of adsorption is shorter for a larger partial pressure;
- ♦ The saturating time of desorption is determined by the substrate temperature T_2 and adsorptive potential energy E .

The time scale of a saturate adsorption is much longer than that of a saturate vaporization, as illustrated in Fig. 6 and Fig. 8. The partial pressure P_p can therefore be treated as constant during adsorption.

The chemi-sorption is essential for a film growth. As to the chemi-sorption, in which C_d is zero, the relative saturating time for the adsorption of different precursors is:

$$t_{TMA} : t_{TEMAH} : t_{H_2O} = \frac{\sqrt{m}}{P_p} \Big|_{TMA} : \frac{\sqrt{m}}{P_p} \Big|_{TEMAH} : \frac{\sqrt{m}}{P_p} \Big|_{H_2O} = 3:78:1 \quad (18)$$

Equation (18) provides a clue finding the proper exposure time of a new precursor. The deposition of ALD Al_2O_3 could be easily reproduced on a new plant. The exposure time of TEMAH could be estimated according to equation (18).

However, equation (18) is not precise because some other factors impacting the exposure time are not considered, such as flow rate of carrier gas Ar. Therefore,

4.2. Parameters for the growth of ALD Al₂O₃ and HfO₂

certain trial experiments are still in need to determine the final exposure time of each precursor.

4.2 Parameters for the growth of ALD Al₂O₃ and HfO₂

4.2.1 Bubbler temperature

The vapor pressures of TMA, TEMAH and H₂O are plotted in Fig. 9. Compared to TEMAH, TMA and H₂O have much higher vapor pressure at room temperature. The exposure time of TMA and H₂O can be quite short. However, a shorter than 0.2 s duration is difficult to be controlled due to the sensitivity limit of the valves. The temperature of TMA and H₂O bubbler is thus cooled down to 15 °C, in order to decrease the vapor pressure.

TEMAH has about 10 times lower vapor pressure than TMA, and therefore much longer exposure time. Increasing the bubbler temperature could reduce the exposure time. However, TEMAH is found instable at temperatures above 100 °C [134]-[135]. In these experiments, TEMAH was heated up to 80 °C.

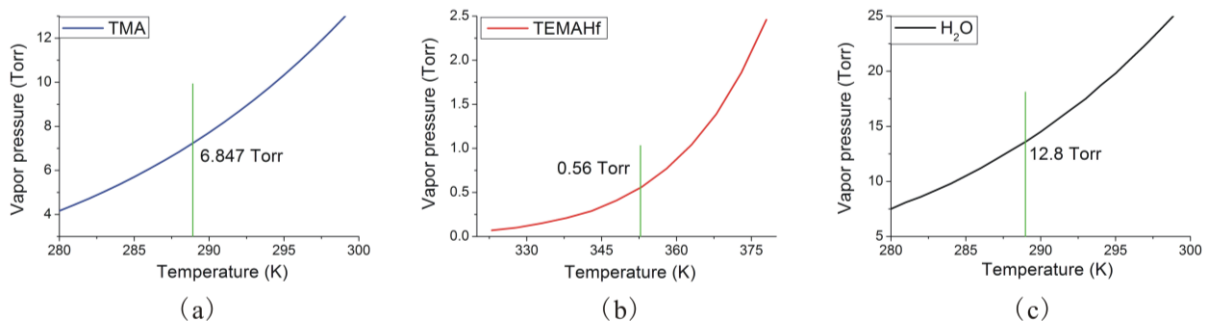


Fig. 9. Vapor pressure of the precursors. (a) TMA; (b) TEMAH; (c) H₂O.

4.2.2 Exposure and purging time

In the first stage, ALD Al₂O₃ was reproduced. The exposure time of TEMAH was then estimated according to equation (18). A number of trial experiments were then carried out to determine the optimum parameters for ALD HfO₂. GPC (growth per cycle) of the film was studied to evaluate the process parameters. It was obtained by dividing the thickness by the cycle number.

4.2. Parameters for the growth of ALD Al_2O_3 and HfO_2

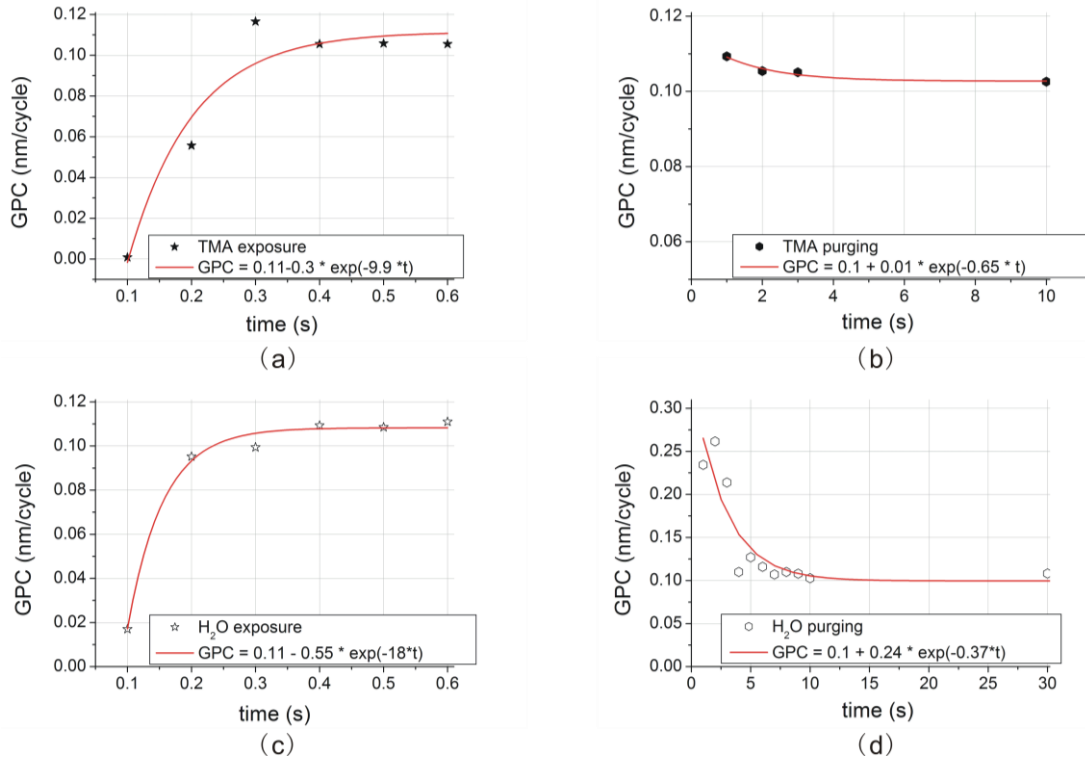


Fig. 10. GPC of an ALD Al_2O_3 cycle plotted versus pulse durations. (a) TMA exposure; (b) TMA purging; (c) H_2O exposure; (d) H_2O purging.

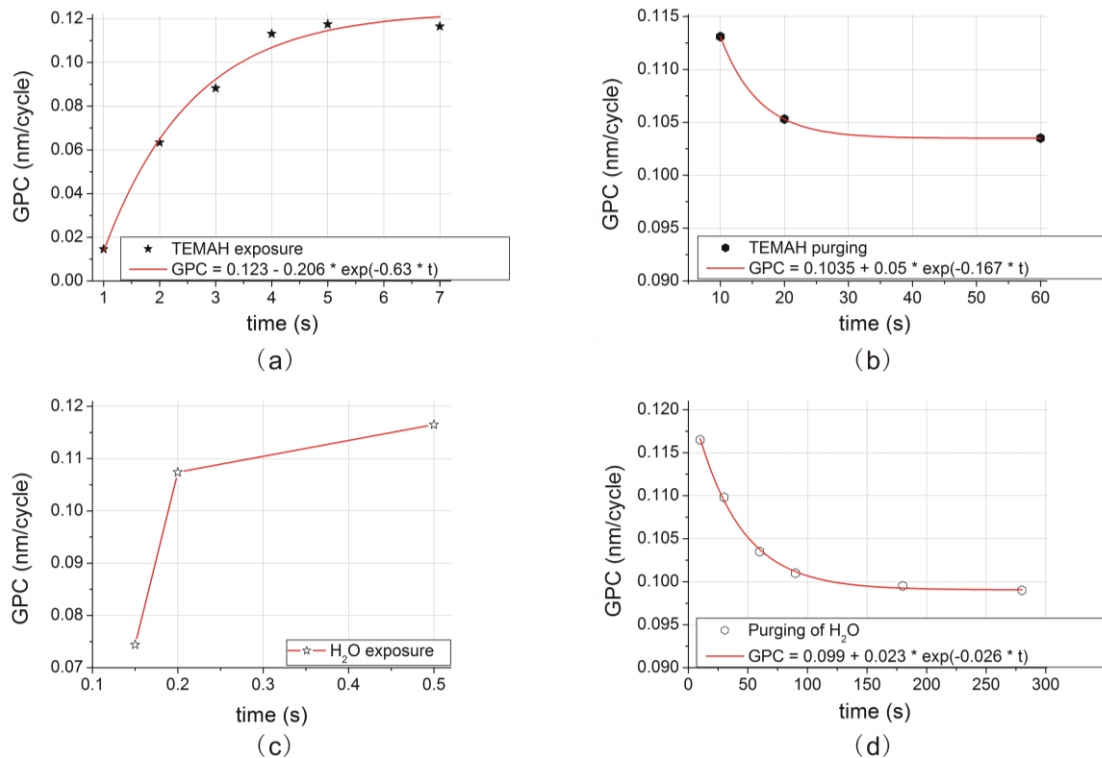


Fig. 11. GPC of an ALD HfO_2 cycle plotted versus pulse durations. (a) TEMAH exposure; (b) TEMAH purging; (c) H_2O exposure; (d) H_2O purging.

4.2. Parameters for the growth of ALD Al₂O₃ and HfO₂

The GPC of ALD Al₂O₃ is plotted versus the pulse durations of TMA/H₂O in Fig. 10. The GPC saturates gradually by nearly 0.11 nm/cycle as the exposure time of TMA or H₂O increases. As the purging time increases, GPC decreases gradually until about 0.1 nm/cycle. The GPC and pulse durations could be approximately fit with equation (17). The same trend of Fig. 10 and Fig. 8(b) verifies the coexistence of physi-sorption and chemi-sorption of the precursors.

The GPC of ALD HfO₂ versus pulse durations of TEMAH/H₂O is plotted in Fig. 11. Similar to that of TMA and H₂O, the GPC and pulse duration of TEMAH could also be fit with equation (17). The exposure time of H₂O is nearly the same for ALD HfO₂ and ALD Al₂O₃, while the purging time of H₂O is distinctively different in the two processes.

A combination of pulse duration should be set for an ALD film deposition, that is, 'precursor exposure / purging / reactant exposure / purging'. The saturation of exposure and purging is necessary in order to control the film thickness by use of the self-terminating feature. The cost of the precursor should also be considered appropriately.

4.2.3 Chamber pressure

The chamber pressure impacts the partial pressure of precursors, therefore affects the exposure time. The necessary exposure time of TEMAH at chamber pressures of 140 Pa and 20 Pa is compared in Fig. 12. The exposure time at low chamber pressure is much longer than that at high chamber pressure. This is consistent with equation (17).

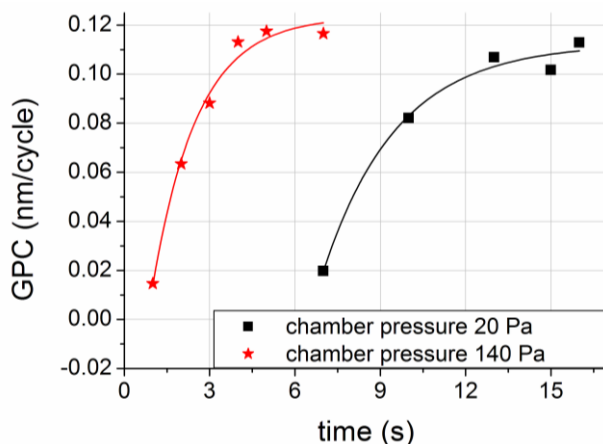


Fig. 12. Exposure time for saturate adsorption of TEMAH at chamber pressure 140 Pa and 20 Pa.

4.2. Parameters for the growth of ALD Al₂O₃ and HfO₂

In this study, the chamber pressure was kept at 140 Pa, with the pumping valve aperture as small as 7%. The pumping valve should not be smaller because a flow of Ar should be guaranteed in the chamber.

4.2.4 Substrate temperature

The substrate temperature affects the ALD process significantly. The desorption rate and surface diffusion rate is low at low temperature, resulting in quite long purging time. On the other hand, the film might be crystallized at high temperature. More importantly, the precursor might be decomposed in the gas pipe and shower head if the substrate temperature is high [135]. According to the reference, the substrate temperature should not exceed 200 °C in order to obtain stable amorphous HfO₂ film [91].

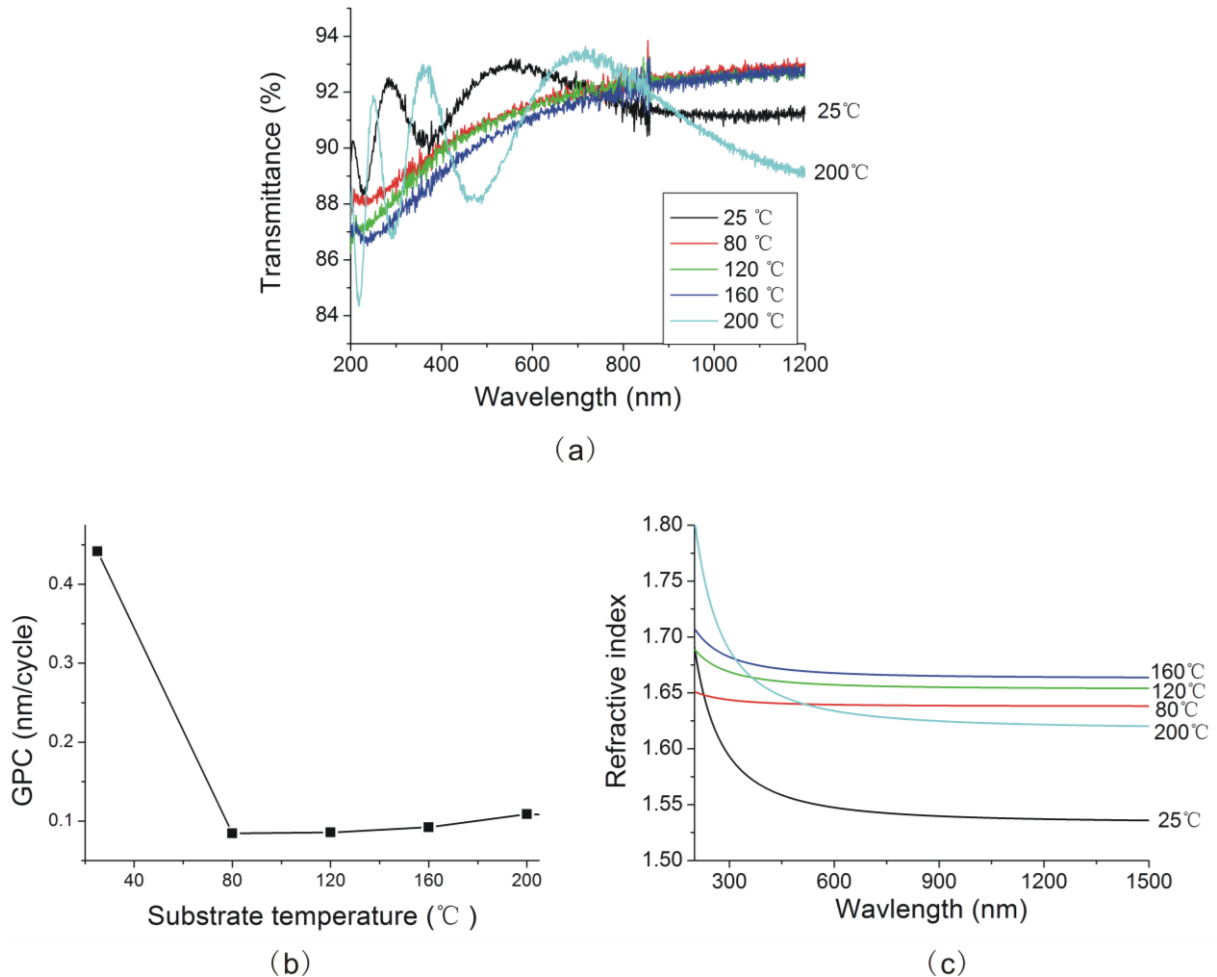


Fig. 13. Impact of substrate temperature on ALD Al₂O₃. 400 cycles were deposited.
(a) Transmittance; (b) GPC; (c) Refractive index.

ALD Al_2O_3 layers were deposited at substrate temperatures varying from 25 to 200 °C. The combination of pulse durations was set to 0.6-2-0.4-8 s, and 400 cycles were deposited on each substrate. The transmittance spectra, growth per cycle (GPC) and refractive indices are shown in Fig. 13.

The 25 °C temperature resulted in GPC as large as 0.5 nm/cycle, however, the refractive index is much lower than a conventional Al_2O_3 film. It is caused by the massive precursor residuals at low temperature. Especially the residual of H_2O decreases the refractive index of the film.

The desorption rate of residual precursors is distinctively larger at substrate temperatures higher than 80 °C. As the substrate temperature increases further, the chemi-sorption reactivity increases gradually, leading to increasing GPC and refractive index in the UV wavelength range simultaneously.

200 °C was selected as the substrate temperature, for the deposition of both Al_2O_3 and HfO_2 .

4.3 Discussion

The desorption rate of the precursors could be evaluated by fitting the GPC plot in Fig. 10 and Fig. 11 with equation (17). The fitting results are listed in Table 7. H_2O has different desorption rate on the surface of Al_2O_3 and HfO_2 , indicating the different physi-sorption energies on different surfaces. The physi-sorption energies are calculated according to the Arrhenius equation (15).

TMA has both low physi-sorption energy and high vapor pressure, making it an excellent precursor for ALD. TEMAH and H_2O have much higher physi-sorption energy, therefore needs longer purging time. TEMAH has also low vapor pressure, needing also a longer exposure time.

Table 7. The inferred physi-sorption energy.

	TMA	H_2O	TEMAH
Desorption rate	65%	2.6-37%	17%
E_{physi} (eV)	0.018	0.041 - 0.149	0.073

The adsorption of precursors could be accelerated by increasing the partial pressure according to equation (17). This could be achieved by heating the precursor, or increasing the flow rate of Ar. However, there is no good way to accelerate the desorption of physi-sorbed precursors. Increasing the substrate temperature might

help, but the crystalline structure induced by high temperature of the substrate is not preferred.

Several options could be considered to obtain a higher ALD growth rate:

1. unsaturate purging.

A shorter purging time could be adopted to reduce the duration of an ALD cycle. In this case, the film thickness is less determined by the self-terminating feature, but more dependent on the valve sensitivity.

2. to change a precursor with lower physi-sorption energy.

O₃ and O₂ plasma have been reported to replace H₂O in some ALD processes, which is a promising trend due to the lower physi-sorption energies [99][100].

4.4 Problems encountered and solved

There were mainly two problems regarding the deposition of HfO₂ in this experiment.

Firstly, TDMAH (Tetrakisdimethylaminohafnium, Hf[N(CH₃)₂]₄, Strem, Massachusetts, USA) was once used as the precursor of HfO₂. However, no film was gained before the precursor was used up, leaving a lot of HfO₂ particles in the pipes and shower head.

Secondly, the shower head was found necessary to be cleaned after each deposition of HfO₂, otherwise, pollution would be introduced in the film in the next deposition. The typical pollution is displayed in Fig. 14, with small particles scattered in area of about 3×4 mm².

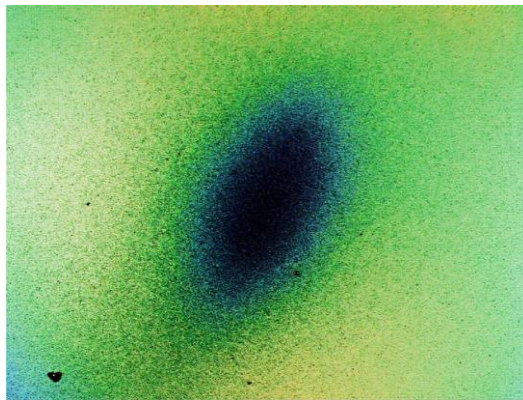


Fig. 14. The typical pollution caused by decomposition of TEMAH. The polluted area is about 3×4 mm².

Both problems were actually caused by the decomposition of precursors. In this system, the shower head was about 20 mm in height above the substrate holder. As the substrate was kept at 200 °C, the shower head should have temperature

between 100 and 200 °C due to heat transfer. TDMAH was decomposed at this temperature in the showerhead. TEMAH had higher decomposing temperature than TDMAH [135], however, certain decomposition might still happen and result in HfO₂ particles in the showerhead [134].

The pollution problem was solved by cleaning the shower head.

To avoid completely the above problems, the substrate and gas pipes should be kept at lower temperature. However, this might result in the residual of H₂O and lead to unpredicted film thickness, therefore was not adopted in this experiment.

4.5 Summary

The molecule kinetics has been studied to instruct the ALD technique. Several key points are summarized from the analysis:

- ♦ The exposure time is determined mainly by the vapor pressure of precursor;
- ♦ The purging time is determined by the physisorption energy and substrate temperature.

An ideal self-terminating process should have both saturate adsorption and desorption. However, the amount of time should also be considered and balanced. The standard parameters for ALD Al₂O₃ and HfO₂ in this dissertation are listed in Table 8.

Table 8. The parameters for this ALD experiment.

	ALD Al ₂ O ₃		ALD HfO ₂	
	TMA	H ₂ O	TEMAH	H ₂ O
bubbler T (°C)	15	15	80	15
exposure time (s)	0.5	0.5	7	0.5
purging time (s)	10	10	60	60
Chamber pressure	140 Pa			
Substrate T (°C)	200 °C			

5. Characterization of ALD Al₂O₃ and HfO₂ single layers

The single layers of ALD Al₂O₃ and HfO₂ were deposited and characterized. As IBS is nowadays one of the most widely used coating techniques, it is desirable to compare the ALD single layers with the IBS layers.

5.1 Comparison of ALD and IBS Al₂O₃ single layers

5.1.1 Stability

ALD Al₂O₃ was deposited in both different modules of the coating system. Different cycles of Al₂O₃ films were deposited in each module. The film thickness was characterized with ellipsometry, as shown in Fig. 15 (a) and (b).

In each of the figures, the thickness could be fitted linearly versus the cycle number, indicating a rather stable self-terminating feature of ALD. No in-situ monitor has been used. The GPC of ALD Al₂O₃ in the 1st module is 0.105 nm ± 4%, while in the 2nd module is 0.110 nm ± 8%. The error of GPC indicates the not strictly saturated precursor adsorption and desorption. The gas pipes, shower head, valves and so on may cause variations of the deposition environment, and induce the error of the film thickness.

The GPC about 0.11 nm is the smallest film thickness resolvable by ALD, and difficult to be achieved by other coating techniques. In application of films thinner than 10 nm, ALD is advantageous in thickness control than other coating techniques. However, for thicker films, a monitor is indispensable.

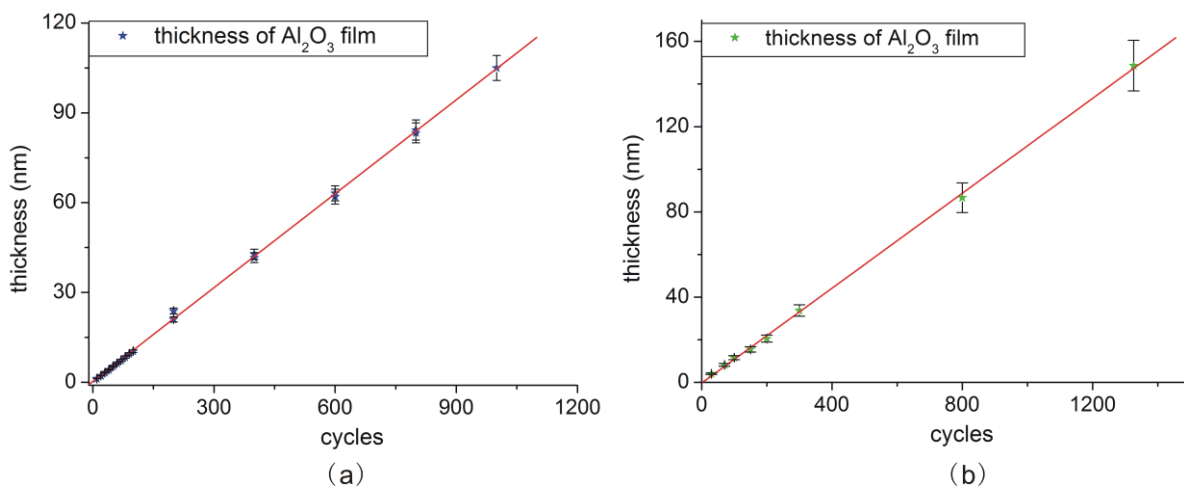


Fig. 15. ALD Al₂O₃ thickness plotted versus cycle number. (a) deposited in 1st module; (b) deposited in 2nd module.

5.1.2 Uniformity

The film thickness at different positions was measured to evaluate the uniformity, as shown in Fig. 16, in which r is the distance to the chamber center. The uniformity of films deposited with different pulse durations and substrate temperatures was compared. 1000 cycles of Al₂O₃ film were deposited on each sample. The exposure time of 0.2 s was insufficient to saturate the adsorption, and purging time 1 s was insufficient for the complete desorption.

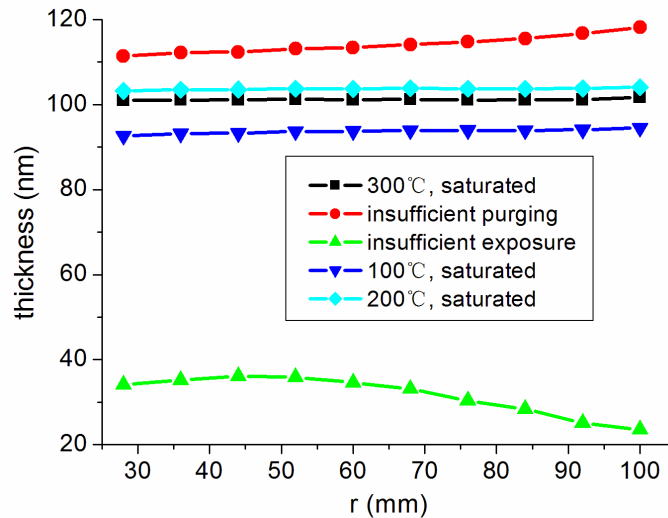


Fig. 16. Uniformity of Al₂O₃ films deposited with different parameters.

The insufficient exposure to precursors leads to poor growth and uniformity. The insufficient purging leads to thicker films while poor uniformity. The films are uniform if both the exposure and purging are saturated. The 100 °C substrate temperature leads to lower reactivity of precursors. In this dissertation the substrate temperature is set to be 200 °C. Further increasing the temperature does not improve the film quality of ALD Al₂O₃.

5.1.3 Elements

The elemental composition of ALD Al₂O₃ was characterized with EDX as shown in Fig. 17. Aside from Al and O, the element C was also detected. As H is not detectable by EDX, C exists probably as –CH₃ ligand from the excessive precursor, and excessive O exists probably as –OH ligand.

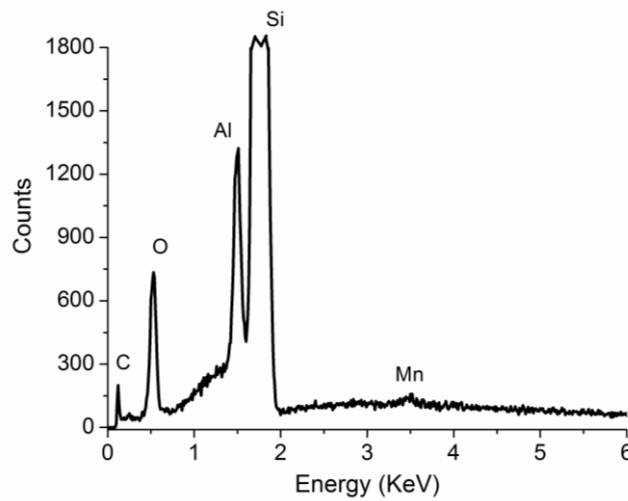


Fig. 17. Elemental composition characterized by EDX.

5.1.4 Dispersion

There is little difference on the film dispersion between system modules. The refractive index and extinction coefficient of the ALD Al₂O₃ film deposited in the 1st module are compared to that of IBS Al₂O₃, as shown in Fig. 18.

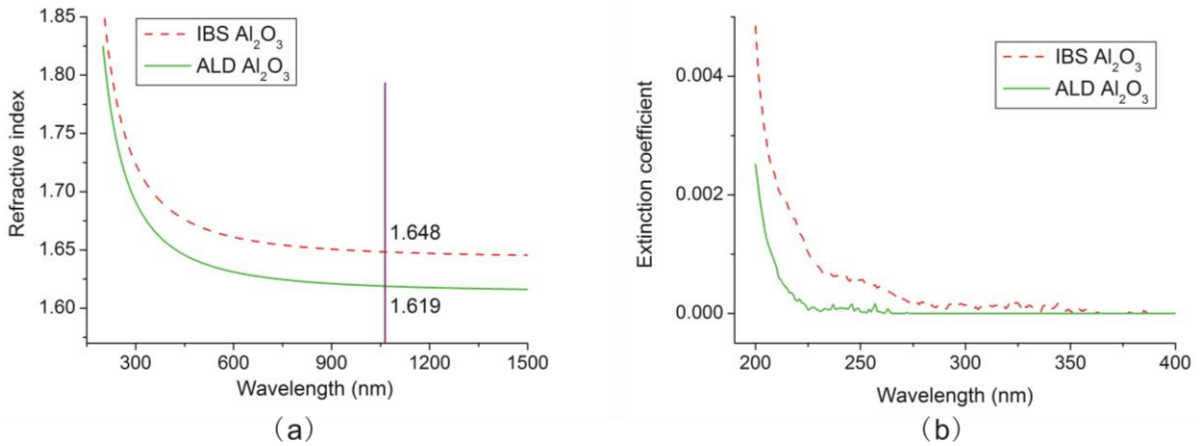


Fig. 18. Dispersion comparison of ALD Al₂O₃ and IBS Al₂O₃ film. (a) Refractive index; (b) Extinction coefficient.

ALD Al₂O₃ has refractive index 1.619 at wavelength 1064 nm, slightly lower than IBS Al₂O₃. It reveals the comparable density of ALD Al₂O₃ with IBS Al₂O₃ film. The extinction coefficient of ALD Al₂O₃ is smaller than IBS Al₂O₃, though both are quite small above wavelength 200 nm.

5.1.5 Band gap energy

The tauc plot of ALD Al₂O₃ film is shown in Fig. 19, in which the band gap energy E_{gap} is found to be 6.5 eV. In comparison, the band gap energy E_{gap} of IBS Al₂O₃ and fused silica substrate are 6.5 eV and 8.3 eV, respectively [136]. ALD Al₂O₃ has the same large band gap energy as IBS Al₂O₃, indicating the potential use for UV and high power lasers.

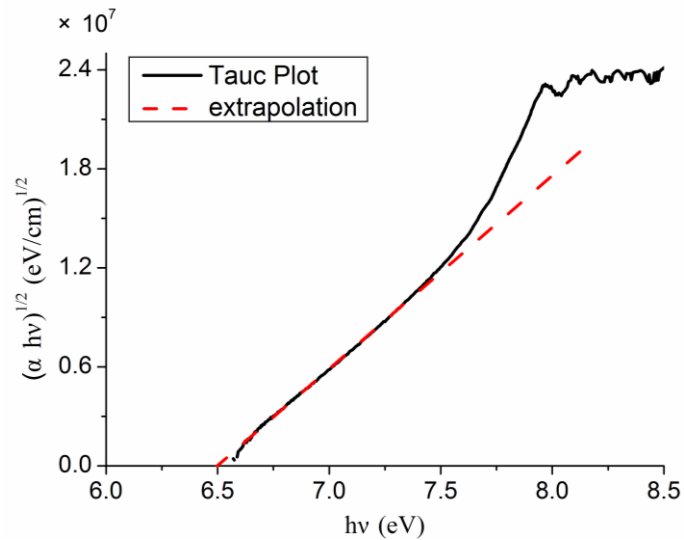


Fig. 19. Tauc plot of ALD Al₂O₃ and extrapolation toward the abscissa.

5.1.6 Stress

The surface profile of ALD Al₂O₃ layer is concave, as shown in Fig. 20(a), corresponding to a tensile stress. Different samples, however, exhibit different stresses, varying from 350-600 MPa. The stress variance is partly caused by the error of measurement, about 10%. Another origin of error is the un-flat substrates, which would be discussed in chapter 9.

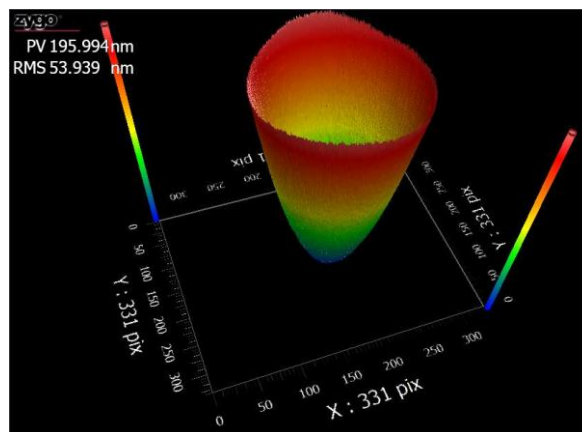


Fig. 20. (a) Surface profile of ALD Al₂O₃ film (104 nm);

5.1. Comparison of ALD and IBS Al₂O₃ single layers

The stress of ALD Al₂O₃ is potentially dangerous for laser components. It would cause cracking or peeling-off when the layer is thick. In comparison, the investigated IBS Al₂O₃ has compressive stress between -300 and -500 MPa [137].

5.1.7 Absorption

The absorptance of ALD Al₂O₃, IBS Al₂O₃ and fused silica substrate are shown in Fig. 21 for comparison. The measurement was carried out with Laser Calorimetry at 1064 nm. The thickness of the substrate was 1mm, and the film thicknesses were about 320 nm. Both ALD Al₂O₃ and IBS Al₂O₃ have absorption as small as 3-4 ppm, indicating their potential for high power laser applications. Basically, the used fused silica substrates contribute 1-2 ppm absorption. Therefore, the film absorption can be estimated to range between 1 and 2 ppm.

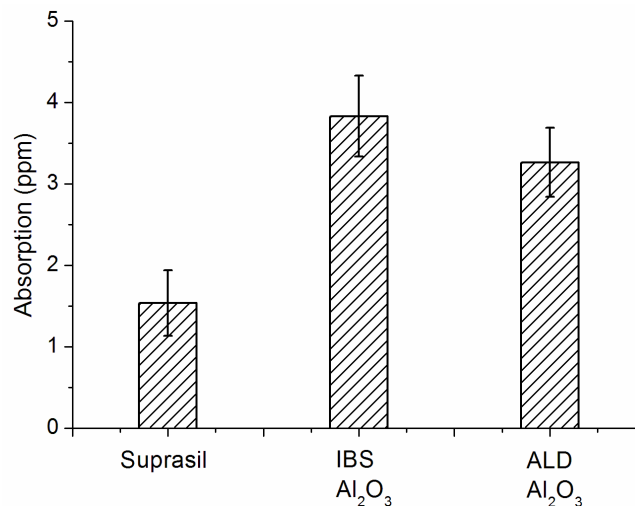


Fig. 21. Absorption comparison of ALD and IBS Al₂O₃.

5.1.8 LIDT and damage morphology

The LIDT of the single layers were tested at 1064 nm. The film thickness of ALD Al₂O₃ was 102 nm, of IBS Al₂O₃ was 320 nm. The total pulse number of 10⁴ was divided into 10 segments to plot the characteristic damage curve. In each segment, the damage threshold was obtained by constructing a plot of damage probability versus energy density. The damage probability plots of ALD Al₂O₃ and IBS Al₂O₃ film irradiated by different numbers of pulses are shown in Fig. 22.

5.1. Comparison of ALD and IBS Al₂O₃ single layers

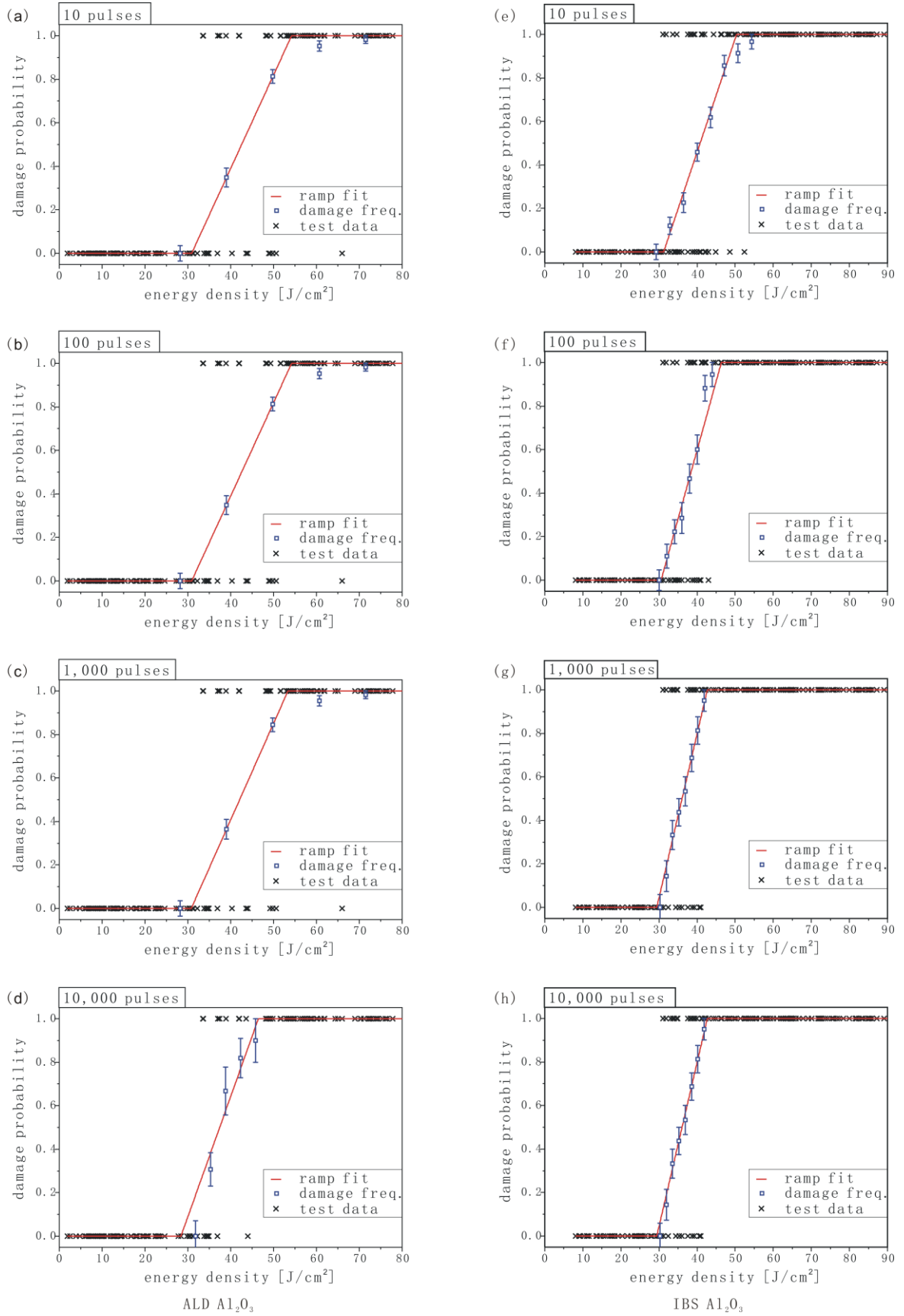


Fig. 22. Damage probability plots. (a)-(d) ALD Al₂O₃; (e)-(h) IBS Al₂O₃.

5.1. Comparison of ALD and IBS Al₂O₃ single layers

For 10 pulses irradiation (Fig. 22a), the first observed damage of ALD Al₂O₃ occurs at 34 J/cm². As the fluence becomes larger, the damage probability grows gradually. The highest fluence that the film could survive is 65 J/cm², which indicates the potential of improving the LIDT if the defects are eliminated.

For 10,000 pulses irradiation (Fig. 22d), the fluence of first observed damage does not change. However, the highest survival fluence is 45 J/cm², smaller than that irradiated by 10 pulses. It indicates a fatigue effect as massive pulses irradiate the same site.

The IBS Al₂O₃ has similar LIDT to ALD Al₂O₃, about 30 J/cm². The highest survival fluence is also close to that of ALD Al₂O₃, about 52 J/cm² for 10 pulses irradiation and 40 J/cm² for 10,000 pulses irradiation, respectively.

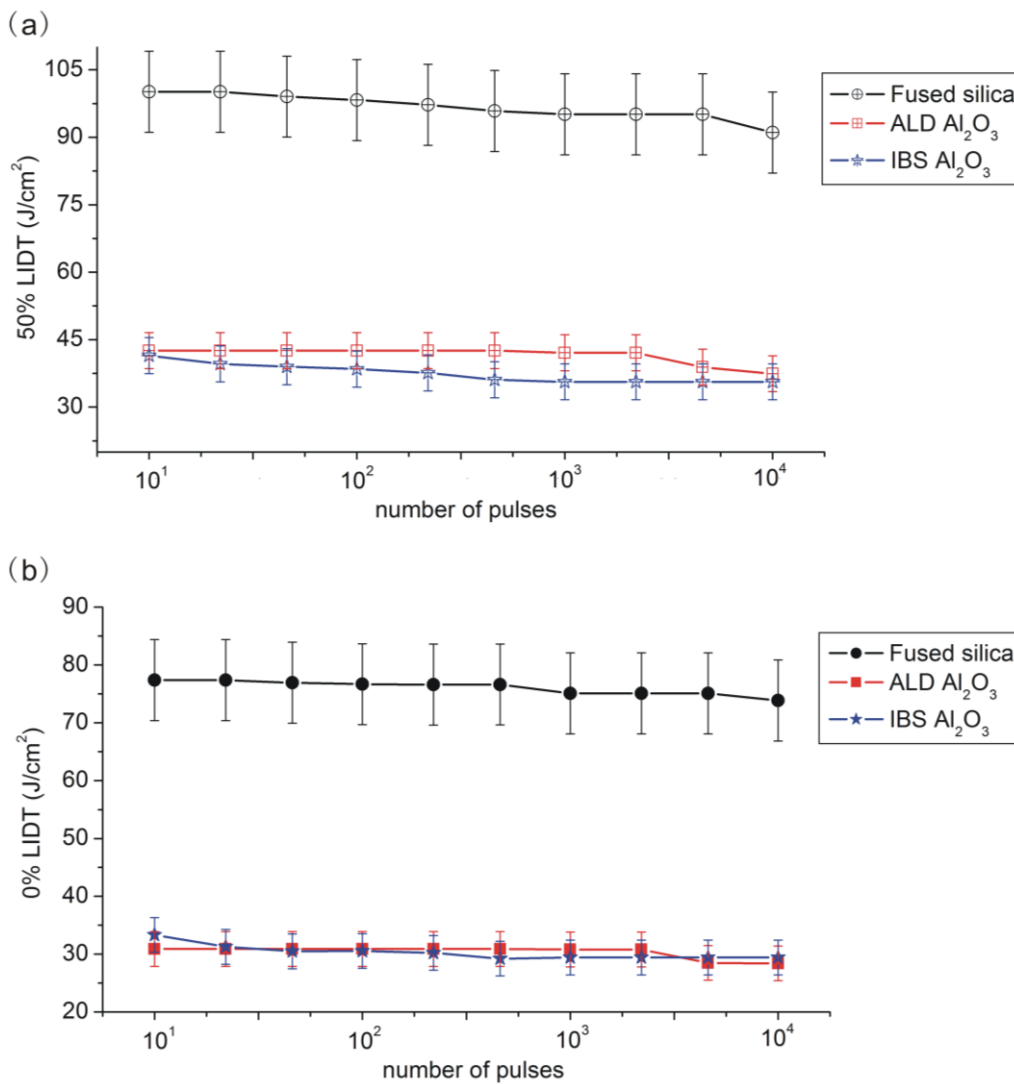


Fig. 23. Characteristic damage curves of fused silica substrate, ALD Al₂O₃ and IBS Al₂O₃. (a) 50% LIDT; (b) 0% LIDT.

5.1. Comparison of ALD and IBS Al₂O₃ single layers

The characteristic damage curves of ALD Al₂O₃ and IBS Al₂O₃ are compared in Fig. 23. The 50% LIDTs are plotted in Fig. 23(a), which means the damage probability equal to 50%. The 0% LIDTs are plotted in Fig. 23 (b), which means 0% damage probabilities. ALD Al₂O₃ has the same 0% LIDT as IBS Al₂O₃, but slightly higher 50% LIDT. However, the LIDT of ALD Al₂O₃ might be overestimated as the defect density might be lower in a thinner film. The characteristic damage curves of the fused silica substrate are listed for comparison, which are much higher than the films.

The typical damage morphologies are displayed in Fig. 24. The stripes on LSM images are not topologies on the sample surface, but interferences from the substrate rear surface.

The morphologies in the 1st row are defect-induced pits caused by relatively low fluence pulses. These defects originate either from the coating process or from the substrate-film interface.

Scalds become typical morphologies as the laser fluence grows higher. The scalds have irregular shape in spite of the Gaussian laser spot, indicating the influence of defects.

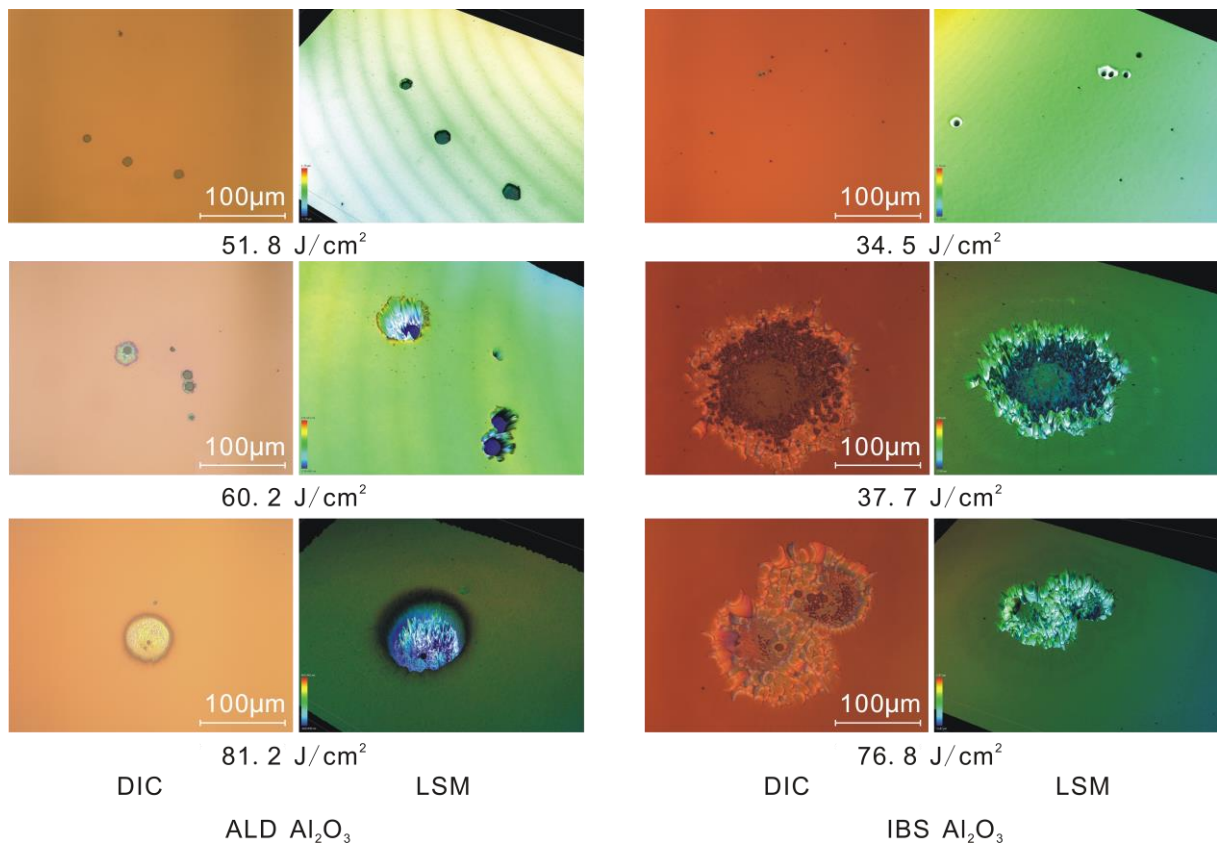


Fig. 24. Damage morphologies of ALD and IBS Al₂O₃ film layer.

5.2 Comparison of ALD and IBS HfO₂ single layers

5.2.1 Stability

As discussed in chapter 4, the pulse durations of ALD HfO₂ for both saturated adsorption and desorption should be 7/60/0.5/60 s. However, it costs too long time to deposit a film layer for optical application. It is reasonable to sacrifice the thickness precision to some extent to save the time cost. The shorter pulse durations 5/5/0.2/30 s was eventually selected for the following study. The film thicknesses of both pulse durations are studied, as shown in Fig. 25.

For both pulse durations, the film thickness could be fitted linearly versus the cycle number, indicating a rather stable self-terminating feature. The average GPC of the films prepared by shorter pulse durations is 0.106 nm ± 7%, while of the films prepared by longer pulse durations is 0.107 nm ± 3%. The fitting of the shorter pulse durations has standard error 1.04, also larger than the 0.16 of the longer durations. It indicates the not strictly saturated precursor adsorption and desorption. The pulse duration and the instable depositing environment (gas pipe, shower head, etc) contribute mainly to the error of the film thickness.

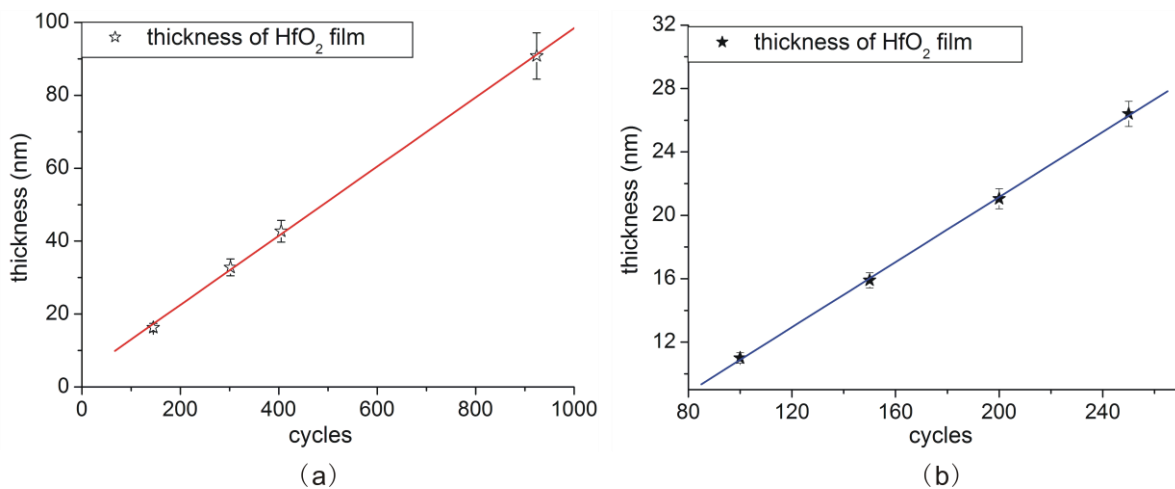


Fig. 25. Thickness of different cycles of ALD HfO₂ layers. (a) pulse durations 5/5/0.2/30 s; (b) pulse durations 7/60/0.5/60 s.

5.2.2 Uniformity

1248 cycles of ALD HfO₂ were deposited on a Si substrate, and the film thickness at different positions was measured. As shown in Fig. 26. The uniformity is above 99% over a range of 120 mm.

5.2. Comparison of ALD and IBS HfO₂ single layers

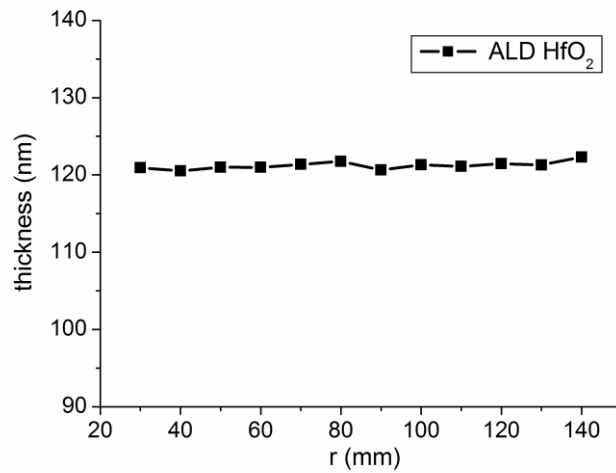


Fig. 26. Uniformity of ALD HfO₂ film.

5.2.3 Elements

The elemental composition of ALD HfO₂ was characterized by EDX, as shown in Fig. 27. Aside from Hf and O, the element C is detected. The same as that of ALD Al₂O₃, C exists probably as precursor residuals –NCH₃CH₂CH₃, and excessive O is in form of -OH. N is undetected because of the little amount.

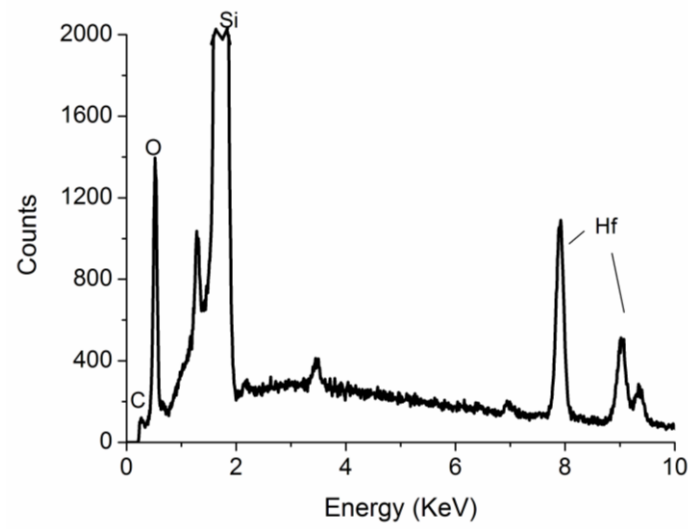


Fig. 27. Elemental composition of ALD HfO₂ characterized by EDX.

5.2.4 Dispersion

The refractive index and extinction coefficient of ALD and IBS HfO₂ films are compared in Fig. 28. The refractive indices of ALD and IBS HfO₂ films are quite close

5.2. Comparison of ALD and IBS HfO₂ single layers

to each other, 1.991 and 1.995 respectively at wavelength 1064 nm. It indicates the similar high density of the films.

The extinction coefficients of both films, however, are quite high in the UV range compared to ALD Al₂O₃. ALD HfO₂ exhibits smaller extinction coefficients than IBS HfO₂.

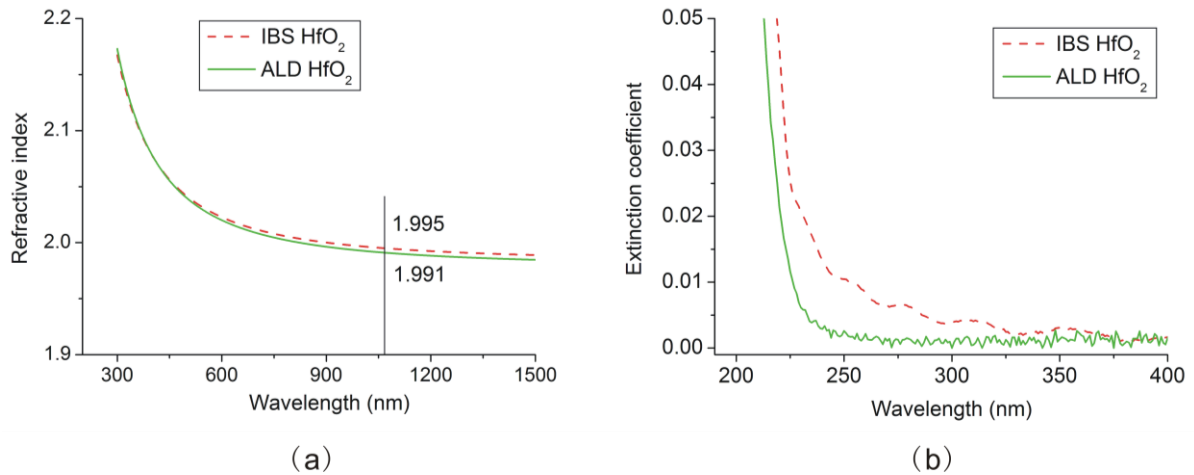


Fig. 28. Dispersion comparison of ALD HfO₂ and IBS HfO₂ film. (a) Refractive index; (b) Extinction coefficient.

5.2.5 Band gap energy

The tauc plot of ALD HfO₂ film is shown in Fig. 29. The band gap energy E_{gap} is found to be 5.5 eV, higher than the 5.1 eV of IBS HfO₂ [136].

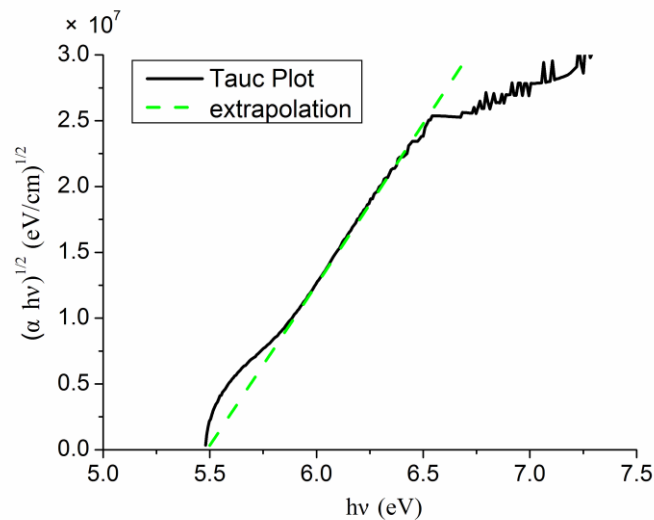


Fig. 29. Tauc plot of ALD HfO₂ and extrapolation toward the abscissa.

5.2.6 Stress

The surface profile of ALD HfO₂ film is concave, as shown in Fig. 30 (a), in contrast to the convex profile of IBS HfO₂ film in Fig. 30 (b). The stress of ALD HfO₂ is tensile, about 800-1000 MPa, while of IBS HfO₂ is compressive, about (-)300-(-)600 MPa.

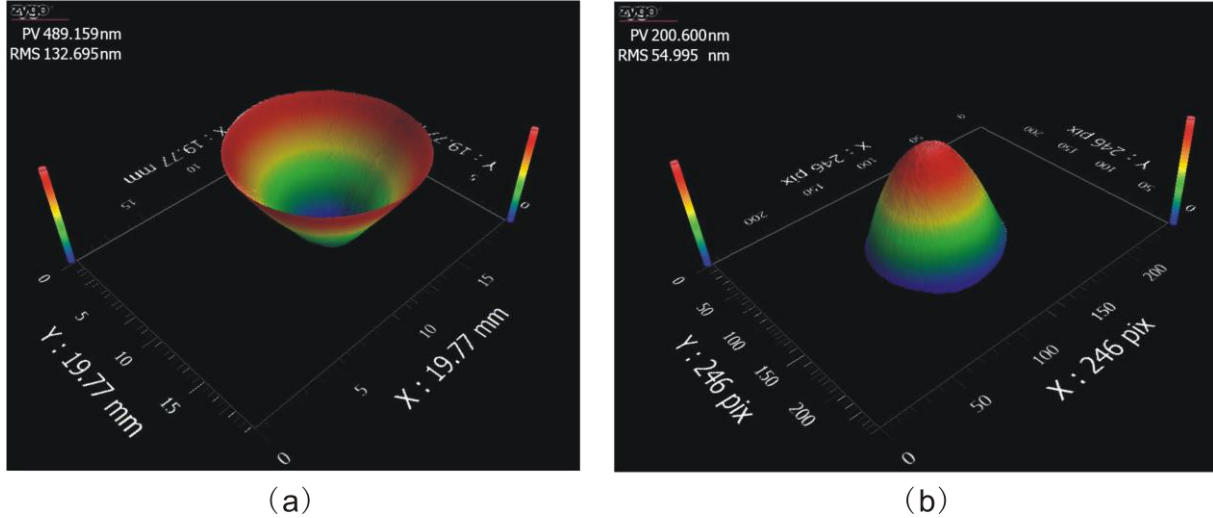


Fig. 30. Surface profiles. (a) ALD HfO₂ film (125nm); (b) IBS HfO₂ film (133 nm).

5.2.7 LIDT and damage morphology

The LIDT of the films were tested at 1064 nm. The damage probabilities of ALD and IBS HfO₂ films irradiated by different number of pulses are shown in Fig. 31.

The first observed damage of ALD HfO₂ occurs at 14.5 J/cm² for the 10 pulse irradiation, and at 14.1 J/cm² for 10,000 pulses irradiation. As the fluence increases, the damage probability grows gradually. However, the growth cannot be fitted linearly. The first few damage probability data are used to determine the LIDT. The highest survival fluence of the film is 37.5 J/cm², which can be viewed as the potential improvement of the LIDT if the defects are eliminated.

The IBS HfO₂ has almost the same LIDT with ALD HfO₂, 12.9 J/cm² for 10 pulses irradiation and 10.7 J/cm² for 10,000 pulses irradiation, respectively. The highest survival fluence is the same of that of ALD HfO₂, 37.5 J/cm².

5.2. Comparison of ALD and IBS HfO₂ single layers

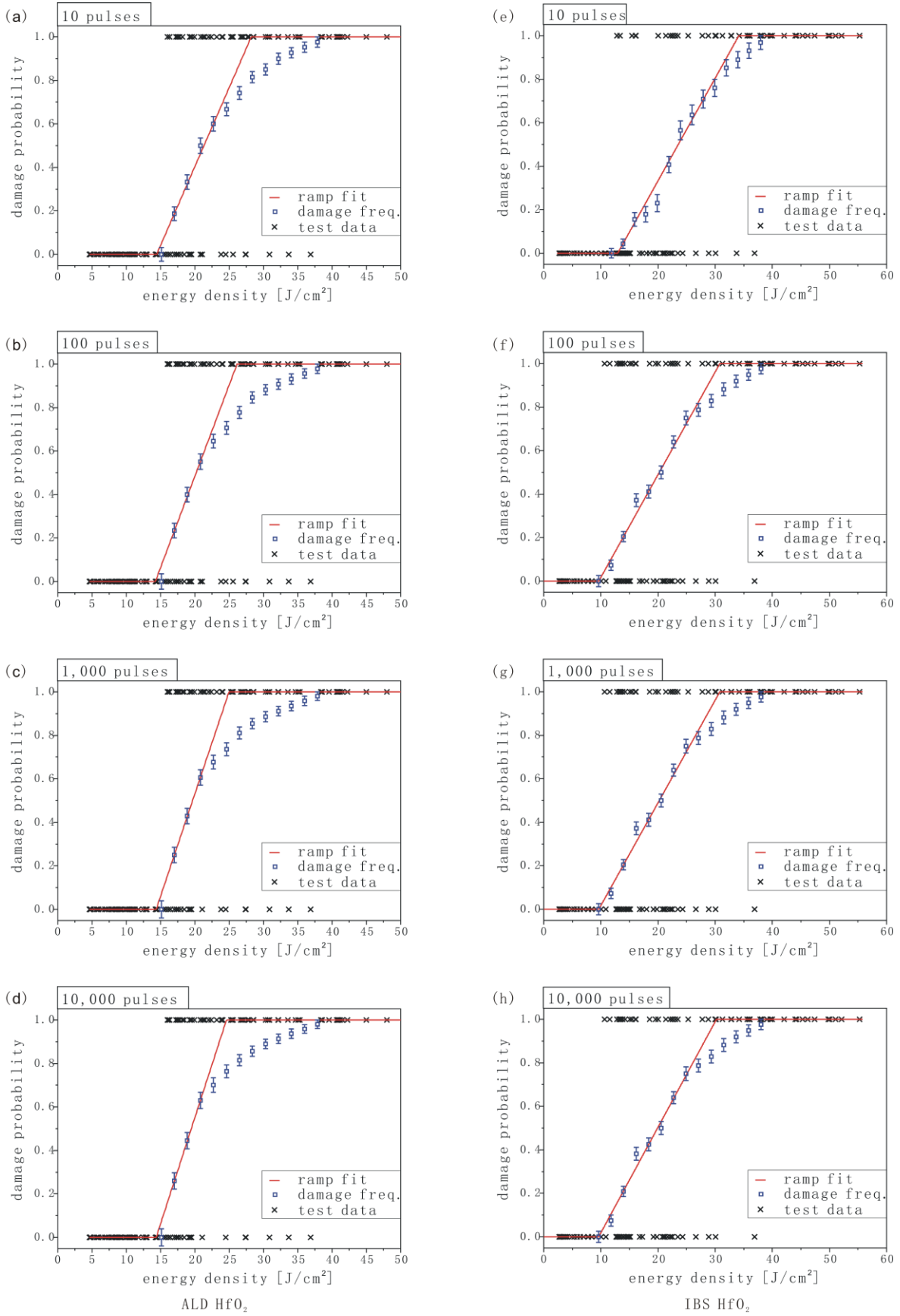


Fig. 31. Damage probability plots. (a)-(d) ALD HfO₂; (e)-(h) IBS HfO₂.

5.2. Comparison of ALD and IBS HfO₂ single layers

The characteristic damage curves of ALD and IBS HfO₂ are compared in Fig. 32. ALD HfO₂ has higher LIDT than IBS HfO₂, especially when irradiated with more pulses. The LIDT decreases to lower fluences due to the fatigue effect.

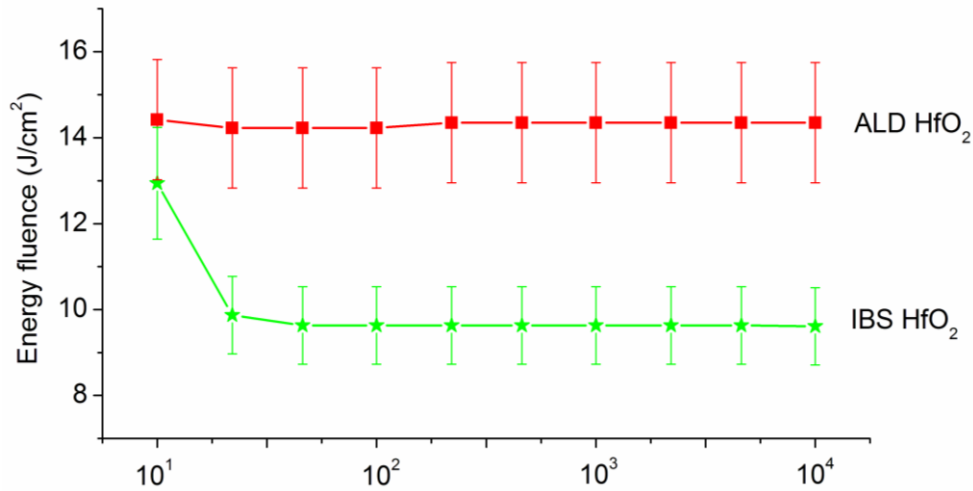


Fig. 32. Characteristic curves of ALD HfO₂ and IBS HfO₂.

The typical damage morphologies are listed in Fig. 33. The depicted damages are caused by fluence near the damage threshold.

ALD HfO₂ exhibit pits when damaged by single pulse, and scalds when damaged by multiple pulses. IBS HfO₂ reveals morphologies connected by pits. The damage of both ALD HfO₂ and IBS HfO₂ are initiated by defects.

5.3. Annealed ALD Al₂O₃ and HfO₂ single layers

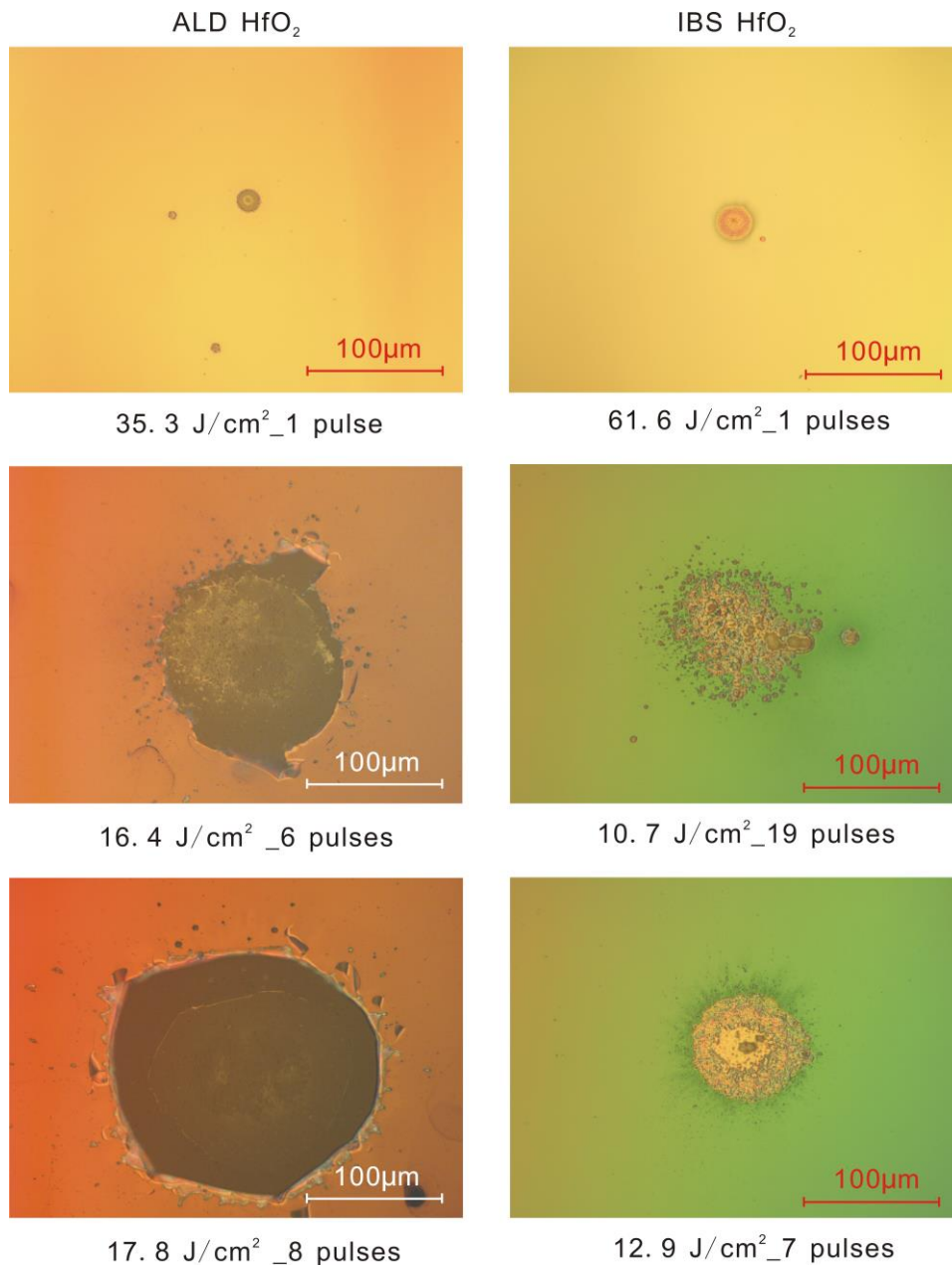


Fig. 33. Damage morphologies of ALD and IBS HfO₂ film layer.

5.3 Annealed ALD Al₂O₃ and HfO₂ single layers

ALD Al₂O₃ and HfO₂ single layer films were annealed at 300 °C, 400 °C and 500 °C, respectively for further studies. The films annealed at 300 °C were studied in comparison with the unannealed films.

5.3.1 Dispersion

As shown in Fig. 34, the refractive index of ALD Al₂O₃ increases no more than 0.01 after annealing at wavelength 1064 nm. The extinction coefficient of Al₂O₃ film

5.3. Annealed ALD Al₂O₃ and HfO₂ single layers

remains a low value. As for ALD HfO₂, the refractive index increases by 0.03 at 1064 nm after annealing. The extinction coefficient increases tremendously after the 500 °C annealing, due to probably crystallization.

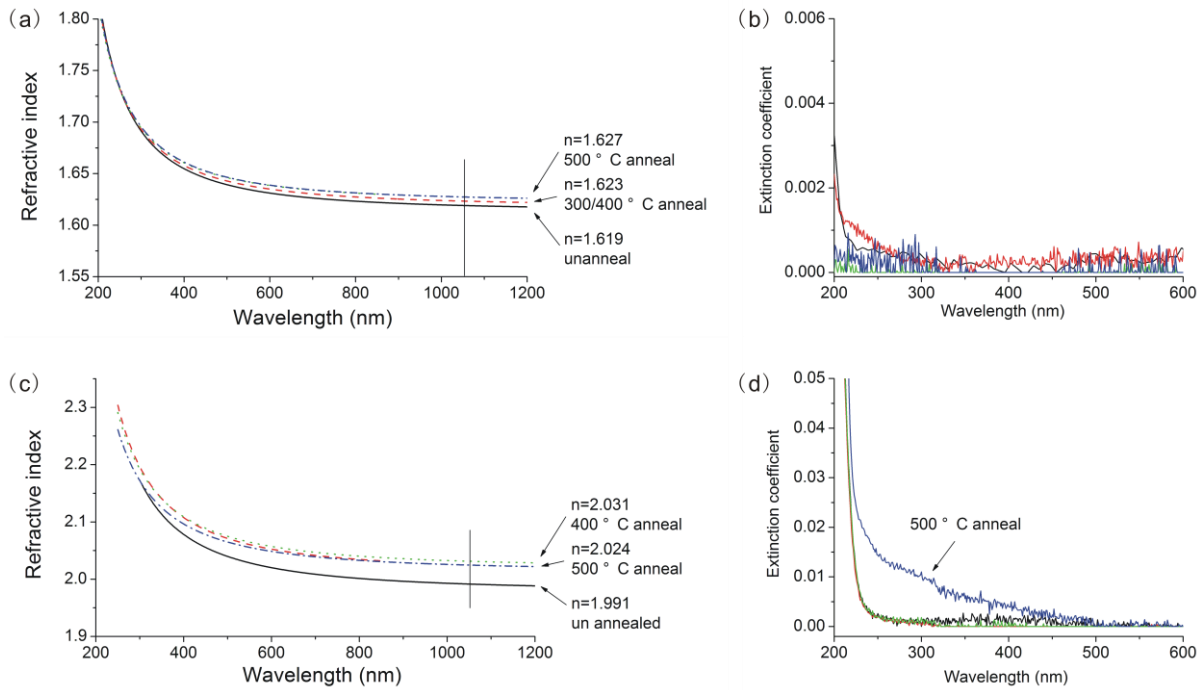


Fig. 34. Dispersion of the annealed ALD films. (a) Refractive indices of annealed ALD Al₂O₃; (b) Extinction coefficients of annealed ALD Al₂O₃; (c) Refractive indices of annealed ALD HfO₂; (d) Extinction coefficients of annealed ALD HfO₂.

5.3.2 Stress

After annealing at 300 °C, the stresses of both ALD Al₂O₃ and HfO₂ films remain tensile, but increase about 7-8%, as shown in Fig. 35.

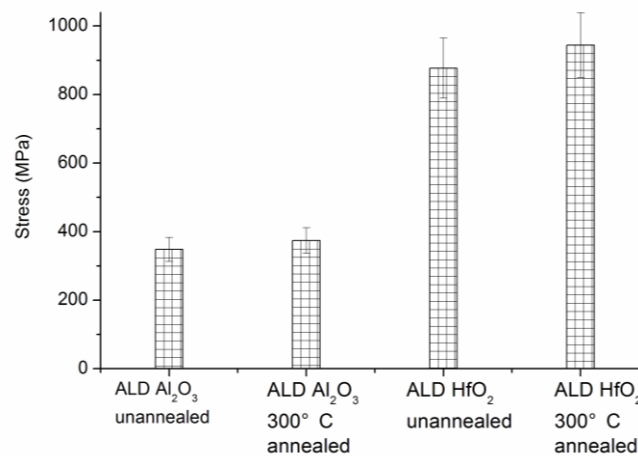


Fig. 35. Stress of the annealed ALD films.

5.3.3 Band gap energy

The band gap energy of ALD Al₂O₃ does not change after 300 °C annealing, while that of ALD HfO₂ increases from 5.5 to 5.6 eV after 300 °C annealing.

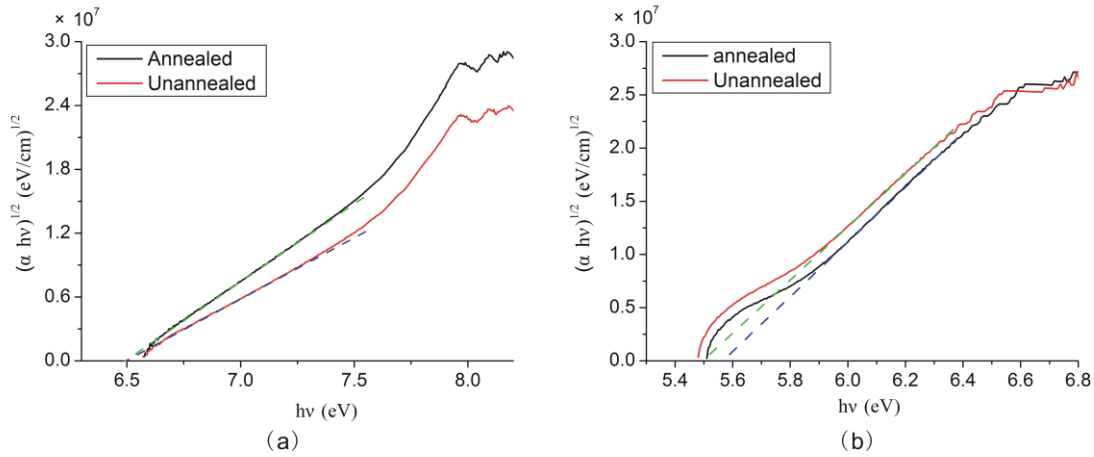


Fig. 36. Tauc plots of the 300 °C annealed films. (a) ALD Al₂O₃; (b) ALD HfO₂.

5.3.4 Absorption

The absorption was measured with Laser Calorimetry at 532 nm. As illustrated in Table 9, the absorption of both films do not change distinctively after 400 °C annealing, but increase tremendously after 500 °C annealing.

Table 9. Absorption of ALD Al₂O₃ and HfO₂ after annealing.

	not annealed	400 °C	500 °C
ALD Al ₂ O ₃ (ppm)	3.5	5.4	871.2
ALD HfO ₂ (ppm)	13.2	19.1	1800

5.3.5 LIDT

The damage probabilities of the ALD Al₂O₃ single layer films annealed at different temperatures are displayed in Fig. 37. The film thicknesses are between 100 and 200 nm.

The LIDT of ALD Al₂O₃ is increased by 30% after 300 °C and 400 °C annealing, however, decreased tremendously after 500 °C annealing. This is consistent with the absorption characterization, which is probably induced by the crystallization at high temperature.

5.3. Annealed ALD Al₂O₃ and HfO₂ single layers

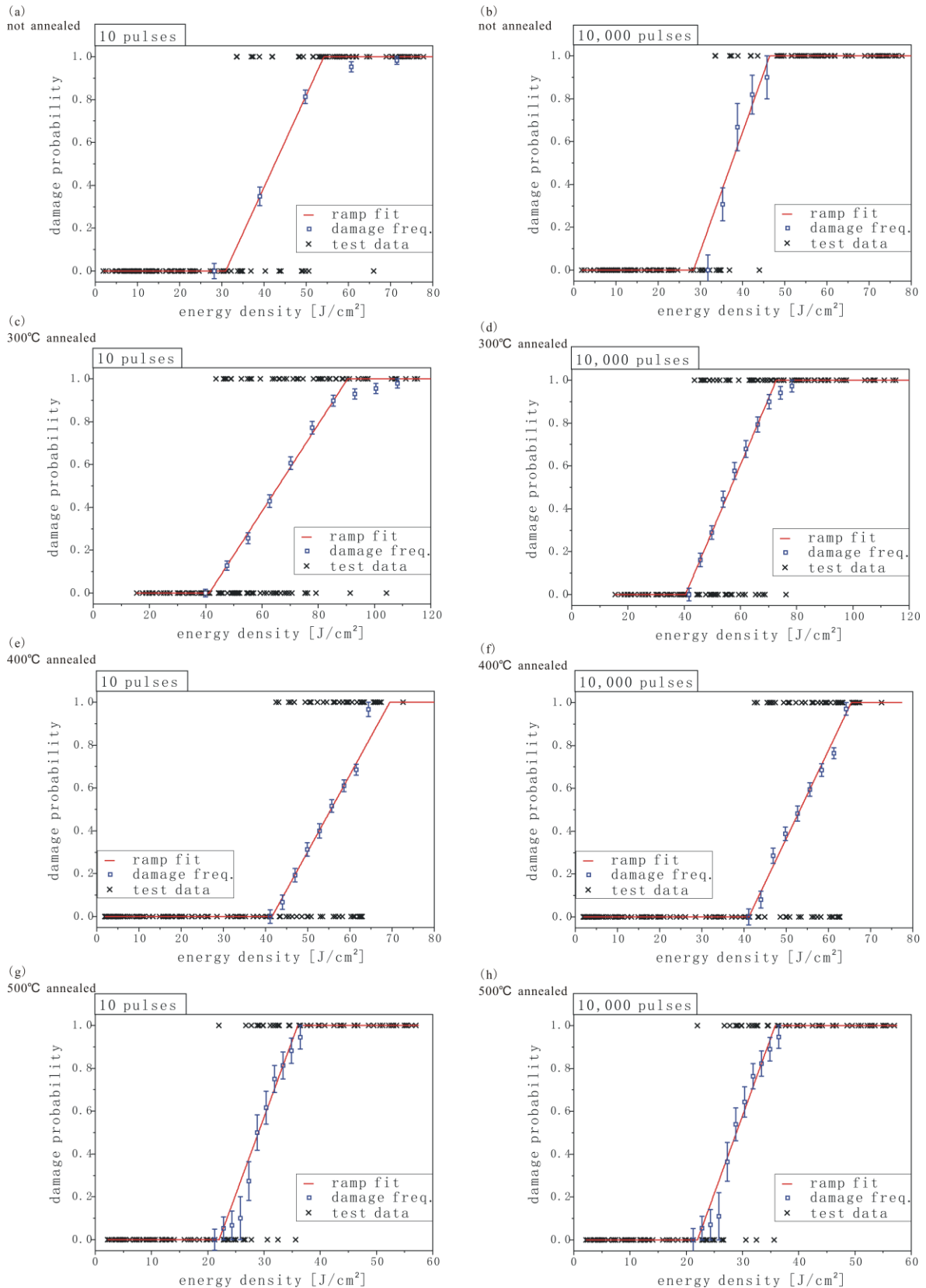


Fig. 37. Damage probabilities of ALD Al₂O₃ annealed at different temperature. (a)-(b): not annealed; (c)-(d): 300 °C annealed; (e)-(f): 400 °C annealed; (g)-(h): 500 °C annealed.

5.3. Annealed ALD Al₂O₃ and HfO₂ single layers

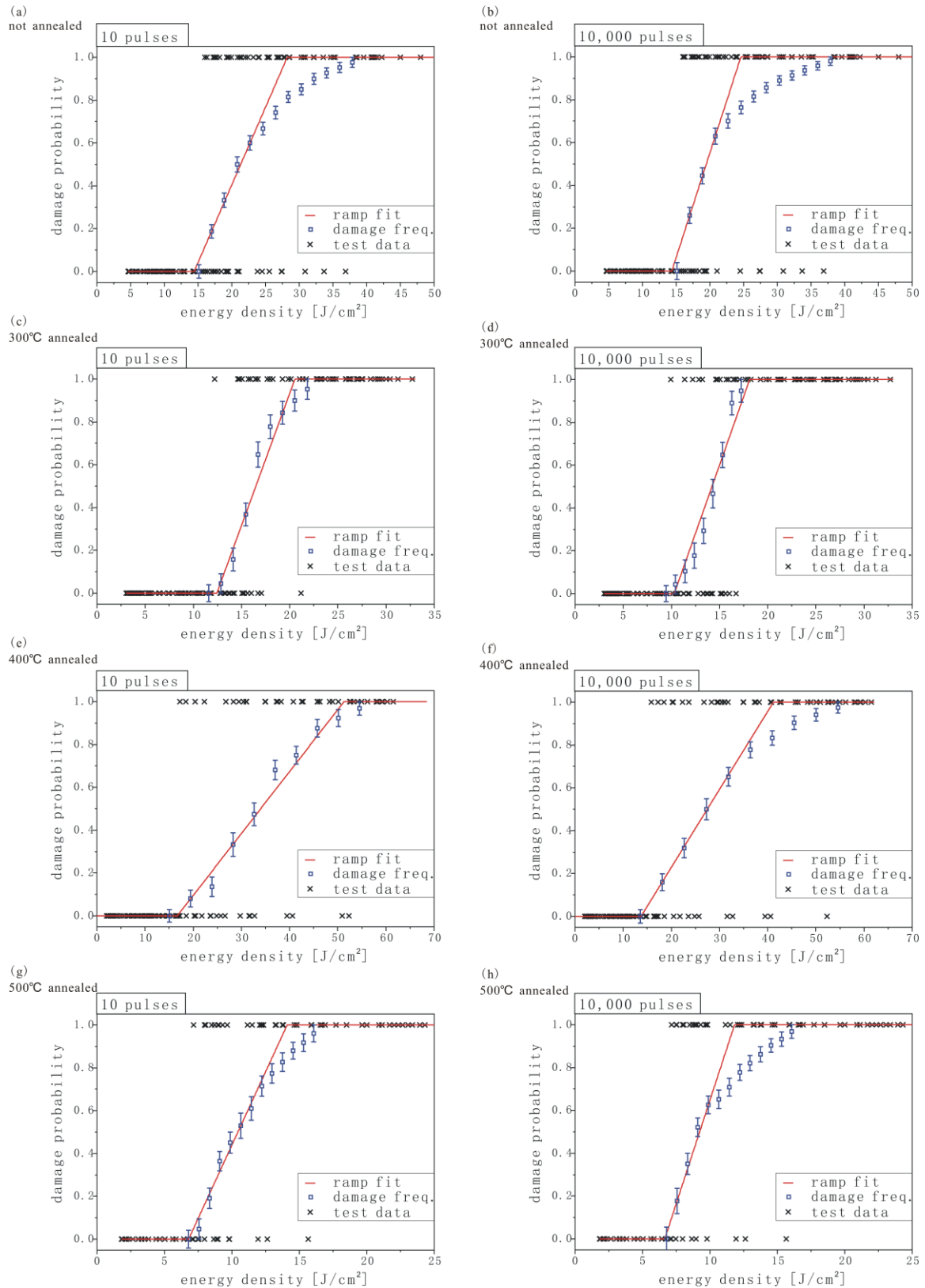


Fig. 38. Damage probabilities of ALD HfO₂ annealed at different temperatures. (a)-(b): not annealed; (c)-(d): 300 °C annealed; (e)-(f): 400 °C annealed; (g)-(h): 500 °C annealed.

5.4. Comparison of ALD Al₂O₃ and HfO₂ with commonly used films

The damage probabilities of the ALD HfO₂ single layers after annealing are displayed in Fig. 38. The film thicknesses are about 100 nm.

The LIDT of ALD HfO₂ is not increased by annealing. Moreover, the highest survival fluence decreases distinctively after 300 °C annealing. The LIDT decreases tremendously after 500 °C annealing, is consistent with the absorption characterization.

The characteristic damage curves of the annealed films are shown in Fig. 39. Annealing at 300 °C /400 °C would lead to the LIDT promotion of ALD Al₂O₃ by 30%, while it does not benefit the LIDT of ALD HfO₂. Annealing at 500 °C is detrimental to the LIDT of both films.

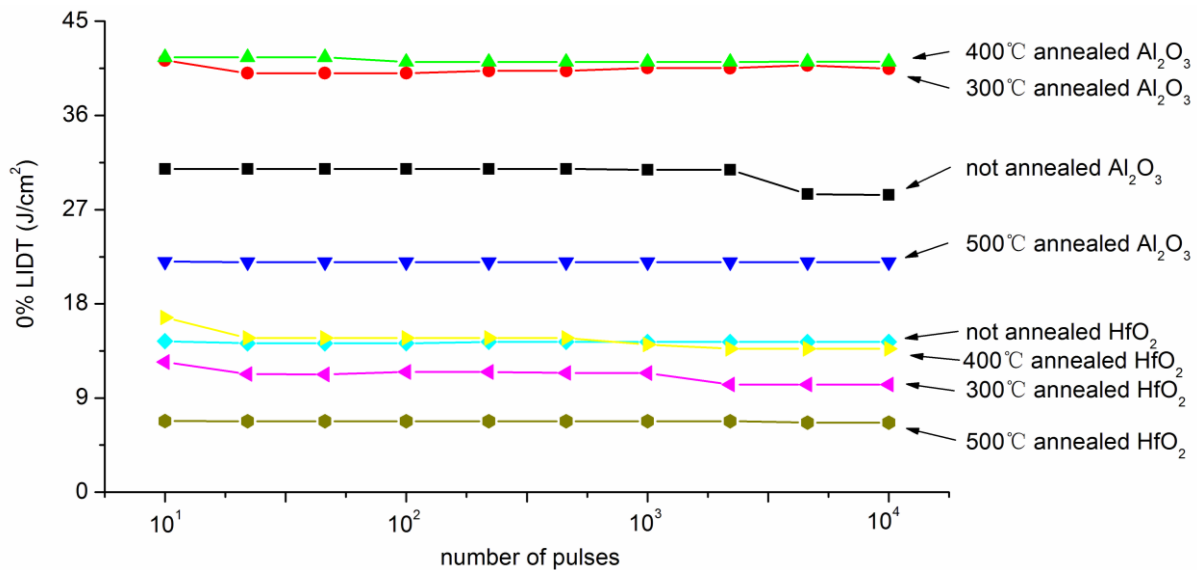


Fig. 39. Characteristic damage curves of ALD single layer films annealed at different temperature.

5.4 Comparison of ALD Al₂O₃ and HfO₂ with commonly used films

For an overview of the ALD film properties, it is necessary to compare the most commonly used optical films in laser applications, such as Ta₂O₅, SiO₂, HfO₂ and Al₂O₃. Ta₂O₅ and SiO₂ were prepared by IBS.

The dispersion curves of the films are displayed in Fig. 40. In optical coating usage, ALD Al₂O₃ could be used as either high refractive index material in combination with SiO₂, or as low refractive index material in combination with HfO₂ and Ta₂O₅. ALD HfO₂ can be used as high refractive index material in the coating design.

5.4. Comparison of ALD Al₂O₃ and HfO₂ with commonly used films

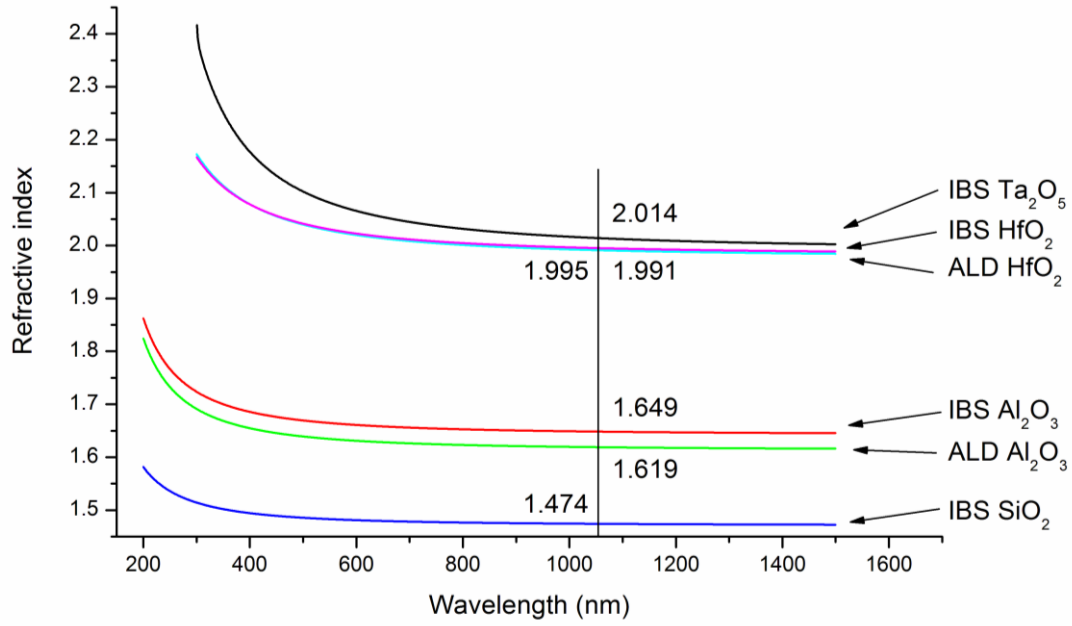


Fig. 40. Dispersion of different film materials.

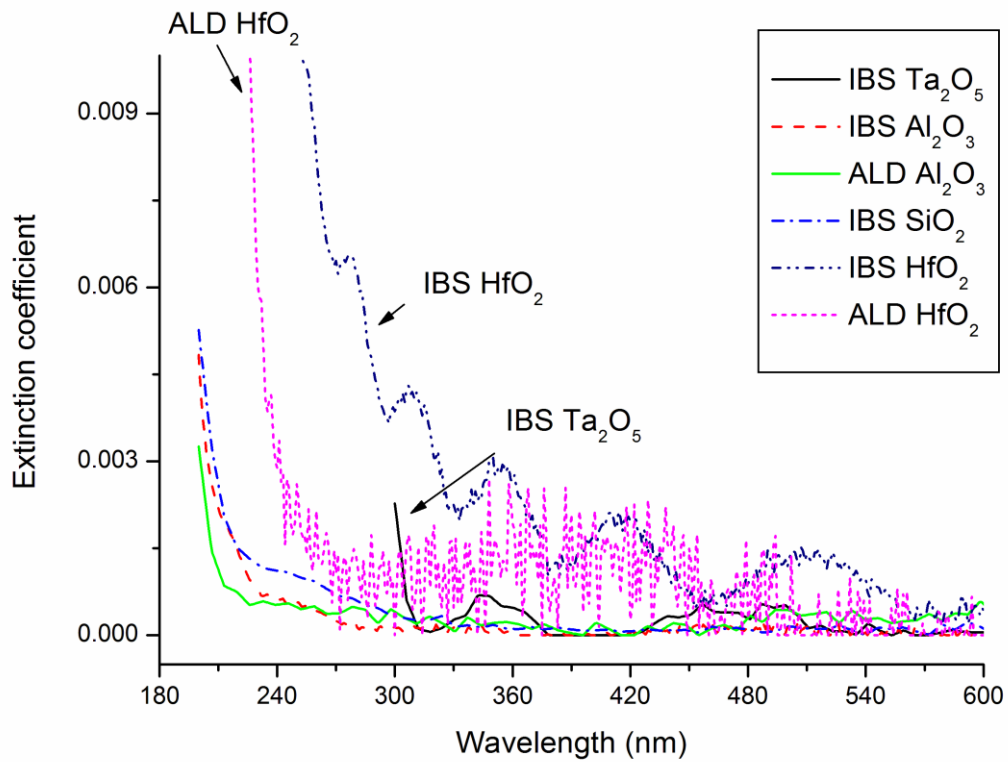


Fig. 41. Extinction coefficient of different film materials.

The extinction coefficients are displayed in Fig. 41. Al₂O₃ and SiO₂ have absorption edge below 200 nm, while Ta₂O₅ has absorption edge at about 300 nm.

5.4. Comparison of ALD Al₂O₃ and HfO₂ with commonly used films

The Band gap energies of the films are compared in Table 10. Both ALD HfO₂ and Al₂O₃ are large gap materials. The absorption was tested with Laser Calorimetry at 1064 nm. Both ALD Al₂O₃ and HfO₂ have absorption 3-4 ppm, in which the substrate contributes about 1 ppm. The extinction coefficients are calculated and listed in Table 10. The ALD films are proper materials for low loss laser applications. IBS SiO₂ and Al₂O₃ have also small absorption. IBS HfO₂ has higher absorption probably because of stoichiometric mismatch.

Table 10. Band gap energies (reference [136]) and extinction coefficients (at 1064 nm) of different film materials.

Material	IBS Ta ₂ O ₅	IBS HfO ₂	ALD HfO ₂	IBS Al ₂ O ₃	ALD Al ₂ O ₃	IBS SiO ₂
E_{gap} (eV)	3.8	5.1	5.5	6.5	6.5	8.3
k_{1064}	3.3×10^{-6}	3.4×10^{-5}	2.6×10^{-6}	1.0×10^{-6}	9.6×10^{-7}	6.7×10^{-7}

The characteristic damage curves of different materials are compared in Fig. 42. IBS SiO₂ and the 300°C annealed ALD Al₂O₃ have the highest LIDT among the available materials. The LIDT of ALD HfO₂ is distinctively lower than Al₂O₃, but still higher than Ta₂O₅, EBE or IBS HfO₂.

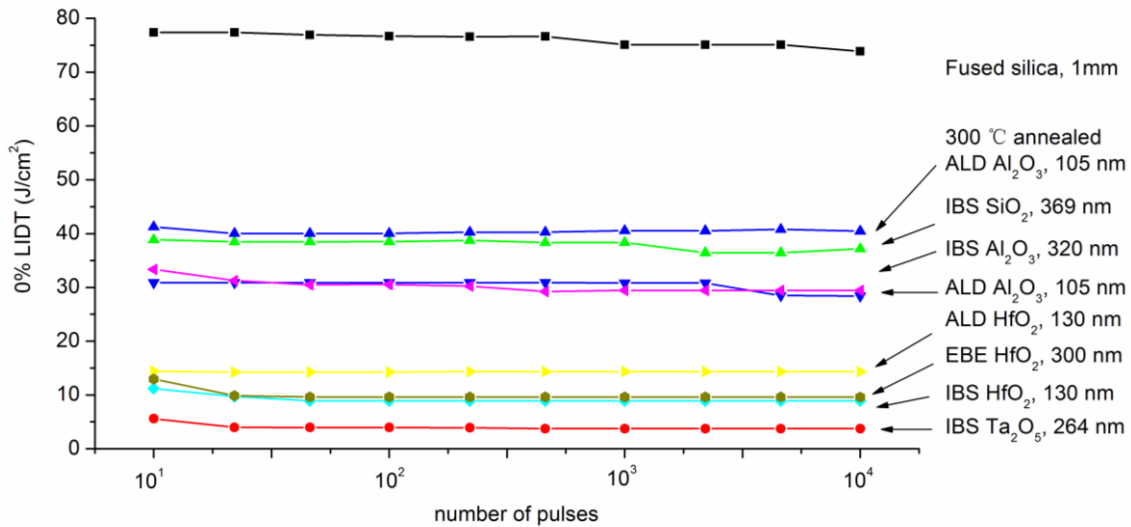


Fig. 42. Characteristic damage curves of different film materials (1 ω).

The damages of the films are induced by defects. The morphology detectable by 500x Nomarski Microscopy has dimension about 10 μ m. The IBS films have stronger adhesion, leading to damage morphologies with unclear border.

The tensile stress of ALD Al₂O₃ and HfO₂, however, is as high as hundreds of MPa. For thick coatings, the stress would lead to cracking or peeling off. One of the

substrates coated with about 5 μm ALD film is shown in Fig. 43. The films are peeled off from the substrate as fragments. The stress has to be carefully treated in an optical application.

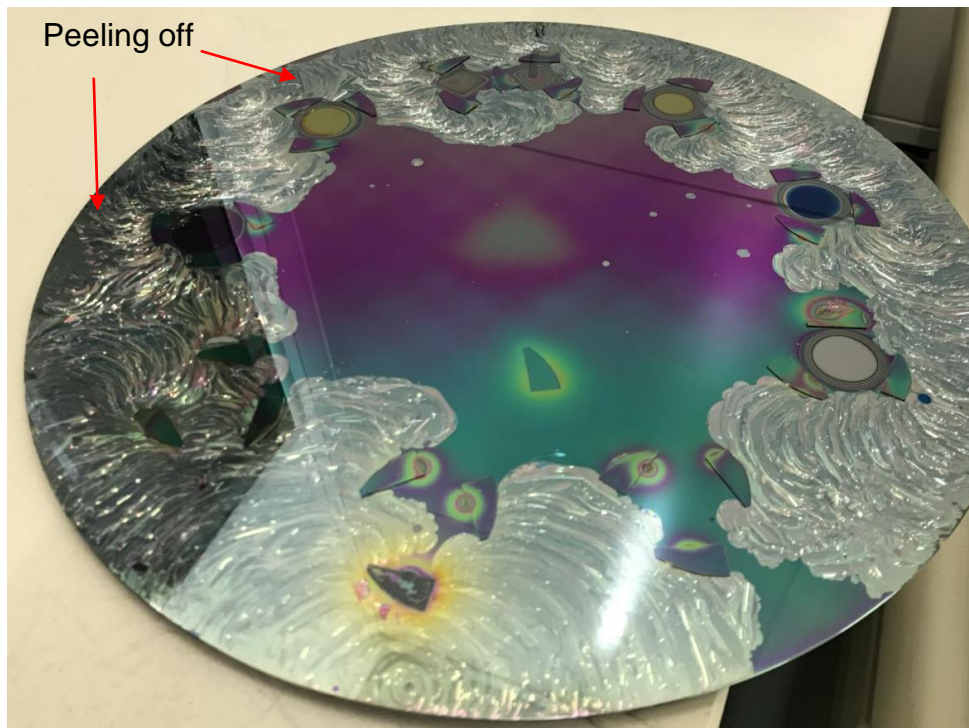


Fig. 43. Peeling off of the thick ALD films (5 μm).

5.5 Summary

ALD Al_2O_3 and HfO_2 single layers are compared to IBS Al_2O_3 and HfO_2 , respectively. The detailed characteristic is summarized in Table 11. The ALD films are distinctive for the following features:

- ♦ High thickness resolution, able to deposit film as thin as about 0.11 nm;
- ♦ Uniform without baffle correction;
- ♦ Large band gap energy and low absorption;
- ♦ Tensile stress;
- ♦ Rather high damage threshold.

Table 11. Characterization of ALD Al_2O_3 and HfO_2 compared to IBS single layers.

	Fused silica	ALD Al_2O_3 (300°C anneal)	IBS Al_2O_3	ALD HfO_2	IBS HfO_2
n (1 ω)	1.46	1.62	1.65	1.99	1.99
GPC (nm/cycle)	/	0.110 \pm 8%	/	0.106 \pm 7%	/
Uniformity (60mm)	/	>99%	/	>99%	/
E_{gap} (eV)	/	6.5	6.5	5.5	5.1
Stress (MPa)	/	Tensile 350-600	Compressive (-)300-(-)500	Tensile 800-1000	Compressive (-)300-(-)600
Extinction coefficient 1 ω	1.3×10^{-10}	9.6×10^{-7}	1.0×10^{-6}	2.6×10^{-6}	3.4×10^{-5}
LIDT, 1 ω , 10 pulses (J/cm ²)	77	41	33	14	13

6. ALD anti-reflection coatings for harmonics of Nd: YAG lasers

Nd:YAG (neodymium-doped yttrium aluminum garnet; $\text{Nd:Y}_3\text{Al}_5\text{O}_{12}$) is one of the most common types of laser crystals, and is used for many different applications. Nd:YAG typically emits light with a wavelength of 1064 nm (1ω). The high-intensity pulses may be efficiently frequency doubled to generate laser light at 532nm (2ω), 355nm (3ω), 266nm (4ω) or higher harmonics.

In this chapter, ALD Al_2O_3 and HfO_2 are used to compose anti-reflection coatings for different harmonics 1ω , 2ω , 3ω and 4ω of the Nd: YAG laser. The properties of anti-reflection coatings are qualified using the 1ω , 2ω , 3ω and 4ω lasers, respectively, and compared to those of IBS anti-reflection coatings.

6.1 Coating design

Double layer anti-reflection coatings composed of ALD HfO_2 and Al_2O_3 were designed. The characteristic matrix of the design was in the form of equation (8), in which the layer thickness d_1 and d_2 were the variants. The transmittance for a combination of $[d_1, d_2]$ was calculated according to equation (9). The proper $[d_1, d_2]$ combination was optimized by annealing method.

The GPC of ALD HfO_2 and Al_2O_3 listed in Table 11 was used to calculate the film cycles.

6.2 Spectral characterization

The transmittance of the 1ω , 2ω , 3ω and 4ω anti-reflection coatings are shown in Fig. 44. The measured spectra of ALD coatings match the designed curves very well, and the spectra have the transmittance peaks at the specific wavelengths. The measured 1ω , 2ω and 3ω transmittance including rear-surface reflection approximates the ideal value 96.5% for fused silica substrates with a single-side anti-reflection coating. It indicates a precise control of the ALD film thickness without in situ monitoring.

However, the measured and designed spectra do not overlap precisely. Recalculation shows an error of 6 nm in the HfO_2 layer thickness in the 1ω anti-reflection coating, while errors less than 2 nm in the other film layers. This experiment indicates that ALD is advantageous over IBS in precise thickness control when the film is thin, but shows disadvantage in thick films without an in-situ monitor.

6.2. Spectral characterization

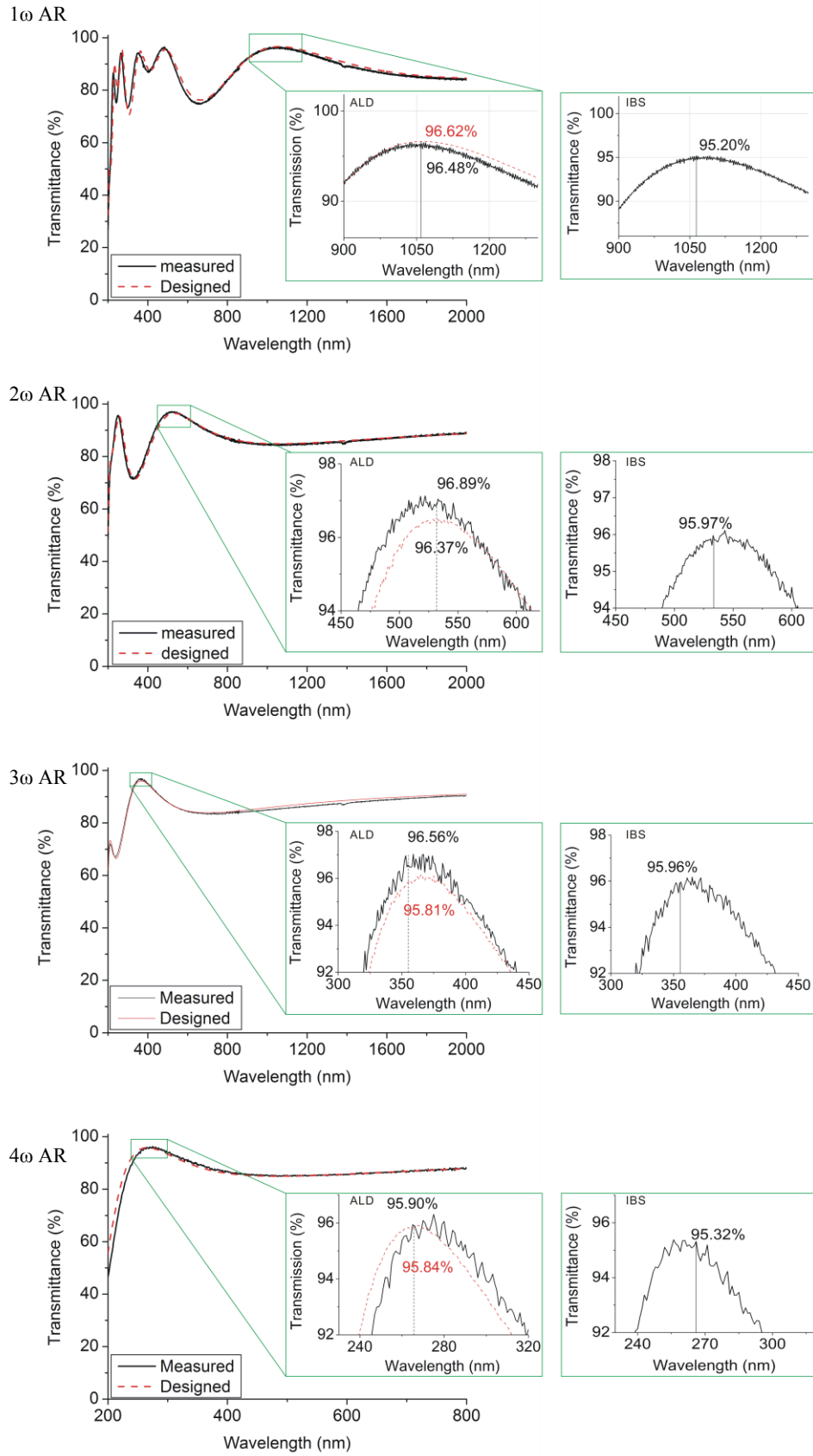


Fig. 44. Transmittance of ALD and IBS anti-reflection coatings.

6.3 Stress

The ALD anti-reflection coatings have concave profiles, and the IBS coatings have convex profiles, as shown in Fig. 45. This is consistent with the tensile stress of ALD single layers and the compressive stress of IBS films.

The coatings have individual stress, different from each other. While the error is one of the factors, it also indicates the complex relationship of stress and film thickness. The error is contributed mainly by the flatness of substrate, about 10%.

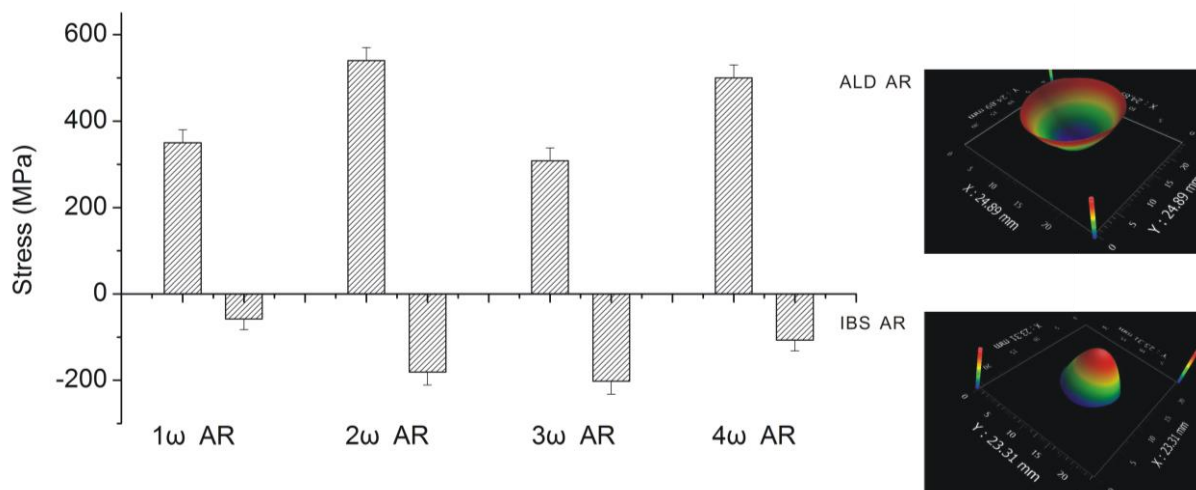


Fig. 45. Stress of the anti-reflection coatings.

6.4 Absorption

The 1ω, 2ω, 3ω and 4ω anti-reflection coatings are characterized by 1ω, 2ω, 3ω and 4ω Laser Calorimetry, respectively. The results are shown in Table 12. For 1ω and 2ω, the ALD films have smaller absorption than IBS anti-reflection coatings, while for 3ω and 4ω, the ALD films have larger absorption than the IBS coatings.

Table 12. Absorption of the anti-reflection coatings.

	1ω	2ω	3ω	4ω
ALD AR (ppm)	~1	9.3	597	6900
IBS AR (ppm)	4.5	32.8	65	590

6.5 LIDT

The LIDT of 1ω, 2ω, 3ω and 4ω anti-reflection coatings are characterized by the 1ω, 2ω, 3ω and 4ω Laser, respectively. The damage probabilities of the ALD and IBS coatings irradiated by 10 pulses are compared in Fig. 46.

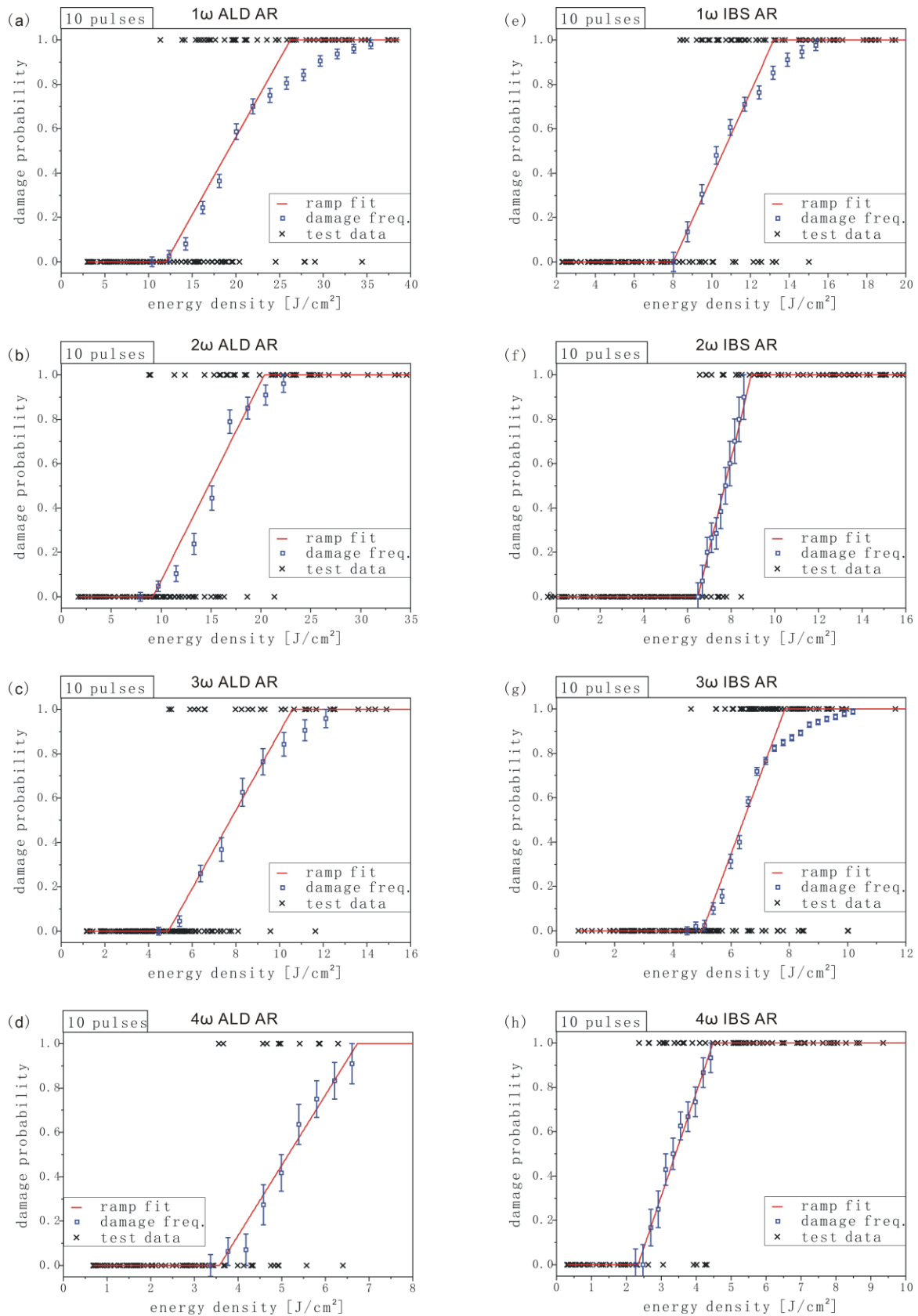


Fig. 46. 10 pulse damage probabilities of ALD and IBS Anti-reflection coatings at different harmonics of Nd:YAG laser.

The coatings have lower LIDT at higher harmonics of the laser due to the larger photon energy. The ALD anti-reflection coatings have generally higher LIDT than the IBS coatings. Moreover, the highest survival fluences of the ALD coatings are much larger than of the IBS coatings, indicating the potential of promoting the LIDT of ALD coatings.

The damage probabilities of the ALD anti-reflection coatings are similar to those of the ALD HfO_2 single layer film. It indicates that the LIDT of the AR coatings is mainly restricted by the HfO_2 film.

The characteristic damage curves of the ALD and IBS anti-reflection coatings are compared in Fig. 47. The ALD coatings have generally higher LIDT than IBS coatings. The 3 ω IBS and ALD AR have similar LIDTs, though 3 ω IBS AR has much lower absorption than ALD AR. It indicates the dominance of defects on LIDT.

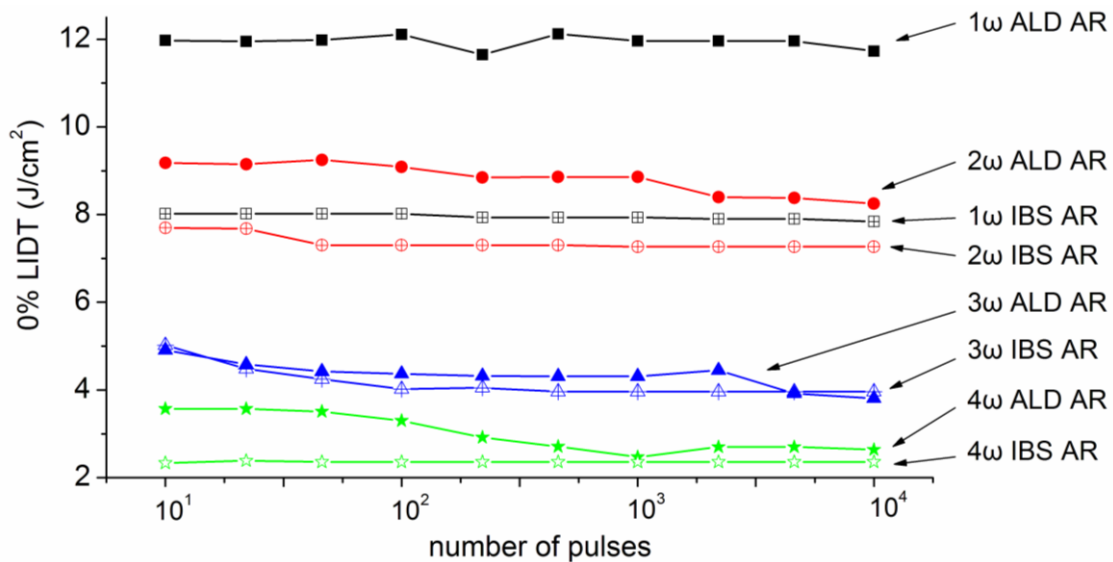


Fig. 47. Characteristic damage curves of ALD and IBS anti-reflection coatings.

6.6 Damage Morphology

The morphologies of the damage sites were characterized with Nomarski Microscopy, as shown in Fig. 48. The damages are caused by single pulse unless notified exceptionally.

The morphologies of either ALD or IBS anti-reflection coatings are mainly pits scattered irregularly within the laser spot. The pits are about 1-10 μm in diameter. At higher fluences, the morphologies exhibit scalds and pits connected with each other. It indicates that the damages of the coatings are induced by defects, which have

much lower damage threshold than the inertial film materials. At higher fluences, more material is burnt around the defects.

The morphologies of the coatings irradiated by higher harmonic laser have smaller but denser pits than the lower harmonic laser. It indicates that more defects are included in the films that interact with radiation of the higher harmonic laser.

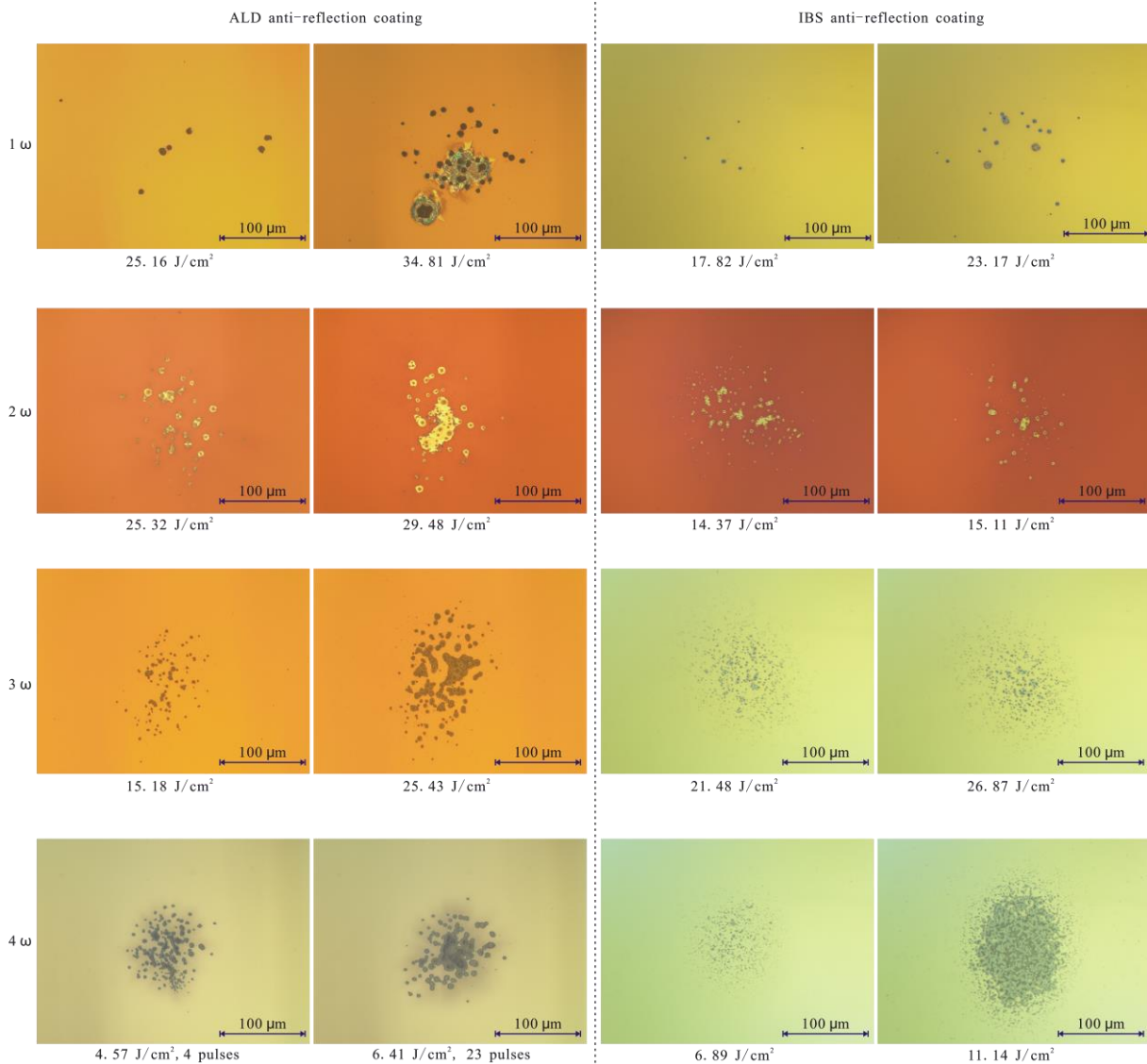


Fig. 48. Damage morphologies of ALD and IBS anti-reflection coatings at different harmonics of Nd: YAG laser.

6.7 Discussion

The damage of both ALD single layers and anti-reflection coatings are induced by defects according to the damage morphologies. This is consistent with the general

opinion of damage mechanisms of ns laser pulses [138]. This text provides findings on how these mechanisms also apply for ALD films.

The LIDT of both the ALD and IBS anti-reflection coatings can be linearly fitted with the photon energy of the testing laser, as shown in Fig. 49. Extrapolation of the fit to abscissa is about 5.5 eV, the band gap energy of ALD or IBS HfO_2 . As discussed in the above section, the LIDT of anti-reflection coating is limited by the HfO_2 film layer.

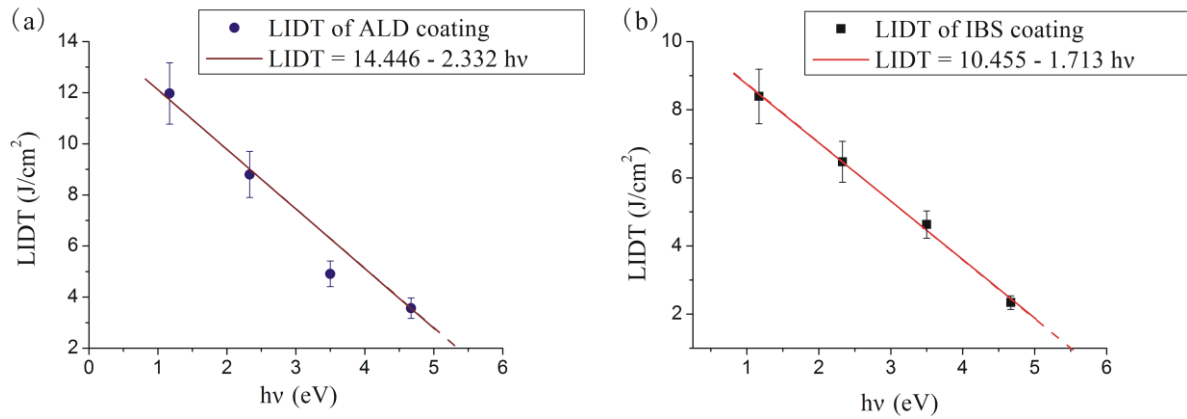


Fig. 49. LIDT plot with irradiating photon energy. (a) ALD anti-reflection coating; (b) IBS anti-reflection coating.

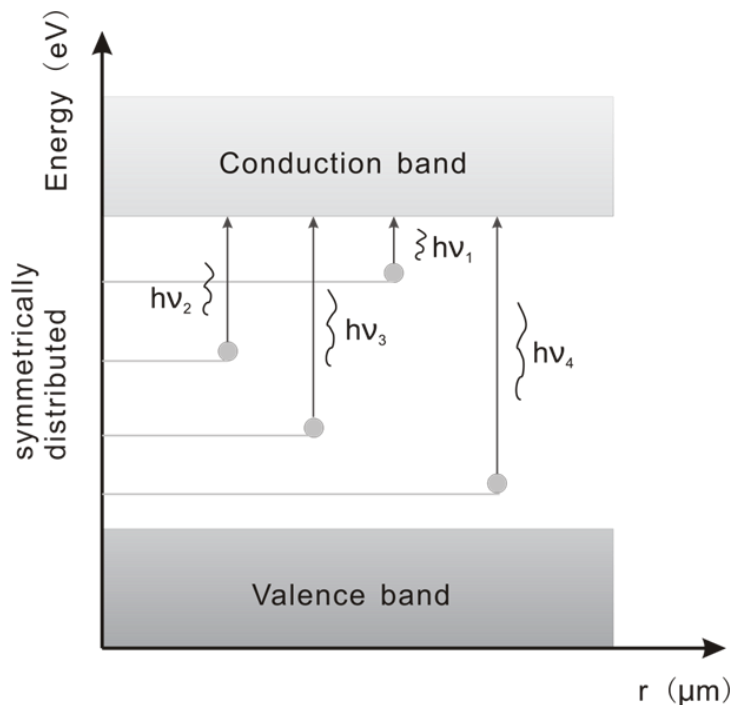


Fig. 50. Model of intra-band defects.

The defects have probably the intra-band energy levels between valence band and conduction band shown in Fig. 50. The electrons on the defect energy levels can be excited by the incident photons, forming free electrons that promote local absorption. The gradient absorption would induce laser damage either by local temperature or thermal tension. This assumption, however, needs to be certified by more experiments.

6.8 Summary

Anti-reflection coatings at different harmonics of Nd: YAG laser are prepared by ALD. The ALD process exhibits excellent film thickness control by the self-terminating feature. For thin film stacks, the ALD technique saves the expense largely without in-situ monitoring. The error of the film thickness is about 1%. For thicker film stacks such as filters, however, the error might cause deviation of the spectrum, and the in-situ monitoring might be indispensable.

Compared to IBS coatings, the ALD anti-reflection coatings have mainly the following features:

- ♦ ALD coatings have tensile stress;
- ♦ ALD coatings have low absorption and rather high LIDT.

The detailed properties of the anti-reflection coatings are summarized in Table 13.

Table 13. Summary of the properties of ALD and IBS AR for different harmonics of Nd: YAG laser.

	Transmittance (%)	Absorption (ppm)	10 pulse LIDT (J/cm ²)	Stress
1 ω ALD AR	96.5	~1	11.97	
2 ω ALD AR	96.9	9.3	9.18	Tensile
3 ω ALD AR	96.6	597	4.91	300 - 500 MPa
4 ω ALD AR	95.9	6900	3.57	
1 ω IBS AR	95.2	4.5	8.02	Compressive
2 ω IBS AR	96.0	32.8	6.47	(-)50-(-)200
3 ω IBS AR	96.0	65	5.02	MPa
4 ω IBS AR	95.3	590	2.34	

7. ALD Al₂O₃ acting as capping layer against vacuum-air-shift

ALD Al₂O₃ has been reported as gas diffusion barriers for organic light-emitting devices [139]-[144], field effect transistors [145], solar cells [146][147], and food packaging industry [148]. In optical application, ALD Al₂O₃ was reported to stabilize the refractive index of nano-porous SiO₂ [149]. ALD Al₂O₃ could be used as moisture barrier because of the high film density, which was however not clarified. In this chapter, ALD Al₂O₃ is studied as capping layer to protect optical coatings from environmental influences. It is demonstrated with the example of the vacuum-air-shift of an EBE dual-wavelength high-reflector. Thermal-shift is studied to further validate the high density of ALD coatings.

7.1 Experiment

A dual-wavelength high reflector (DWHR) for 532 nm and 1064 nm was deposited by Electron beam evaporating Ta₂O₅ and SiO₂, which are commonly used materials in dielectric optical coatings.

Four samples numbered with M1, M2, M3 and M4 were prepared simultaneously in a deposition run. The substrate temperature was kept at 200-300 °C. Sample M1 and M2 were used to verify the vacuum-air-shift without a protective overcoat, while M3 and M4 were capped with 100 nm of ALD Al₂O₃. The ALD film was added in a chamber with a temperature of about 200 °C and a pressure about 1.1 mbar. The samples were kept in the chamber for 5 minutes.

The vacuum-air-shift was tested with a broad band optical monitor (BBM) developed in Laser Zentrum Hannover [4]. The BBM was calibrated with a spectrometer, able to measure the transmittance spectrum in vacuum 3×10^{-6} mbar [150]. Sample M4 was then dipped in water for 60 hours to expose the multilayer film to a maximum of water and to verify the protective function of the capping layer. The vacuum-air-shift of capping layers with different thicknesses was tested.

The surface of each sample was characterized with a laser scanning microscope (LSM) under 500× magnification to determine the surface roughness in an area of 240×180 μm². The film structure of M4 was characterized by a Scanning Electron Microscope (SEM) under 120,000× magnification.

For further analysis of the capping effect, the vacuum-air-shift of DWHR protected by 3 nm, 10 nm and 20 nm ALD Al_2O_3 was compared to the unprotected multilayer. The temperature-shift of ALD films was tested by measuring the spectrum of an ALD $\text{HfO}_2/\text{Al}_2\text{O}_3$ anti-reflection coating at different temperatures.

7.2 Results

The transmittance spectra of M1 (without capping layer) measured in atmosphere and vacuum are shown in Fig. 51(a). Compared to that in atmosphere, the spectrum of the DWHR in vacuum shows a vacuum-to-air blue shift of 22 nm near wavelength 1000 nm. M2 has the same spectrum and vacuum-air-shift as M1, revealing a reproducibility of the experiment.

The spectra of M3 (with capping layer) are shown in Fig. 51(b). The spectrum measured in atmosphere overlaps with that in vacuum. It indicates the moisture isolation of the ALD capping layer as the optical thickness is not influenced by environmental variation.

M3 shows the same high-reflection bands at 490-540 nm and 950-1200 nm with M1 in vacuum, indicating the desorption of moisture in ALD vacuum chamber before deposition. In the wavelength range 700-900 nm, M3 has a different spectrum compared to M1, due to the optical influence of the Al_2O_3 overcoat.

The spectra of M4 (with capping layer) measured before and after dipping in water for 60 h are shown in Fig. 51(c). The spectrum after dipping does not shift to the red, but overlaps with that before dipping completely. The capping Al_2O_3 layer does not degrade but prevents the adsorption of moisture over time, indicating the sustainability of the capping layer.

Surface characterization shows that the DWHR without capping layer has average roughness 23.5 ± 1 nm, while the DWHR with capping layer has roughness 16.8 ± 1 nm. It indicates the denser film structure of ALD Al_2O_3 layer than EBE multilayers.

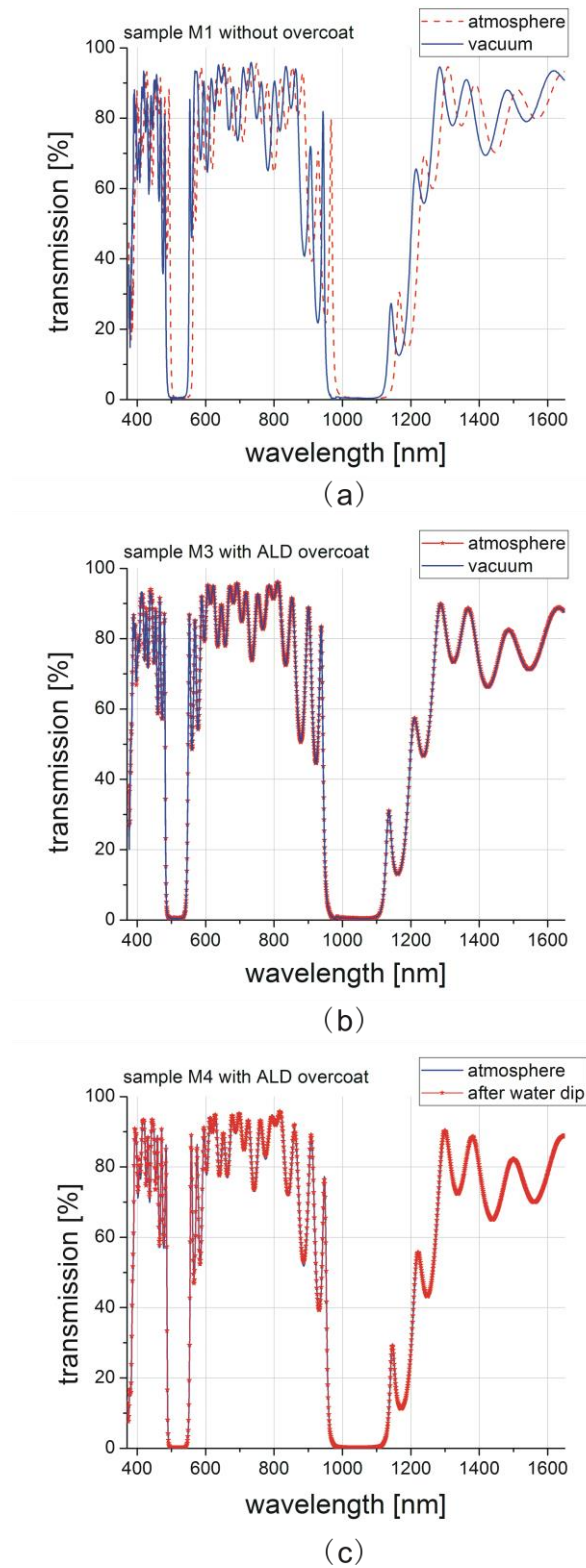


Fig. 51. Spectra of samples. (a) M1 (without capping layer) measured in atmosphere and vacuum; (b) M3 (with capping layer) measured in atmosphere and vacuum; (c) M3 (with capping layer) measured in atmosphere before and after dipping in water.

The capping effect of ALD Al_2O_3 with different thickness is displayed Fig. 52(a). The unprotected sample has the largest vacuum-air-shift, about 22 nm at wavelength 1000 nm, while the 20 nm Al_2O_3 protected sample has no vacuum-air-shift. 10 nm ALD Al_2O_3 is found to have a good capping effect against vacuum-air-shift. The capped mirrors show spectra blue shifted, indicating that moisture was lost in the ALD chamber before deposition. The effect of capping layer with different thicknesses against vacuum-air-shift is plotted in Fig. 52 (b).

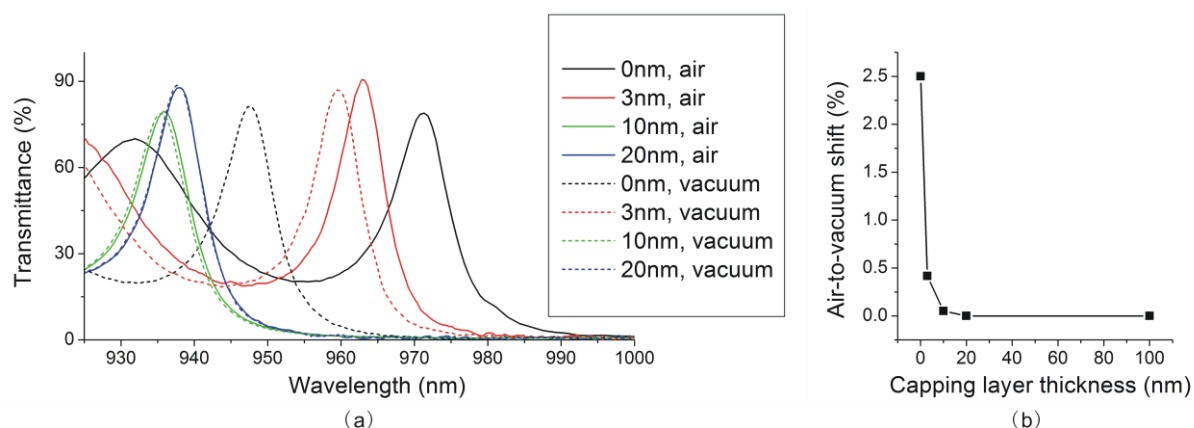


Fig. 52. Vacuum-air-shift of DWHR protected by ALD Al_2O_3 of different thickness. (a) The spectra measured in air and vacuum; (b) The Vacuum-air-shift plot versus capping layer thickness.

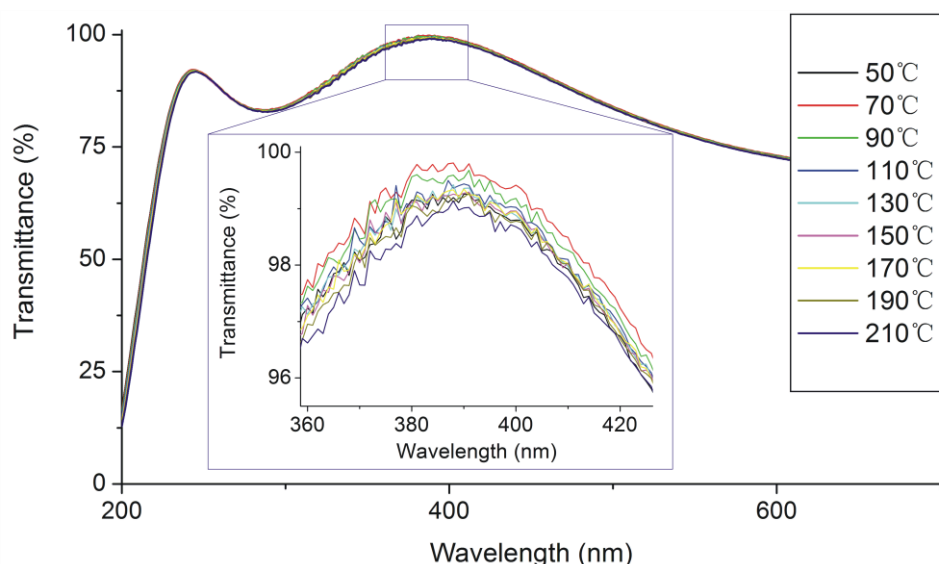
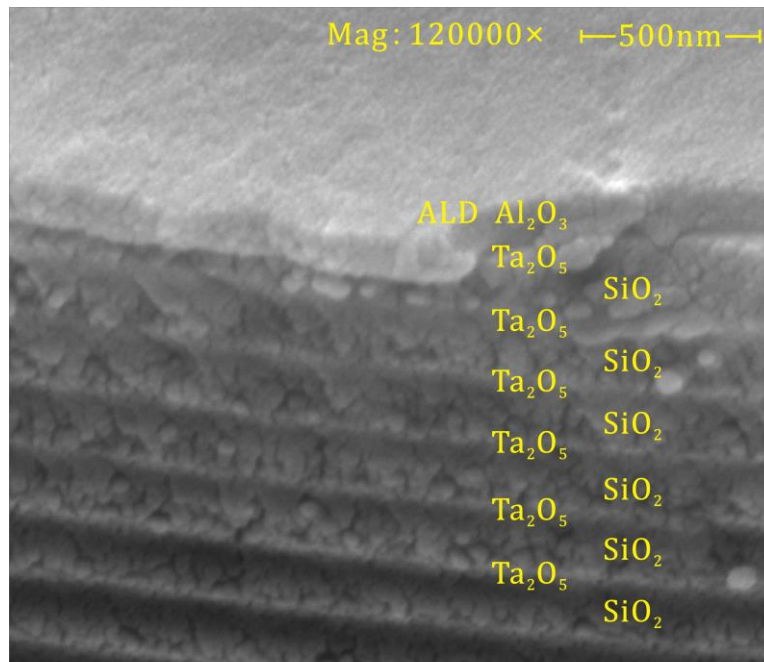
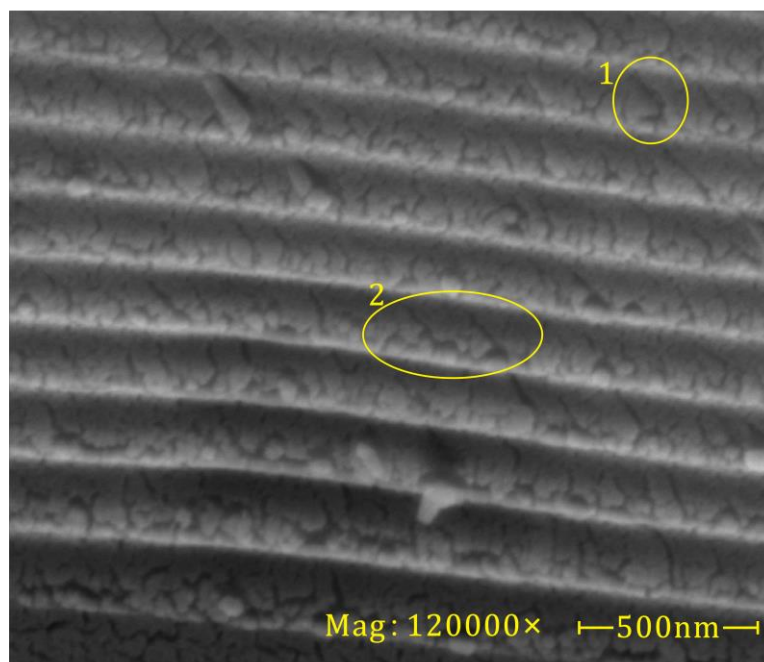


Fig. 53. Temperature shift test of the ALD $\text{HfO}_2/\text{Al}_2\text{O}_3$ anti-reflection coating.

The spectra of the ALD anti-reflection coating deposited with HfO_2 and Al_2O_3 at different temperature are shown in Fig. 53. There is no discriminable shift of the spectrum at different temperature, verifying the dense structure of the ALD films.



(a)



(b)

Fig. 54. Film structure of EBE multilayer capped by ALD Al_2O_3 layer. (a) overview; (b) pores of EBE multilayers.

The SEM images of the film structure are shown in Fig. 54. The overview of the ALD Al_2O_3 layer and the EBE DWHR can be seen in Fig. 54 (a). The pores of ALD layer are hardly recognizable compared to those of EBE stacks. The grains and

pores in the DWHR can be observed clearly in Fig. 54 (b). The pores in SiO₂ layers have width between 10 and 20 nm, in comparison to the 100-200 nm size of grains.

7.3 Analysis

The different deposition mechanisms of EBE and ALD contribute to the different film densities. The kinetics of coating species after transportation to the substrate include: adsorption on the surface of the substrate or growing coating, diffusion over this surface, chemical reaction with local reactive ligands, and their release from the surface by thermal desorption.

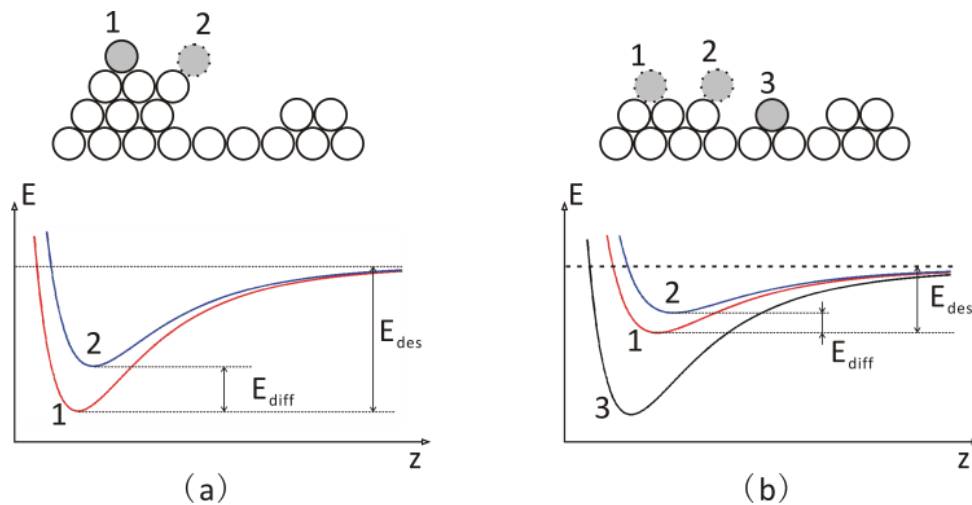


Fig. 55. Schematic diagram showing molecule in different adsorption sites and the corresponding potential energy E as a function of relative distance z to the surface molecule. (a) Ta_2O_5 or SiO_2 molecule in EBE; (b) TMA or H_2O molecule in ALD.

The energy potentials of different sites are illustrated in Fig. 55. During EBE coating growth, the Ta_2O_5/SiO_2 molecules condense onto the substrate or growing coating forming covalent bonds (position 1 in Fig. 55a), followed by diffusion or desorption. In the ALD process, the precursor molecules are physisorbed firstly by way of hydrogen bonding and van-der-Waals attraction (position 1 in Fig. 55b), which are much weaker than covalent bondings, and then switch to diffusion, desorption, or chemisorption through reaction with reactive ligands ($-OH$ or $-CH_3$) on the surface (position 3 in Fig. 55b). The reactive ligands will not regenerate once consumed until the next precursor exposing half cycle.

The surface diffusion rate r_{diff} of a specific molecule could be expressed by Arrhenius law [139]:

$$r_{diff} = \exp\left(-E_{diff} / k_B T\right) \quad (19)$$

Where k_B is the Boltzmann constant, T the substrate temperature, E_{diff} the potential energy difference in the equilibrium adsorption site (position 1 in Fig. 55 a and b) and in the transition saddle point (position 2 in Fig. 55 a and b). E_{diff} is related to melting point T_m . The ALD precursors TMA/H₂O or TEMA have much smaller E_{diff} than Ta₂O₅/SiO₂ in EBE process.

The diffusion rate of Ta₂O₅/SiO₂ is about 0.5%. The film molecules will thus essentially stick close to where they arrive, shadow the subsequent molecules, and lead to the porous film structure.

In case of ALD precursors, TMA/H₂O have diffusion rates as high as 40%. The molecules are therefore more likely to diffuse into the neighbor physisorption site, leading to weaker shadowing effects and therefore a dense film structure when the film grows layer by layer. The refractive index at 550 nm of ALD Al₂O₃ is 1.635, compared to 1.620 of the Al₂O₃ evaporated at 300°C [152].

When the TMA/H₂O molecules interact with the native pores in the EBE stacks with high depth-width ratio, more molecules and a longer exposure time are needed for the diffusion to cover the entire inner-wall surface. In this experiment, the precursor exposure pulse duration is set for growing a dense film on flat substrate, but insufficient for a deeper penetration of the pore structures. Therefore, the top portion of the pores is coated as the capping layer grows, closing the pore aperture gradually, and isolating the EBE stacks from the atmosphere moisture. In this context, the capping layer should have a thickness exceeding half of the pore width to achieve complete isolation of the underlying EBE-structure from the environment. Consequently, the thickness of the capping layer reaches a range that influences the coating spectrum. However, this effect can be pre-compensated in the coating design.

7.4 Summary

Vacuum-air-shift is a typical effect observed in many coatings with porous film structure deposited by conventional thermal evaporation. In the present study, a conventional Ta₂O₅/SiO₂ coating stack is covered by an ALD Al₂O₃ layer to isolate the grain pores in the columnar structure from atmospheric moisture. It is analyzed whether an ALD capping layer can be applied to a multilayer thin film structure to provide a protection from environmental changes or instabilities. Transmission

spectra in vacuum and atmosphere are compared to evaluate the vacuum-air-shift effect. The film structure of the coating capped with the ALD layer is characterized. Results indicate good performance of the ALD Al₂O₃ capping layer for the intended purpose. Both reproducibility and sustainability are verified, indicating a high potential of ALD Al₂O₃ as capping films. The capping effect of ALD Al₂O₃ with different thickness is evaluated. The temperature shift of an ALD anti-reflection coating is tested to verify the dense structure of the ALD films. Although IBS or IAD coating have also high film density [153], the high diffusion of ALD precursor enables an advantageous application of ALD Al₂O₃ as capping layer for objects with complex surfaces.

8. Stress compensated high power antireflection coatings

8.1 Introduction

Since the very beginning of laser technologies, one main subject is the development of laser systems operating at high power levels and improved beam quality [154][155]. The obstacle towards high power laser is the limitation in the power-handling capability of optical components. Among the various components for Nd: YAG lasers, optical coatings that form mirrors and polarizers are most easily to breakdown [156]. Improving the laser resistance of optical coatings is a continuing challenge.

On the other hand, wave-front specification of optical components are demanded in order to obtain sub-mm focused laser [157]-[159]. The stress of coatings needs to be carefully set, as the coating stress can either bend the glass substrate and change the wave-front or cause the coating to crack. Coatings with little stress are desired

Nowadays, the most widely used coatings for high power laser mirrors are electron beam evaporated (EBE) $\text{HfO}_2/\text{SiO}_2$ compositions [160]. HfO_2 is more resistive than the traditional high-index material TiO_2 [161], and laser conditioning could increase the $\text{HfO}_2/\text{SiO}_2$ damage threshold by 2× to 3× [162]. The stress of coatings could be adjusted by ion assisting deposition (IAD). It is rather difficult to promote the resistance further without damaging the wave-front.

Ion beam sputtering (IBS) is an enabling technology for modern thin film coatings [163]. IBS coatings exhibit superior properties such as: precise thickness control, high packing density, low absorption and high LIDT. A recent damage competition indicates that IBS has larger damage threshold than EBE or other techniques [164]. However, its application is inhibited in large optics of high power laser due to the severe compressive stress. Though post annealing is reported to release part of the IBS coating stress [165][166], it is difficult for a precise control.

Atomic layer deposition (ALD) coatings are also competitive in uniformity, low loss, high LIDT and precise thickness control. However, the severe tensile stress of ALD coatings sets an obstacle towards the application in large-size high power lasers.

In this chapter, a novel idea is presented to take advantage of the power handling abilities and opposite stress of IBS and ALD coatings. With ALD Al_2O_3 and IBS SiO_2 selected as high and low refractive index materials, coatings with compensated stress as well as high LIDT could be designed. IBS SiO_2 and ALD Al_2O_3 have been

individually well studied, possessing rather high LIDTs among a variety of optical materials. Moreover, precursors $\text{Al}(\text{CH}_3)_3$ and H_2O are prominent for ALD processes due to the high reactivity, thermal stability and rather safe reaction product.

In the following section, the derivation of the opposite stress in IBS and ALD coatings is analyzed at first. In section 8.3, the coating design concept taking advantage of IBS SiO_2 and ALD Al_2O_3 is depicted. In section 8.4 and 8.5, an anti-reflection coating composed of ALD Al_2O_3 and IBS SiO_2 is prepared and characterized. This chapter describes a coating concept with high LIDT as well as low stress, which might promote the output of solid state laser to a new level.

8.2 Stress analysis of IBS and ALD coatings

As it approaches the substrate, each film molecule exerts a force on the existing molecules on the substrate, either attractive or repulsive. The molecule cannot freely move in the horizontal direction due to limited diffusivity. The intermolecular forces would eventually reach a balance. In other words, the film layer is formed with a shrinking or expanding trend, as shown in Fig. 56. The substrate, however, prevents the shrinking or expansion of the film.

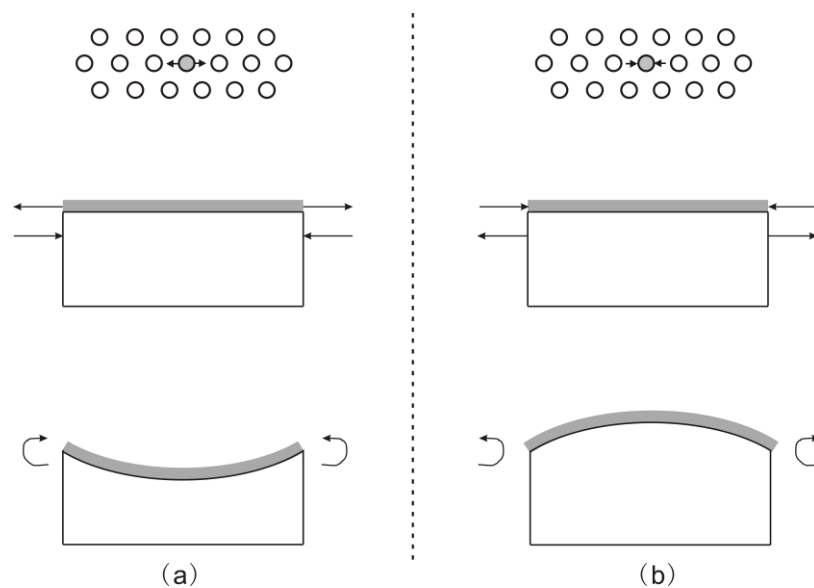


Fig. 56. Intermolecular force induced stress. (a) attractive force leading to tensile stress; (b) repulsive force leading to compressive stress.

The equilibrium requires that both forces and bending moments be balanced at any point of the interface. Take the attractive force in Fig. 56(a) for an example. The substrate is under the expansion force of the film, and balances it with repulsive force.

The bending moment is compensated by elastically bending of the substrate. Thus, attractive intermolecular force bends the substrate concave upward, named as tensile stress, and repulsive intermolecular force bends the substrate convex outward, named as compressive stress.

The intermolecular force is approximately described by Lennard-Jones function [167].

$$U_{LJ}(r) = \varepsilon \left[\left(\frac{r_m}{r} \right)^{12} - 2 \left(\frac{r_m}{r} \right)^6 \right] \quad (20)$$

Where r is the distance between the molecules, ε is the depth of the potential well, r_m is the balance distance at which the inter-particle potential is minimum and the inter-particle force is zero. The potential is composed of a repulsive term and an attractive term. The repulsive term at short range describes the Pauli repulsion due to overlapping electron orbitals, while the attractive term at long range depicts attraction such as covalent bonding, hydrogen bonding, Van der Waals force and so on.

In order to develop a simplified mathematic model, the harmonic oscillator potential is used to approximate the intermolecular potential.

$$U(r) = \frac{1}{2} k_e r^2 - \varepsilon \quad (21)$$

Where k_e is the elastic constant. k_e is determined by ε and r_m in Lennard-Jones function. The balance position is reset here as 0 for convenience, as illustrated in Fig. 57.

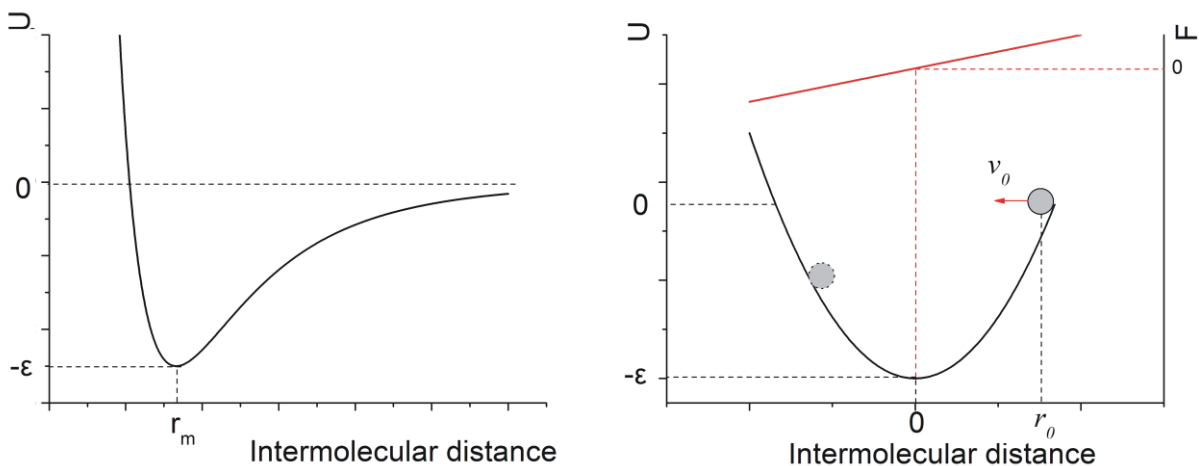


Fig. 57. Intermolecular potential. The bottom part could be approximated as harmonic oscillator potential.

During the coating process, the film molecule approaches the potential well from infinity with initial velocity v_0 , and then oscillates in the potential well. The interaction with the large number of molecules in substrate would damp the kinetic energy until a thermal oscillation. However, the thermal oscillation has much smaller amplitude, thus is not considered here. The movement equation of the molecule in the harmonic oscillator potential could be written as following:

$$\begin{cases} \frac{d^2 r}{dt^2} + 2\zeta\omega_0 \frac{dr}{dt} + \omega_0^2 r = 0 \\ r|_{t=0} = r_0 \\ \left. \frac{dr}{dt} \right|_{t=0} = v_0 \end{cases} \quad (22)$$

$$\omega_0 = \sqrt{k_e / m}$$

$$\zeta = c_d / 2\sqrt{mk_e}$$

Where r_0 is the initial position at which potential equals zero, and v_0 is the initial velocity of the coating molecule. ω_0 is the angular frequency determined by the elastic constant k_e and molecule mass m , ζ is the damping ratio. It is assumed that the damping force is proportional to the molecule velocity:

$$F = -c_d \cdot dr / dt \quad (23)$$

Solving equation (22), the mean position $\langle r \rangle$ can be expressed by equation (24). The detailed calculation is in Appendix I.

$$\langle r(t) \rangle = \frac{v_0 + 2r_0\zeta\omega_0}{t \cdot \omega_0^2} (1 - e^{-\zeta\omega_0 t}) \quad (24)$$

The mean position could be either positive or negative, depending on the initial velocity v_0 . There are three cases as illustrated in Fig. 58.

- ♦ $|v_0| > 2r_0\zeta\omega_0$. The molecule has large velocity, leading to an intermolecular distance smaller than balance distance. In this case, the repulsive force dominates;
- ♦ $|v_0| = 2r_0\zeta\omega_0$. The intermolecular distance is exactly the balance distance, and the average force is zero;
- ♦ $|v_0| < 2r_0\zeta\omega_0$. The molecule has small velocity, leading to an intermolecular distance larger than balance distance. In this case, the attractive force dominates.

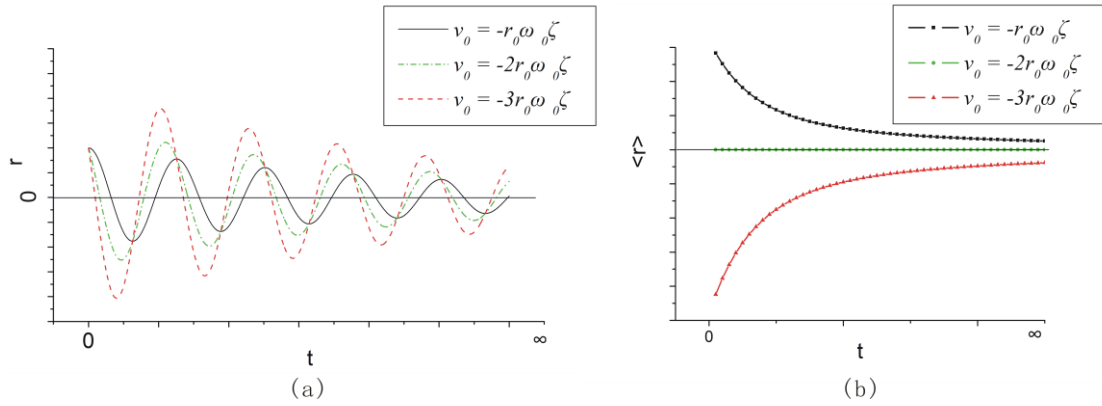


Fig. 58. (a) The trace of an impinging molecule with different initial velocities; (b) The mean position of an impinging molecule with different initial velocities.

In order to estimate the value of item $2r_0\zeta\omega_0$ of Al_2O_3 and SiO_2 , further assumption has to be made to the parameters.

1. The damp ratio is a variable between 0 and 1, depending on the damping force. It is rather difficult to clarify how fast the substrate damps the oscillation of the incoming molecule. The damp ratio 0.1, 0.5 and 1 are adopted in the calculation in Table 14.
2. The potential depth is assumed to be 1-3 eV. The exact potential depth of an amorphous film is hardly available, though some elements are reported [168]-[170]. The potential depth 0.1eV, 1 eV and 3 eV are adopted in Table 14.

Table 14. Estimation of the $2r_0\zeta\omega_0$ of Al_2O_3 and SiO_2 .

m (g/mol)	ε (eV)	ζ	$2\zeta\sqrt{\frac{2\varepsilon}{m}}$ (m/s)
50 (Al_2O_3)	1	0.1	392
	1	1	3920
	1	0.5	1960
	3	0.5	3394
	0.1	0.5	620
30 (SiO_2)	1	0.1	506
	1	1	5060
	1	0.5	2530
	3	0.5	4381
	0.1	0.5	843

8.3. Design of the stress-compensated AR coating

The typical parameters are calculated as in Table 14. Based on the above assumptions, Al_2O_3 and SiO_2 have $2r_0\zeta\omega_0$ probably between 400-5000 m/s.

In an IBS process the film molecules are emitted with kinetic energies as high as several 10 eV through the momentum transfer from impinging ions to the target. In EBE process, the film molecules are evaporated with kinetic energies few tenth eV through energy transfer from impinging electrons to the target. In ALD process, the precursor molecules arrive at the substrate at rates of hundreds of sccm carried by Ar. The initial velocity v_0 in each case are listed as Table 15. Compared to the average value of $2r_0\zeta\omega_0$, IBS is believed to produce compressive stress, EBE and ALD coatings should have tensile stress.

Table 15. Stress induced by molecule velocity in different coating process.

	IBS	EBE	ALD
initial velocity v_0	$\sim 10^4$ m/s	10 m/s	0.1 m/s
Intermolecular force	Repulsive	Attractive	Attractive
Stress	Compressive	tensile	tensile

Importantly, this model developed in this text provides a general insight of how stress occurs. The model is based on assumption and the parameters are far from precise values. After all, the conclusion can be drawn that though the temperature in each coating process might cause external stress, the intermolecular force plays the key role in determining the total stress.

8.3 Design of the stress-compensated AR coating

Of all the possible applications, anti-reflection coatings have had the greatest impact on technical optics. Double-layer coatings are essential for AR design. Varying the thickness of each layer, a combination could be found giving lowest reflectance. The characteristic matrix of a typical double-layer design is described in equation (8).

The strain of the layers exerted on substrate could be expressed by peak-to-valley value:

$$\frac{4E_s d_s^2}{3(1-\nu_s)D^2} \Delta PV = \sigma_1 d_1 + \sigma_2 d_2 \quad (25)$$

Where E_s , ν_s , d_s , D are Yong's modulus, Poisson ratio, thickness and aperture of the substrate, respectively. σ is the stress of the film layer.

8.3. Design of the stress-compensated AR coating

As could be seen in equation (8) and (25), varying the thickness of each layer by $\eta_i d_i = \lambda$ would not change the characteristic matrix, but would affect distinctively the peak-to-valley value. Theoretically speaking, if a pair of integers x, y could be found meeting equation (26), both the reflection and stress would be zero.

$$\sigma_1(d_1 + x \frac{\lambda}{\eta_1}) + \sigma_2(d_2 + y \frac{\lambda}{\eta_2}) = 0 \quad (26)$$

$$x, y = 0, 1, 2, 3, \dots$$

Normally, the suitable x and y would be very large, leading to a very thick coating design, which is not practical. However, there is usually a tolerance for error in an actual requirement. Besides, more than two layers could also be used as an initial design. The algorithm searching for suitable x and y is based on the simulated annealing method [171], as illustrated in Fig. 59.

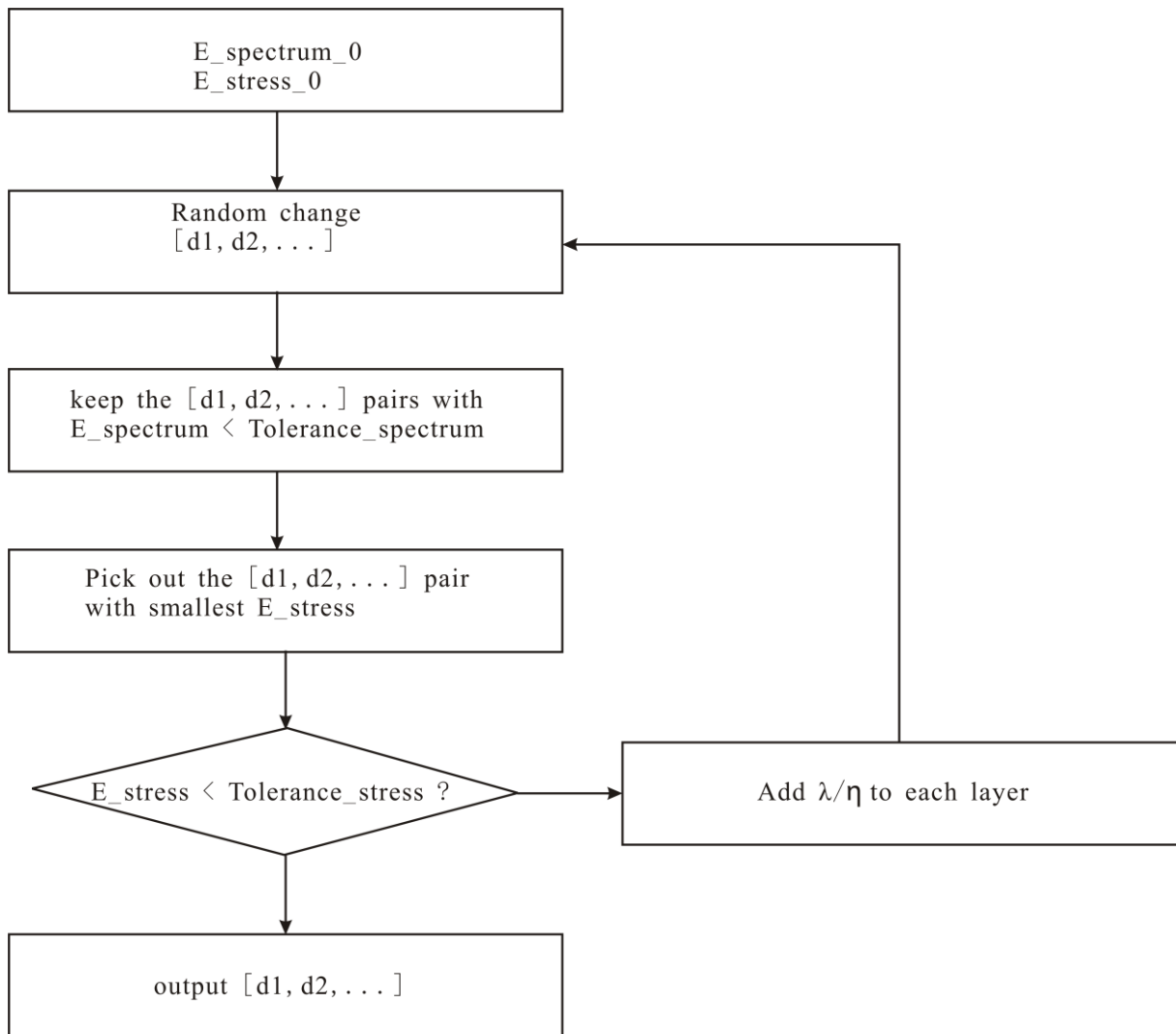


Fig. 59. Algorithm for designing a stress-compensated coating.

8.4 Experimental details

An anti-reflection coating at 980 nm was designed with compensated stress. According to previous experiment, ALD Al_2O_3 has tensile stress varying from 350-600 MPa, while IBS SiO_2 has compressive stress 400-470 Mpa. In this experiment, the average value of the film stress was adopted, that is, 414 Mpa of ALD Al_2O_3 , and (-)415 Mpa of IBS SiO_2 . The design was Sub/135 H 182L 178H 134L/Air.

The SiO_2 was deposited in an IBS machine. The film thickness was monitored with a broad band monitor. ALD Al_2O_3 was deposited without in-situ monitoring. The substrate was transferred between the IBS machine and ALD machine to be coated with IBS SiO_2 and ALD Al_2O_3 layers.

The transmittance at 980 nm was designed to be 100% excluding rear surface reflection. The stress was designed to be -3 MPa. The LIDT of the anti-reflection coating and single layers were measured at 532 nm according to ISO 21254. The beam frequency was 100 Hz. The beam diameter at $1/e^2$ of the maximum intensity was about 300 μm .

8.5 Results and analysis

8.5.1 Spectrum

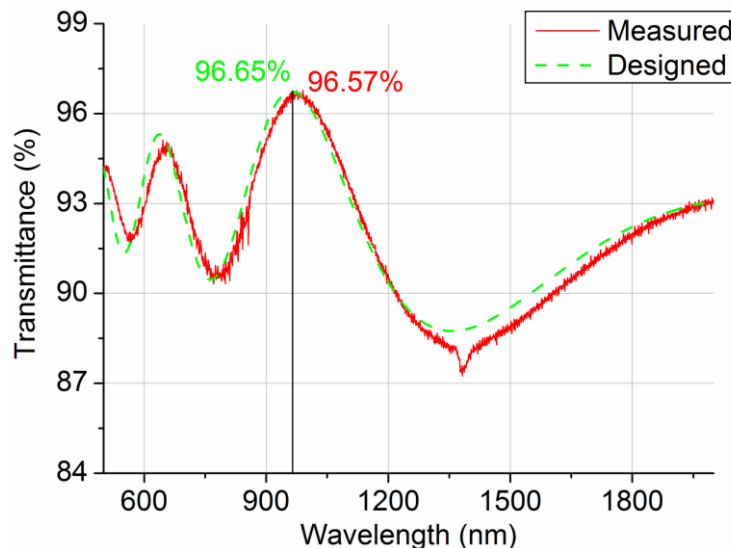


Fig. 60. The measured and designed spectra.

The transmittance in wavelength range [500, 2000] nm was measured and compared with the design, as shown in Fig. 60. The peak position is at 980 nm, consistent with the design. The peak transmittance is 96.57%, which is quite close to the designed

value including a rear surface reflection. The accordance of measured and designed spectra indicates the rather controllable film thickness. However, the spectra do not overlap. The recalculation indicates a thickness error of 8% in the ALD Al_2O_3 film layers. The GPC of the 1st Al_2O_3 layer is 0.112 nm/cycle while of the 2nd is 0.102 nm/cycle.

8.5.2 Stress

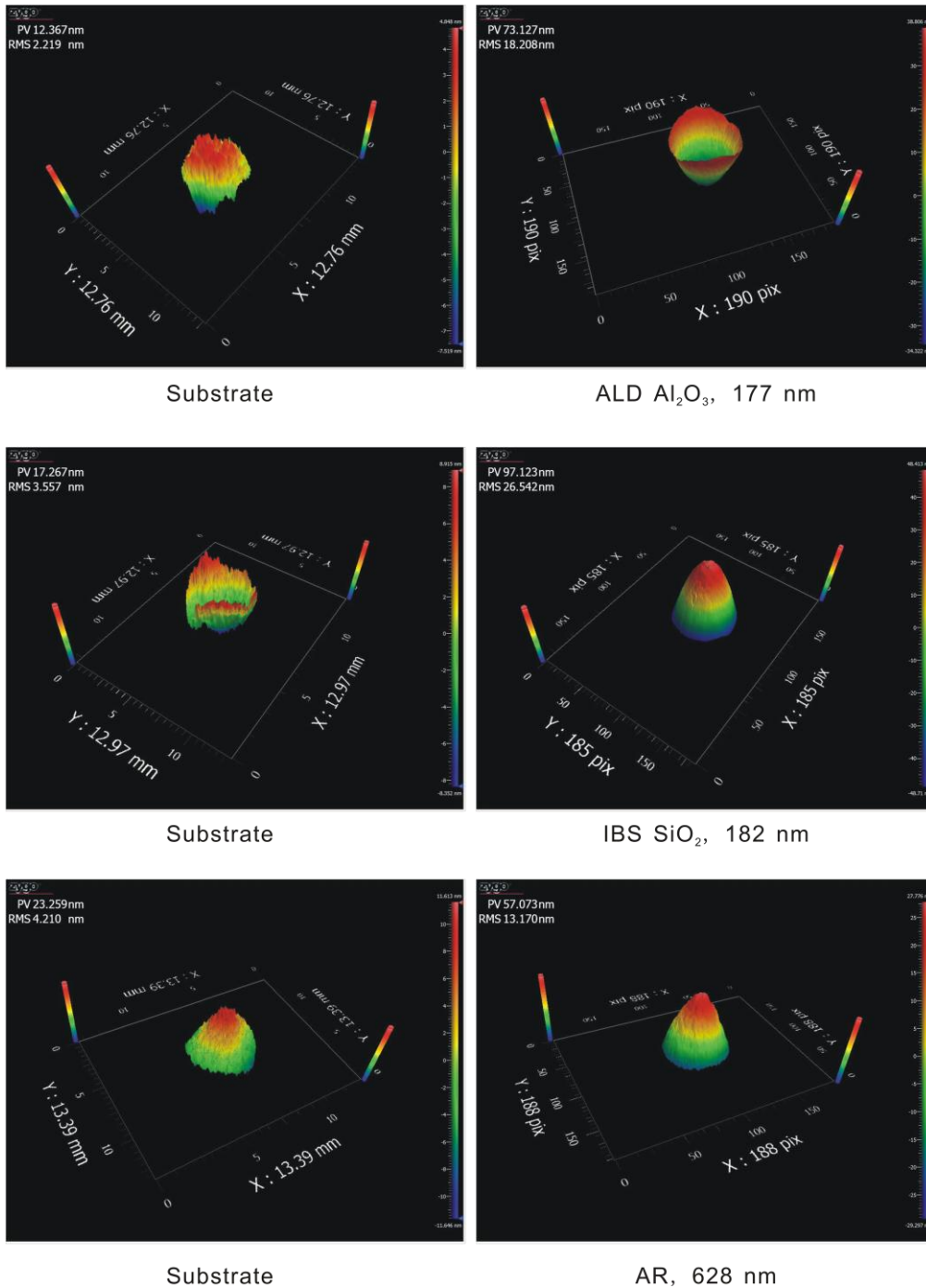


Fig. 61. Surface profile of the single layers and anti-reflection coating.

The surface profiles of the single layers as well as the anti-reflection coating are shown in Fig. 61. The profile at the rim is truncated to avoid obvious error, which is valid in principle if the substrate is flat. The anti-reflection coating has much smaller peak-valley value than the single layers in spite of the much larger film thickness. The stress values calculated according to Stoney's equation are listed in Table 16.

Both Al₂O₃ and SiO₂ single layer have stress several hundred MPa, while the anti-reflection coating has (-)38 MPa stress. Though much thicker than the single layers, the anti-reflection coating has much smaller stress due to the compensation.

The compensation is not perfect, residing certain stress to some extent. This is due to the error of the single layer stress. The single layers do not show the same stress as in the design, as listed in Table 16.

Table 16. Stress comparison of single layers and anti-reflection coating.

	ALD Al ₂ O ₃	IBS SiO ₂	ALD Al ₂ O ₃	IBS SiO ₂	AR coating
Film thickness (nm)	148	182	178	135	628
Diameter (mm)	12.5	12.5	12.5	20	12.5
ΔPV (nm)	63	-114	85	-152	-34
Stress (MPa)	302	-450	343	-315	-38

8.5.3 LIDT

The damage probabilities of IBS SiO₂ (135 nm), ALD Al₂O₃ (178 nm) and the stress compensated anti-reflection coating are displayed in Fig. 62. The damage probabilities are plotted versus fluence and fitted linearly. The extrapolation to the abscissa is defined as 0% LIDT, indicating the highest fluence that causes no damage.

For 10 pulses irradiation, IBS SiO₂ has LIDT about 35 J/cm², and the highest survival fluence is over 45 J/cm². For 10,000 pulses irradiation, the LIDT of IBS SiO₂ decreases distinctively till 15 J/cm², and no site survives the 30 J/cm² fluence. It indicates the fatigue effect of SiO₂ under the 2ω laser irradiation.

ALD Al₂O₃ has LIDT 15 J/cm² under irradiation of both 10 and 10,000 pulses. However, the highest survival fluence decreases distinctively when the film is irradiated with more pulses.

The anti-reflection coating has an LIDT of 10 J/cm² under irradiation of both 10 and 10,000 pulses, lower than the single layer films. The LIDT is probably induced by the defects at the film interfaces. The samples were moved between the ALD chamber

and IBS chamber, during which much more defects were expected. The defects are supposed to have higher absorption.

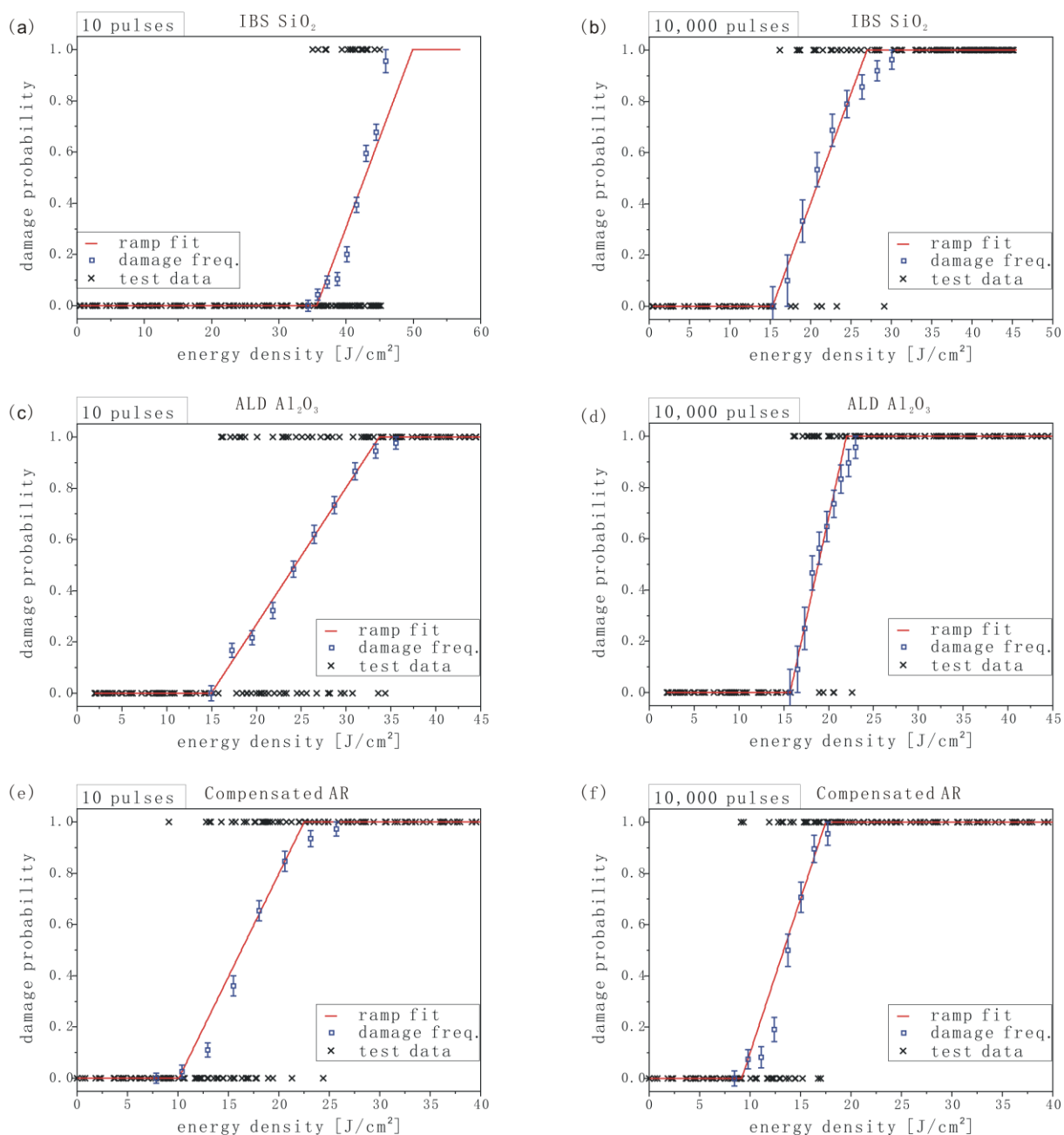


Fig. 62. Damage probabilities. (a)-(b) IBS SiO₂, 135 nm; (c)-(d) ALD Al₂O₃, 178 nm; (e)-(f) compensated anti-reflection coating.

The characteristic damage curves of the stress compensated anti-reflection coating is compared with ALD and IBS anti-reflection coatings, as shown in Fig. 63. Though much more defects are introduced during the movement between coating chambers, the stress compensated anti-reflection coating has the same LIDT as the ALD anti-reflection coating, and larger than IBS anti-reflection coating.

The 50% characteristic damage curves give more hint on the potential of higher LIDT. If the additionally introduced defects are eliminated, theoretically speaking, the LIDT of the stress-compensated anti-reflection coating could reach that of the ALD Al_2O_3 single layer.

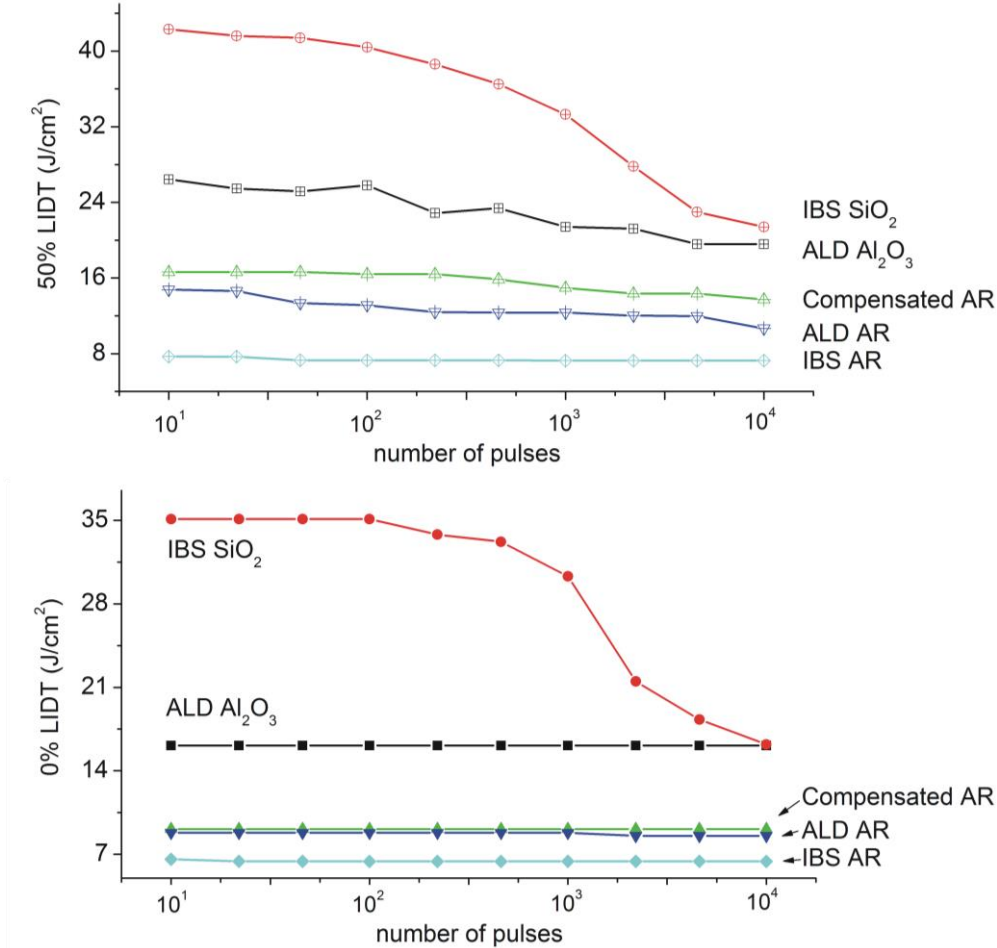


Fig. 63. Characteristic damage of the anti-reflection coatings as well as the single layers.

The typical damage morphologies are illustrated in Fig. 64. IBS SiO_2 exhibits small and dense pits, while ALD Al_2O_3 exhibits pits around the damage centers. The anti-reflection coating shows damage pits scattered irregularly within the laser spot. However, the damage pits of the anti-reflection coating are more like peeling-off pits, different from the single layers. The stress mismatch of ALD Al_2O_3 and IBS SiO_2 might account for the different appearance of the pits. The damage morphologies indicate that the damage of the anti-reflection coating is induced by the defects introduced externally. There is much potential for improvement of the LIDT, if the

defects concentration could be reduced. For example, it would be helpful to deposit the IBS SiO₂ and ALD Al₂O₃ in the same chamber.

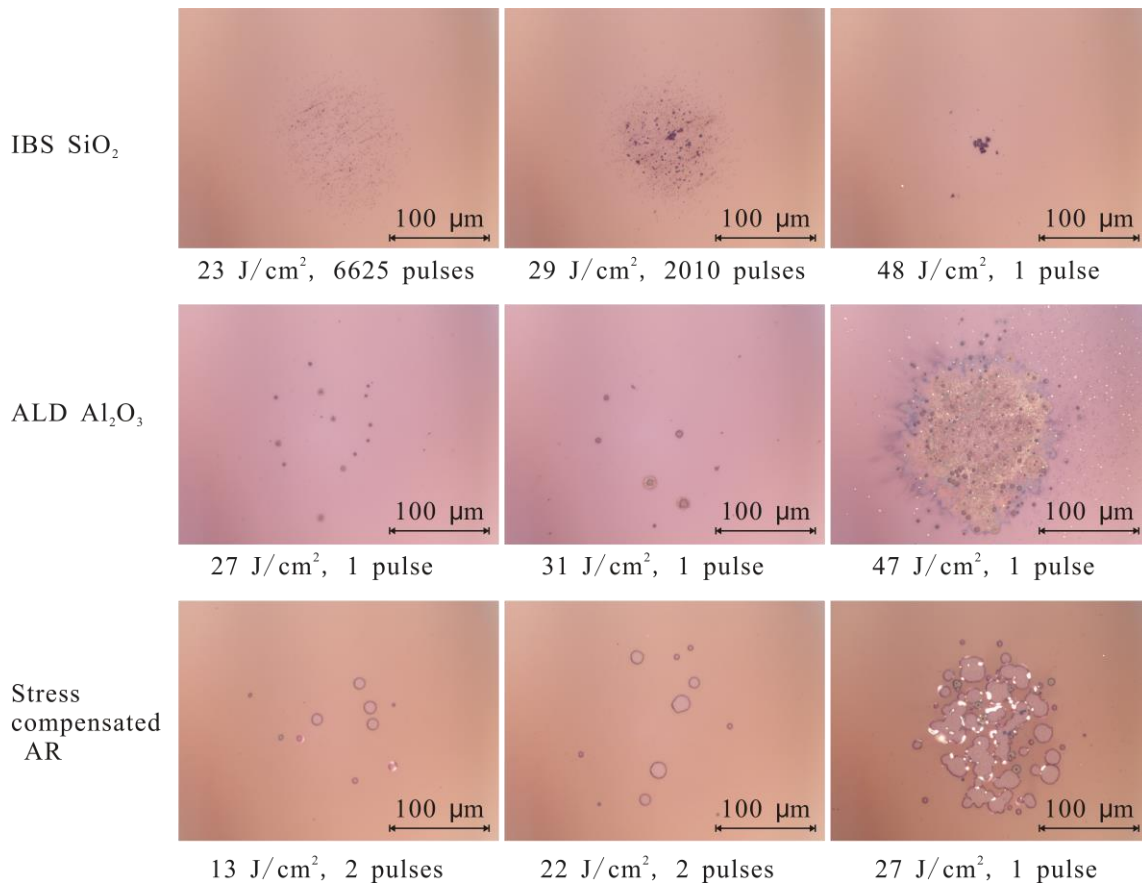


Fig. 64. Damage morphologies of the single layers and the stress compensated anti-reflection coating.

8.6 Discussion

It is a promising trend to design optical coatings meeting the spectrum, stress as well as high LIDT requirements by use of ALD Al₂O₃ and IBS SiO₂. According to the results in this text, the LIDT may probably be further enhanced by depositing the two materials in the same chamber. The film thickness needs higher precision in order to design the spectrum with less error. Though ALD is advantageous in thickness resolution, the precision is lower than BBM controlled IBS when the film thickness reaches 100 nm.

It is rather difficult to set the stress of single layers fixed in the design stage. The stress of Al₂O₃ film, as shown in Fig. 65, varies from 300 to 600 MPa. There are probably several reasons for the stress instability.

For one thing, the stress of the ALD films might be influenced by the precursor residual. The intermolecular potential energy of physisorption is much smaller than of chemisorption, leading to a different intermolecular force. The film stress might be thus affected by the not strictly saturated precursor adsorption and desorption.

For another, different thickness might also induce different stress, according to references [172][173]. In this experiment, the stress has a decreasing trend as film thickness increases from 30 to 150 nm, as in Fig. 65. It might be induced by the attenuation in the transfer of intermolecular force as the film thickness increases. However, more experiments are needed to support this inference.

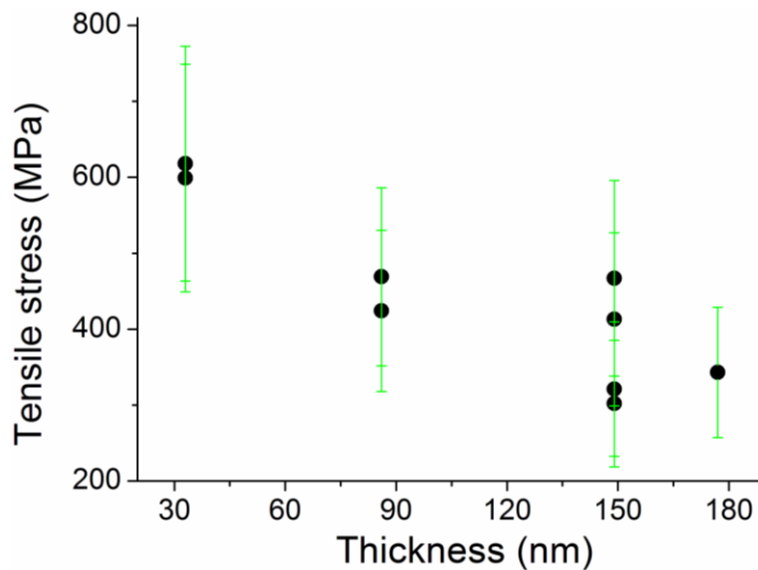


Fig. 65. Stress of ALD Al_2O_3 with different thickness.

Most importantly, the unflat substrate surface contributes largely to the stress error. The measurement of stress is based on Stoney's equation, as the PV expression in equation 27. The stress is determined by the change of peak-valley value ΔPV induced by the coating. This applies well to an ideal flat substrate surface, as in Fig. 66(a). ΔPV approximates the change of curvature. This approximation also works well if the surface is truncated by certain mask to avoid the obvious error. For example, the rim of an IBS film surface is often less coated due to the shielding of the jig, and there is often some film at the rim on the rear surface of an ALD coating, due to the high diffusivity of precursors.

$$\sigma = \left(\frac{E_s}{1-\nu_s} \right) \frac{t_s^2}{6t_f} \left(\frac{1}{R_f} - \frac{1}{R_0} \right) \quad (27)$$

$$\sigma = \frac{4E_s t_s^2 \Delta PV}{3(1-\nu_s) t_f D^2}$$

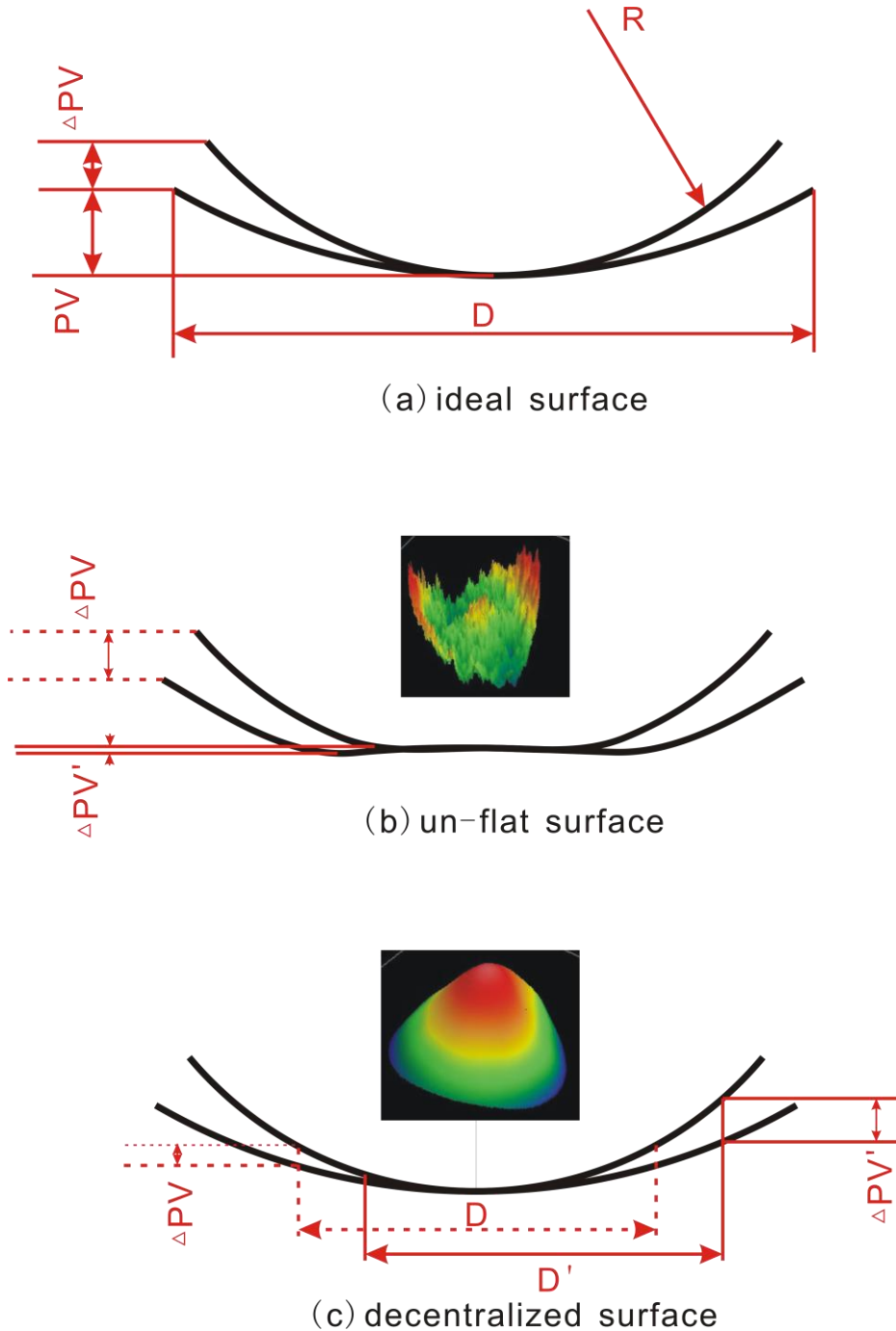


Fig. 66. Influence of un-ideal surface on stress measurement.

As to an imperfect surface, however, extra error might be introduced into the stress value. Take the saddle surface in Fig. 66(b) for an example, due to the miss of

concave apex, the measured PV difference is $\Delta PV - \Delta PV'$, leading to an underestimated stress. On the other hand, If the apex is not at the sample center, as in Fig. 66(c), the measured PV difference becomes larger than the actual ΔPV , resulting in an overestimated stress value. The decentralized apex would also result in different stress value if the surface is tailored by a mask.

In summary, the measured stress has a large error, making it challenging in eliminating the residual stress completely with this compensating method. To further compensate the residual stress, the stress of single layers needs to be measured with higher precision. The error might be diminished by the use of larger flat substrates. Besides, the relationship of stress and film thickness needs to be investigated in more detail.

8.7 Conclusion

Both ALD and IBS can deposit coatings with high density, few structural defects and rather high LIDT. However, their stress problems inhibit their application in large aperture high power lasers. Their stress levels originate probably from the molecule kinetics during deposition. A model based on the intermolecular potential is proposed, concluding that IBS coatings have compressive stress and EBE/ALD coatings have tensile stress.

In this study, an anti-reflection coating based on ALD Al_2O_3 and IBS SiO_2 is designed and fabricated. The resulting spectrum matches the design well, and residual stress is much less than that of single layers. The LIDT of the anti-reflection coating at 532 nm is less than both single layers, probably due to the introduction of additional defects. However, it indicates the promising development of low stress high LIDT coatings for future high power lasers.

9. Other applications

9.1 Nanolaminates

9.1.1 Introduction of nanolaminates

The ultra-fast laser applications impose high demands on optical coatings in terms of film thickness, refractive index and LIDT. The LIDT in subpicosecond pulse regime is found linearly scaling with band gap energy [136]. In general only a limited amount of materials are available in nature. In order to achieve further progresses, novel design techniques are required to adjust the optical band gap values and refractive indices of optical materials. According to the RISED (Refractive Index Stepped Down) concept, a new class of composite materials was made available to optimize the LIDT of high reflection mirrors by co-sputtering two materials in ratio [174][175]. As an alternative to the co-deposited layers with homogeneously distributed atoms, nanolaminates can be considered for a study of the electronic properties of mixed material phases.

The concept of nanolaminates was used in reference [176], in which the structural sizes of the nano layers were not chosen small enough to generate new electronic states in the structure. In the work of Willemsen, IBS Ta_2O_5 or HfO_2 was embedded in a matrix SiO_2 layers to form nanolaminates [177]-[179]. The band gap energy was controlled by the thickness of the quantum well through the electron confinement between the barriers. The smallest thickness of the quantum well was 0.5 nm, which approaches the limit of the IBS coating monitored by BBM.

In this context, ALD is applied to deposit nanolaminates, which has film thickness resolution 0.11 nm. The refractive indices and band gap energies are studied.

9.1.2 Experimental results

Four different HfO_2 and Al_2O_3 stacks $(\text{LH})^n\text{L}$ were manufactured by varying the layer thickness of the HfO_2 (low gap material) down to 0.21 nm and keeping the thickness of the Al_2O_3 barriers as well as the total design thickness of HfO_2 constant. The sample information and properties are listed in Table 17.

The transmission and reflection spectra of each nanolaminate were measured. Sellmeier equations are applied to calculate the equivalent refractive index. As shown

in Fig. 67, a growing trend of refractive index can be observed as the thickness of HfO₂ layer increases.

Table 17. Properties of the manufactured nanolaminates.

Layer thickness HfO ₂ (nm)	Layer thickness Al ₂ O ₃ (nm)	Design	Tauc Band gap (eV)	Refractive index (1064 nm)
8.5	5.5	(LH) ³ L	5.65	1.87
2.1	5.5	(LH) ¹² L	6.00	1.74
0.5	5.5	(LH) ⁴⁸ L	6.13	1.66
0.2	5.5	(LH) ¹²⁰ L	6.25	1.64

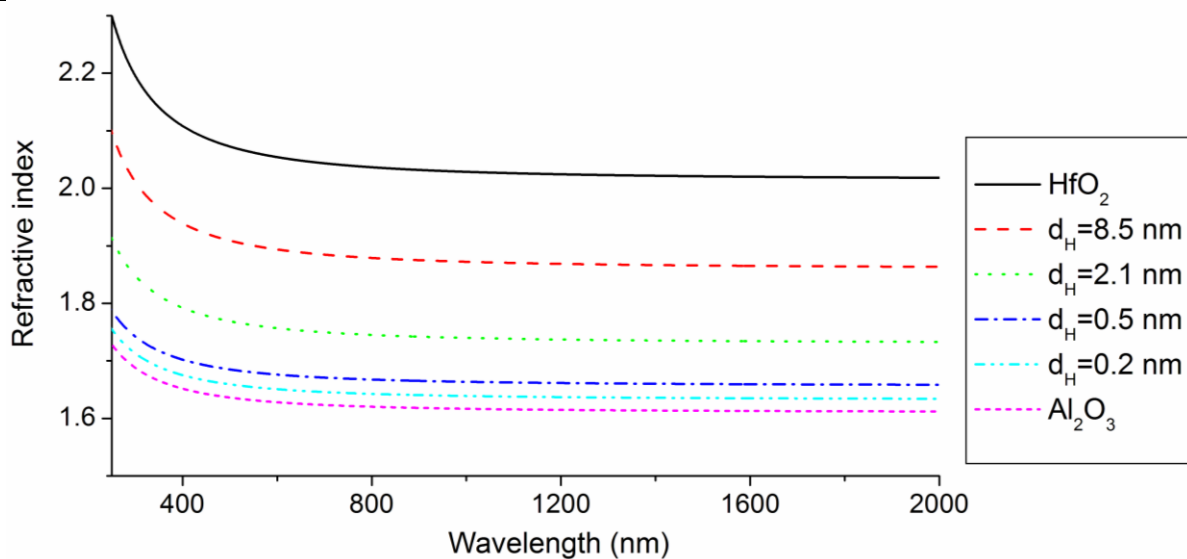


Fig. 67. Equivalent dispersion of the nanolaminates.

A clear blue shift in the band gap is obvious for the manufactured nanolaminates as the thickness of HfO₂ layer decreases, as shown in Fig. 68. One nanolaminate with HfO₂ layer thickness 8.5 nm was prepared for TEM inspection (Fig. 69). The thickness determined by TEM of HfO₂ was about 8.5 nm. However, the thickness of the Al₂O₃ layer adjacent to the substrate is about 4.9 nm while that amid the HfO₂ layers is about 4 nm, showing a thickness error larger than 4%. It might be caused by the different initiation of ALD Al₂O₃ on Si/SiO₂ surface and HfO₂ surface, which was not detectable by spectral measurements such as ellipsometry.

This experiment reveals the promising application of ALD films in nanolaminates, which might gain application in complex coating, or in RISED high power coatings.

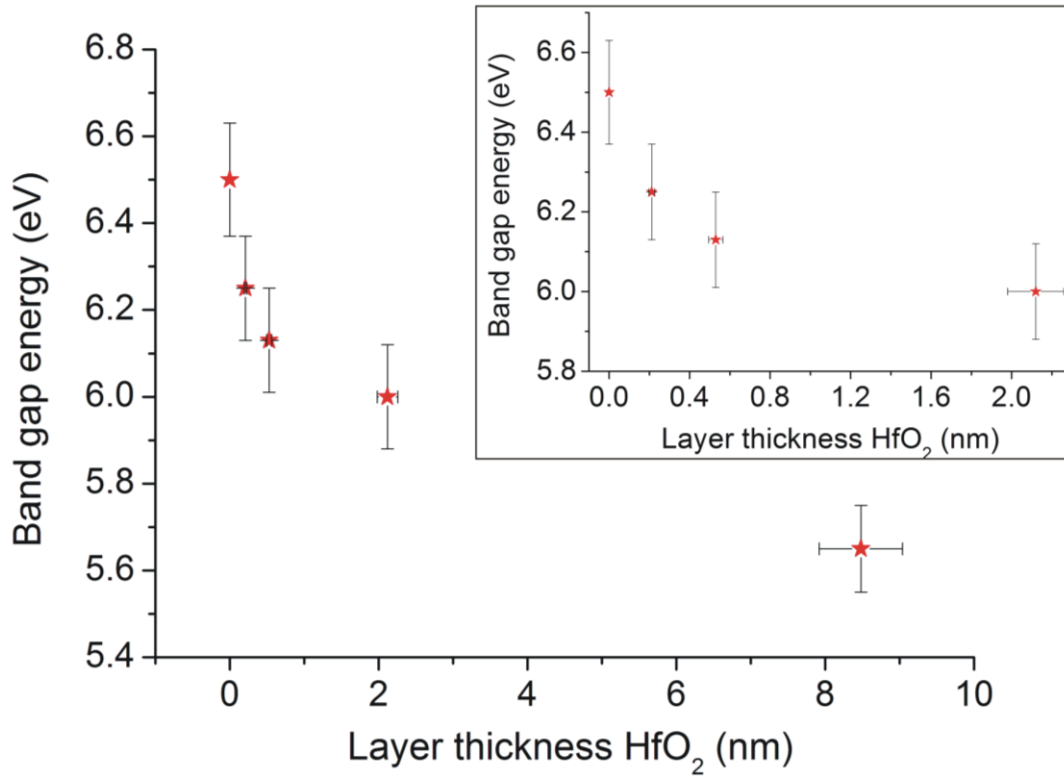


Fig. 68. Band gap energies determined by Tauc plot.

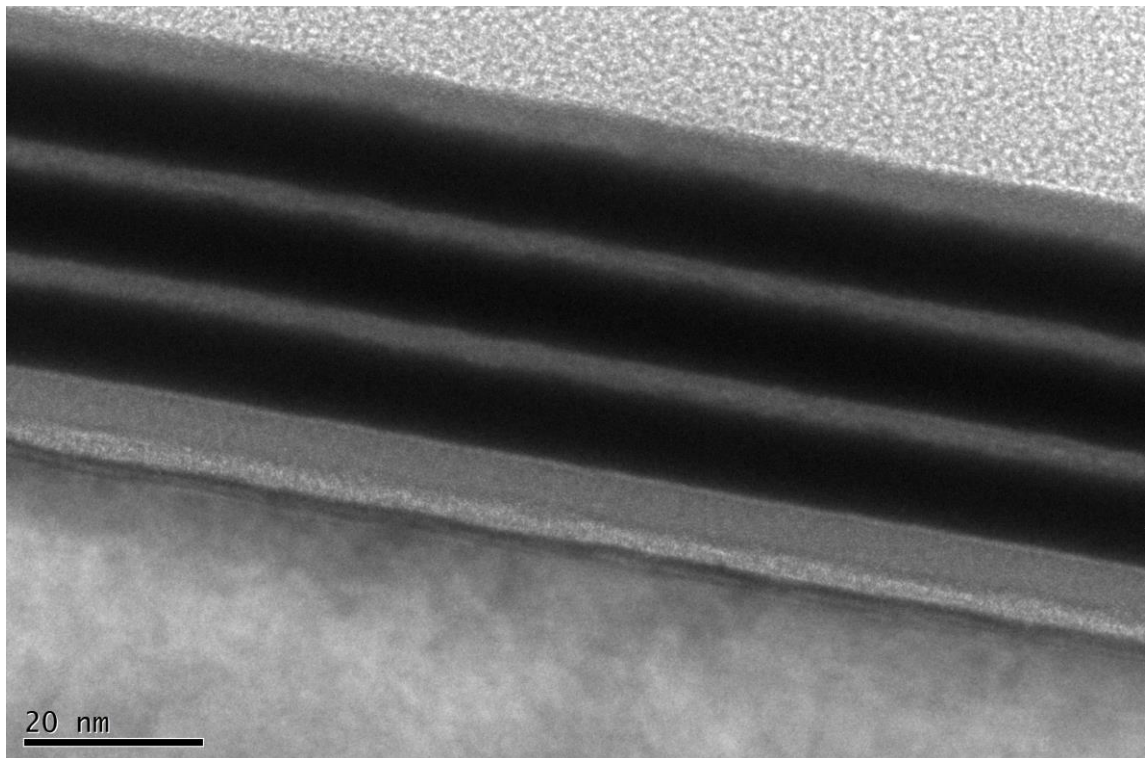


Fig. 69. TEM cross-section of (LH)³L nanolaminate showing the alternating layer structure of HfO₂ (dark area) and Al₂O₃ (bright area).

9.2 GDD film

9.2.1 Introduction

The rapid development of ultra-fast laser applications requires a precise phase management to counter the natural dispersion of light [180][181]. Chirped mirrors offer the possibility to gain HR mirrors with minus Group Delay Dispersion (GDD) around the reference wavelength [179]. Chirped mirrors provide a more compact solution to control the dispersion in comparison to prism pairs [182].

In the current design, the last layer has a thickness of several nanometers, which is difficult to be controlled with QCM or BBM monitor. What's more important, it is the thickness of the last layer that influences the GDD significantly. The thickness error of 1 nm would cause distinctive GDD deviation, but almost no transmittance difference. It is therefore of great importance to realize the last layer with more precise thickness.

Before the invention of phase BBM, which monitors the online GDD directly, ALD was a promising method to solve the thin layer problem of chirped mirror. ALD coating has thickness resolution as high as 0.1 nm. The thickness was controlled by counting cycles instead of in-situ monitoring. Besides that, ALD Al_2O_3 has large band gap, low absorption and high LIDT. This experiment was to deposit ALD Al_2O_3 as last layer of the chirped mirror, minimizing the GDD error.

9.2.2 Experiment

The complete design is composed of 58 layers, the last of which is 10.9 nm Al_2O_3 . The first 57 layers were accomplished by IBS. The measured GDD curve of the 57 layers matched the designed very well.

The last Al_2O_3 layer was deposited by ALD in the 1st module. The GPC was measured to be $0.1045 \text{ nm} \pm 4\%$. The required 10.9 nm corresponded to 104 cycles.

9.2.3 Results and discussion

The reference sample (Si substrate) indicated that the thickness of ALD Al_2O_3 layer was 11.34 nm, which was 0.44 nm thicker than expected. Such small deviation was supposed to cause GDD difference not larger than 20 fs^2 .

The measured result and the calculated GDDs with different last layer thickness are shown in Fig. 70. According to the measurement, the sample ended with ALD Al_2O_3 has a GDD deviation of about 70 fs^2 (including about 20 fs^2 average shift), much more than the prediction of design. In comparison, the phase BBM controlled

sample has a GDD deviation less than 10 fs^2 (excluding the average shift), and the BBM controlled sample has about 200 fs^2 deviation. The measured GDD indicates the thickness of the last layer is about 16 nm , much larger than 11.34 nm of the reference sample.

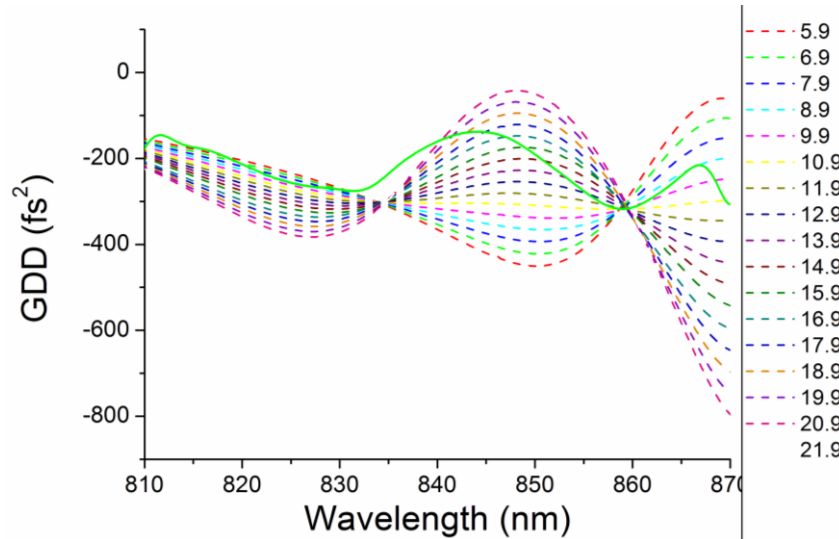


Fig. 70. Measured GDD and the calculation by varying last layer thickness.

There are probably two explanations for these results:

- ◆ The ALD growth on Ta_2O_5 and Si (SiO_2) substrate was different;
- ◆ The heating during ALD changed the GDD of the first 57 layers.

(1) Growth difference on Ta_2O_5 and Si(SiO_2) substrates

The first 57 layers in this experiment were ended with Ta_2O_5 , thus only Ta_2O_5 is discussed here.

An experiment was carried out depositing ALD Al_2O_3 on IBS Ta_2O_5 single layer. The GPC was determined to be 0.1045 nm/cycle by measuring the film on Si substrate. After 1000 cycles deposition, the measured and calculated spectra match well with little error, as shown in Fig. 71. For comparison, the spectra calculated with error $\pm 4\%$ are displayed. The result indicates that the GPC of ALD Al_2O_3 on Ta_2O_5 was almost the same as that on Si substrates.

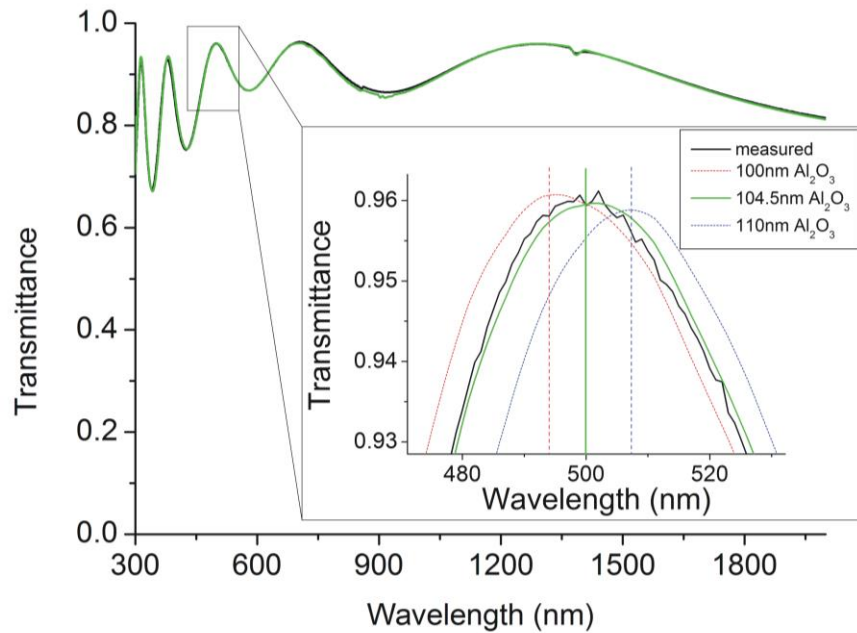


Fig. 71. Measured and calculated spectra of IBS Ta_2O_5 + ALD Al_2O_3 .

(2) Influence of heating or storage on the first 57 layers.

Another GDD coating sample ended with ALD Al_2O_3 was heated in ALD chamber for 20 minutes after 2 weeks storage. As shown in Fig. 72, the heating influences distinctively the GDD of the first 57 layers. This is probably the reason of the failure of experiment – the influence of ALD heating was not considered in the coating design.

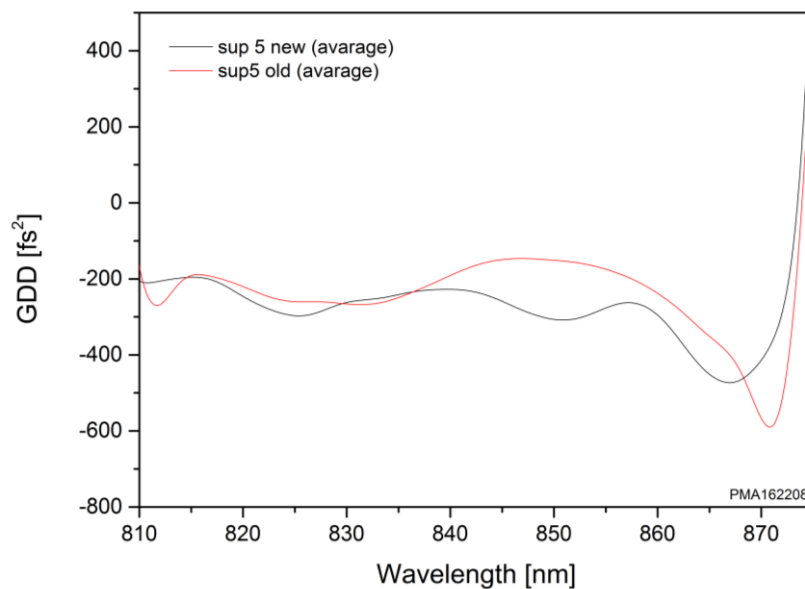


Fig. 72. GDD before and after heating at 200 °C, 20 min.

The solutions would thus be:

- ◆ To study ALD film at room temperature;

- ♦ Or to study the influence of heating on GDD.

It seems impractical to deposit ALD Al_2O_3 at room temperature, since the gas pipes are heated, and the heat would be transferred to the substrate holder. The substrate temperature would reach 78 °C eventually after the film deposition.

9.3 Conclusion

ALD is advantageous in film thickness resolution, therefore it can deposit coatings about 10 nm with little error. Nanolaminates with tailored refractive index have been prepared with ALD HfO_2 and Al_2O_3 . A clear blue shift in band gap energy is detected as the HfO_2 thickness decreased from 8 nm to 0.2 nm. The nanolaminates have promising application in promoting LIDT of femtosecond components following the RISED concept.

ALD Al_2O_3 was used as the last layer of the chirped mirror in this text. However, the GDD does not match the design due to probably the influence of heating the first 57 layers. This experiment points out the development of ALD in future: ALD at room temperature, and ALD with in-situ monitoring.

10. Summary and Conclusions

As potential candidates for laser coatings, ALD Al_2O_3 and HfO_2 have been studied in this thesis in aspects of thickness precision, uniformity, stress, weak absorption, laser induced damage threshold, film density and so on.

ALD is based on the sequential chemi-sorption of reactive precursor molecules onto the substrate. Each precursor has its own vapor pressure, molecule mass and physi-sorption energy. Therefore the exposure time and purging time of each precursor has to be determined separately. It is sensible to estimate the relative ratio of the parameters and instruct the trial experiments to find out the proper process for each precursor.

The self-terminating feature is derived from the limited reactive sites in each ALD cycle. Due to the self-terminating and large surface diffusion rate, the ALD films have good uniformity and thickness with high resolution. Both ALD Al_2O_3 and HfO_2 have stable growth rates, with GPC about $0.11 \text{ nm} \pm 8\%$. Both ALD films have uniformity $>99\%$ without compensating baffle in $\phi 60 \text{ mm}$ area.

The characteristics of ALD Al_2O_3 and HfO_2 concerned in high power components are compared to those of IBS Al_2O_3 and HfO_2 single layer films. The ALD films have comparable refractive indices, band gap energies and LIDT with IBS films. ALD films have lower extinction coefficients than IBS films. The 1064 nm Laser Calorimetry measurements show smaller absorption of ALD films than IBS films. Both ALD films have severe tensile stress, in contrast to the compressive stress of IBS films.

The annealing of ALD films at $300 \text{ }^\circ\text{C}$, $400 \text{ }^\circ\text{C}$ and $500 \text{ }^\circ\text{C}$ has been studied. The annealing at $300 \text{ }^\circ\text{C}$ does not affect the stress or band gap energy distinctively, but enhances the LIDT of ALD Al_2O_3 by nearly 30%. However, the LIDT of ALD HfO_2 is not improved at this temperature. The effect of $400 \text{ }^\circ\text{C}$ annealing is the same with $300 \text{ }^\circ\text{C}$. The $500 \text{ }^\circ\text{C}$ annealing is detrimental to the ALD films, both increasing the absorption and decreasing the LIDT distinctively.

Anti-reflection coatings for different harmonics of Nd: YAG laser were deposited with ALD and IBS $\text{Al}_2\text{O}_3/\text{HfO}_2$, respectively. The film thickness was well controlled by counting the cycle number. The ALD anti-reflection coatings have tensile stress while the IBS coatings have compressive stress. ALD coatings have generally higher LIDTs than IBS coatings for the harmonics of the Nd: YAG laser. The LIDT is mainly

restricted by the ALD HfO_2 layer. The damages of both ALD and IBS anti-reflection coatings are induced by defects.

ALD coating have high density, and have potential applications as capping films. A conventionally evaporated $\text{Ta}_2\text{O}_5/\text{SiO}_2$ coating stack was covered by an ALD Al_2O_3 layer, to isolate the grain pores in the columnar structure from atmospheric moisture. Results indicate good performance of the ALD Al_2O_3 capping layer against the vacuum-air-shift. The spectrum of an ALD anti-reflection coating was measured at different temperature, revealing no thermal shift of the ALD films.

The severe tensile stress of ALD film makes it not suitable for thick components alone. The opposite stress of ALD and IBS coatings are probably contributed by the different molecule velocity. A novel concept was proposed to deposit stress-compensated, high LIDT coatings by using IBS SiO_2 and ALD Al_2O_3 as low and high refractive index materials. An anti-reflection coating was prepared following this concept. The measured spectrum matches the design very well. The anti-reflection coating has much smaller stress than either IBS or ALD single layer films. However, extra defects were introduced as the sample was shifted between the IBS and ALD chamber. The anti-reflection coating has therefore lower LIDT than both single layer films. This concept of combining ALD and IBS coatings has potential in future for development of low stress high LIDT components provided the extra defects could be inhibited.

List of figures

Fig. 1. Plane wavefront incident on a single surface.....	7
Fig. 2. Schematic of an ALD cycle. (1) exposure of precursor; (2) purging; (3) exposure of reactant; (4) purging.	12
Fig. 3. (a) Schematic of ALD system; (b) Schematic of gas flow during one ALD cycle. The pressure was kept constant in the chamber. (c) Valve systems for H ₂ O and TEMAH.....	22
Fig. 4. Measuring the same sample with Ellipsometry.....	23
Fig. 5. The trace of precursor molecules.	25
Fig. 6. Partial pressure during vaporization of different precursors.....	27
Fig. 7. The potential on the substrate surface.....	28
Fig. 8. Schematic of the surface coverage in an ALD exposure step. (a) physisorption and chemisorption; (b) actual adsorption.	29
Fig. 9. Vapor pressure of the precursors. (a) TMA; (b) TEMAH; (c) H ₂ O.....	30
Fig. 10. GPC of an ALD Al ₂ O ₃ cycle plotted versus pulse durations. (a) TMA exposure; (b) TMA purging; (c) H ₂ O exposure; (d) H ₂ O purging.....	31
Fig. 11. GPC of an ALD HfO ₂ cycle plotted versus pulse durations. (a) TEMAH exposure; (b) TEMAH purging; (c) H ₂ O exposure; (d) H ₂ O purging.	31
Fig. 12. Exposure time for saturate adsorption of TEMAH at chamber pressure 110 Pa and 20 Pa.	32
Fig. 13. Impact of substrate temperature on ALD Al ₂ O ₃ . 400 cycles were deposited. (a) Transmittance; (b) GPC; (c) Refractive index.	33
Fig. 14. The typical pollution caused by decomposition of TEMAH. The polluted area is about 3×4mm ²	35
Fig. 15. ALD Al ₂ O ₃ thickness plotted versus cycle number. (a) deposited in 1 st module; (b) deposited in 2 nd module.	37
Fig. 16. Uniformity of Al ₂ O ₃ films deposited with different parameters.....	38
Fig. 17. Elemental composition characterized by EDX.	39
Fig. 18. Dispersion comparison of ALD Al ₂ O ₃ and IBS Al ₂ O ₃ film. (a) Refractive index; (b) Extinction coefficient.	39
Fig. 19. Tauc plot of ALD Al ₂ O ₃ and extrapolation toward the abscissa.	40
Fig. 20. (a) Surface profile of ALD Al ₂ O ₃ film (104nm);.....	40

Fig. 21. Absorption comparison of ALD and IBS Al ₂ O ₃	41
Fig. 22. Damage probability plots. (a)-(d) ALD Al ₂ O ₃ ; (e)-(h) IBS Al ₂ O ₃	42
Fig. 23. Characteristic damage curves of fused silica substrate, ALD Al ₂ O ₃ and IBS Al ₂ O ₃ . (a) 50% LIDT; (b) 0% LIDT.....	43
Fig. 24. Damage morphologies of ALD and IBS Al ₂ O ₃ film layer.	44
Fig. 25. Thickness of different cycles of ALD HfO ₂ layers. (a) pulse durations 5/5/0.2/30s; (b) pulse durations 7/60/0.5/60s.	45
Fig. 26. Uniformity of ALD HfO ₂ film.	46
Fig. 27. Elemental composition of ALD HfO ₂ characterized by EDX.	46
Fig. 28. Dispersion comparison of ALD HfO ₂ and IBS HfO ₂ film. (a) Refractive index; (b) Extinction coefficient.	47
Fig. 29. Tauc plot of ALD HfO ₂ and extrapolation toward the abscissa.	47
Fig. 30. Surface profiles. (a) ALD HfO ₂ film (125nm); (b) IBS HfO ₂ film (133 nm).....	48
Fig. 31. Damage probability plots. (a)-(d) ALD HfO ₂ ; (e)-(h) IBS HfO ₂	49
Fig. 32. Characteristic curves of ALD HfO ₂ and IBS HfO ₂	50
Fig. 33. Damage morphologies of ALD and IBS HfO ₂ film layer.	51
Fig. 34. Dispersion of the annealed ALD films. (a) Refractive indices of annealed ALD Al ₂ O ₃ ; (b) Extinction coefficients of annealed ALD Al ₂ O ₃ ; (c) Refractive indices of annealed ALD HfO ₂ ; (d) Extinction coefficients of annealed ALD HfO ₂	52
Fig. 35. Stress of the annealed ALD films.....	52
Fig. 36. Tauc plots of the 300 °C annealed films. (a) ALD Al ₂ O ₃ ; (b) ALD HfO ₂	53
Fig. 37. Damage probabilities of ALD Al ₂ O ₃ annealed at different temperature. (a)-(b): not annealed; (c)-(d): 300 °C annealed; (e)-(f): 400 °C annealed; (g)-(h): 500 °C annealed.	54
Fig. 38. Damage probabilities of ALD HfO ₂ annealed at different temperatures. (a)-(b): not annealed; (c)-(d): 300 °C annealed; (e)-(f): 400 °C annealed; (g)-(h): 500°C annealed.	55
Fig. 39. Characteristic damage curves of ALD single layer films annealed at different temperature.....	56
Fig. 40. Dispersion of different film materials.....	57
Fig. 41. Extinction coefficient of different film materials.	57
Fig. 42. Characteristic damage curves of different film materials (1ω).	58
Fig. 43. Peeling off of the thick ALD films (5μm).....	59

Fig. 44. Transmittance of ALD and IBS anti-reflection coatings.....	62
Fig. 45. Stress of the anti-reflection coatings.....	63
Fig. 46. 10 pulse damage probabilities of ALD and IBS Anti-reflection coatings at different harmonics of Nd:YAG laser.....	64
Fig. 47. Characteristic damage curves of ALD and IBS anti-reflection coatings.....	65
Fig. 48. Damage morphologies of ALD and IBS anti-reflection coatings at different harmonics of Nd: YAG laser.....	66
Fig. 49. LIDT plot with irradiating photon energy. (a) ALD anti-reflection coating; (b) IBS anti-reflection coating.	67
Fig. 50. Model of intra-band defects.	67
Fig. 51. Spectra of samples. (a) M1 (without capping layer) measured in atmosphere and vacuum; (b) M3 (with capping layer) measured in atmosphere and vacuum; (c) M3 (with capping layer) measured in atmosphere before and after dipping in water.	71
Fig. 52. Vacuum-air-shift of DWHR protected by ALD Al_2O_3 of different thickness. (a) The spectra measured in air and vacuum; (b) The Vacuum-air-shift plot versus capping layer thickness.....	72
Fig. 53. Temperature shift test of the ALD $\text{HfO}_2/\text{Al}_2\text{O}_3$ anti-reflection coating....	72
Fig. 54. Film structure of EBE multilayer capped by ALD Al_2O_3 layer. (a) overview; (b) pores of EBE multilayers.....	73
Fig. 55. Schematic diagram showing molecule in different adsorption sites and the corresponding potential energy E as a function of relative distance z to the surface molecule. (a) Ta_2O_5 or SiO_2 molecule in EBE; (b) TMA or H_2O molecule in ALD.	74
Fig. 56. Intermolecular force induced stress. (a) attractive force leading to tensile stress; (b) repulsive force leading to compressive stress.....	78
Fig. 57. Intermolecular potential. The bottom part could be approximated as harmonic oscillator potential.	79
Fig. 58. (a) The trace of an impinging molecule with different initial velocities; (b) The mean position of an impinging molecule with different initial velocities.	81
Fig. 59. Algorithm for designing a stress-compensated coating.	83
Fig. 60. The measured and designed spectra.	84
Fig. 61. Surface profile of the single layers and anti-reflection coating.....	85

Fig. 62. Damage probabilities. (a)-(b) IBS SiO ₂ , 135 nm; (c)-(d) ALD Al ₂ O ₃ , 178 nm; (e)-(f) compensated anti-reflection coating.....	87
Fig. 63. Characteristic damage of the anti-reflection coatings as well as the single layers.	88
Fig. 64. Damage morphologies of the single layers and the stress compensated anti-reflection coating.	89
Fig. 65. Stress of ALD Al ₂ O ₃ with different thickness.....	90
Fig. 66. Influence of un-ideal surface on stress measurement.	91
Fig. 67. Equivalent dispersion of the nanolaminates.	94
Fig. 68. Band gap energies determined by Tauc plot.	95
Fig. 69. TEM cross-section of (LH) ³ L nanolaminate showing the alternating layer structure of HfO ₂ (dark area) and Al ₂ O ₃ (bright area).	95
Fig. 70. Measured GDD and the calculation by varying last layer thickness.....	97
Fig. 71. Measured and calculated spectra of IBS Ta ₂ O ₅ + ALD Al ₂ O ₃	98
Fig. 72. GDD before and after heating at 200 °C, 20 min.	98
Fig. 73. The damped harmonic oscillator with initial conditions.	125
Fig. 74. Solution of the damped harmonic oscillator. The initial velocity plays a key role in the trace of the oscillator.	125
Fig. 75. Mean position of the damped harmonic oscillator.....	127

List of tables

Table 1. Requirements on optical coatings of modern applications.....	2
Table 2. Assessment of optical coating techniques.	9
Table 3. Part of ALD materials for optics.	16
Table 4. Valve recipes for an ALD HfO ₂ cycle.	21
Table 5. Physical properties of TMA, TEMAH and H ₂ O.....	26
Table 6. Desorption rate in case of physi-sorption and chemi-sorption.	27
Table 7. The inferred physi-sorption energy.	34
Table 8. The parameters for this ALD experiment.	36
Table 9. Absorption of ALD Al ₂ O ₃ and HfO ₂ after annealing.....	53
Table 10. Band gap energies (reference [136]) and extinction coefficients (at 1064 nm) of different film materials.	58
Table 11. Characterization of ALD Al ₂ O ₃ and HfO ₂ compared to IBS single layers. .	60
Table 12. Absorption of the anti-reflection coatings.....	63
Table 13. Summary of the properties of ALD and IBS AR for different harmonics of Nd: YAG laser.	68
Table 14. Estimation of the $2r_0\zeta\omega_0$ of Al ₂ O ₃ and SiO ₂	81
Table 15. Stress induced by molecule velocity in different coating process.	82
Table 16. Stress comparison of single layers and anti-reflection coating.	86
Table 17. Properties of the manufactured nanolaminates.	94

Reference

- [1] H. A. Macleod, "Thin-film optical filters," fourth edition, CRC Press, Taylor & Francis Group 2010.
- [2] R. P. Riegert, "Optimum usage of quartz crystal monitor based devices" in IVth International Vacuum Congress Manchester Institute of Physics and the Physical Society: 527-530 (1968).
- [3] D. Ristau, H. Ehlers, T. Groß, and M. Lappschies, "Optical broadband monitoring of conventional and ion processes," Appl. Opt. 45: 1495-1501 (2006).
- [4] M. Lappschies, T. Groß, H. Ehlers, D. Ristau, "Broadband optical monitoring for the deposition of complex coatings," Proc. SPIE 5250: 637-645 (2004).
- [5] L. Holland and W. Steckelmacher, "The distribution of thin films condensed on surfaces by the vacuum evaporation method," Vacuum 2: 346-364 (1952).
- [6] J. V. Ramsay, R. P. Netterfield and E. G. V. Mugridge, "Large-area uniform evaporated thin films," Vacuum 24: 337-340 (1976).
- [7] K. U. Schreiber and J. R. Wells, "Invited review article: large ring lasers for rotation sensing," Review of Scientific Instruments 84: 041101 (2013).
- [8] B. C. Barish and R. Weiß, "LIGO and the detection of gravitational waves," Physics Today 52(10): 44-50 (1999).
- [9] B. A. Paldus, B. G. Fidric, S. S. Sanders, S. M. Tan, H. Pham, A. A. Kachanov, E. H. Wahl and E. R. Croßon, "High-sensitivity detectors based on cavity ring-down spectroscopy," Proc. SPIE 5617: 312-322 (2004).
- [10] M. H. Schleier-Smith, I. D. Leroux and V. Vuletic, "Preparation of reduced-quantum-uncertainty input states for an atomic clock," Proc. SPIE 7431: 743107 (2009).
- [11] www.trumpf.com
- [12] www.en.raycuslaser.com
- [13] www.ipgphotonics.com
- [14] B. Camille, P. J. Wegner and R. Hauley-Fedder, "UV sources: world's largest laser to generate powerful ultraviolet beams," Laser focus world, 2008.
- [15] D. Ristau, "Laser induced damage in optical materials," CRC Press (2015).
- [16] D. Ristau, M. Jupe and K. Starke, "Laser damage thresholds of optical coatings," Thin Solid Films 518: 1607-1613 (2009).

- [17] T. W. Walker, A. H. Günther and P. Nielsen, "Pulsed laser-induced damage to thin-film optical coatings- Part I: Experimental & Part II: Theory," *IEEE J. Quant. Electron.* QE-17: 2041-2065 (1981).
- [18] L. Gallais, B. Mangote, M. Zerrad, M. Commandre, A. Meininkaitis, J. Mirauskas, M. Jeskevcs and V. Sirutkaitis, "Laser-induced damage of hafnia coatings as a function of pulse duration in the femtosecond to nanosecond range," *Appl. Opt.* 50: C178-C187 (2011).
- [19] N. Blömborgen, "Laser-induced electric breakdown in solids," *IEEE J. Quant. Electron.* 10: 375-386 (1974).
- [20] J. K. Lawson, et al, "NIF optical specifications – The importance of the RMS gradient specification," *Proc. SPIE* 3492: 336-343 (1998).
- [21] D. M. Aikens, "The origin and evolution of the optics specifications for the national ignition facility," *SPIE* 2536: 2-12 (1995).
- [22] A. E. Ennos, "Stresses developed in optical film coatings," *Appl. Opt.* 5(1): 51-61 (1966).
- [23] European Space Agency, ADM-Aeolus Science Report. ESA SP-1311, 121 (2008).
- [24] I. Petrov, P. B. Barna, L. Hultman, and J. E. Greene, "Microstructural evolution during film growth," *J. Vac. Sci. Technol. A* 21(5): S117-S128 (2003).
- [25] C. J. Stolz, J. R. Taylor, W. K. Eickelberg, and J. D. Lindh, "Effects of vacuum exposure on stress and spectral shift of high reflective coatings," *Appl. Opt.*, 32 (28): 5666-5672 (1993).
- [26] L. Jensen, M. Jupe, H. Mädebach, H. Ehlers, K. Starke, D. Ristau, W. Riede, P. Allenspacher, and H. Schröder, "Damage threshold investigations of high power laser optics under atmospheric and vacuum conditions," *Proc. SPIE* 6403: 1-10 (2007).
- [27] J. H. Campbell, R. A. Hawley-Fedder, C. J. Stolz, J. A. Menapace, M. R. Borden, P. K. Whitman, J. Yu, M. Runkel, M. O. Riley, M. D. Feit and R. P. Hackel, "NIF optical materials and fabrication technologies: An overview," *Proc. SPIE* 5341: 84-95 (2004).
- [28] C. J. Stolz, C. L. Weinzapfel, A. L. Rigatti, J. B. Oliver, J. Taniguchi, R. P. Bevis and J. S. Rajasansi, "Fabrication of meter-scale laser resistant mirrors for the National Ignition Facility, a fusion laser," *Proc. SPIE* 5193: 50-58 (2003).

- [29] K. H. Günther, "Microstructure of vapor-deposited optical coatings," *Appl. Opt.* 23(21): 3806 (1984).
- [30] K. H. Müller, "Monte Carlo calculation for structural modifications in ion assisted thin film deposition due to thermal spikes," *Journal of Vacuum Science and Technology, A* 4: 184-188 (1986).
- [31] K. H. Müller, "Models for microstructure evolution during optical thin film growth," *Proceedings of the Society of Photo-Optical Instrumentation Engineers* 821: 36-44 (1988).
- [32] M. Turowski, M. Jupe, H. Ehlers, T. Melzig, A. Pflug and D. Ristau, "Simulation in thin film technology," *Proc. SPIE* 9627: 962707 (2015).
- [33] J. D. Targove and H. A. Macleod, "Verification of momentum transfer as the dominant densifying mechanism in ion-assisted deposition," *Appl. Opt.* 27: 3779-3781 (1988).
- [34] P. J. Martin, H. A. Macleod, R. P. Netterfield, C. G. Pacey and W. G. Sainty, "Ion beam assisted deposition of thin films," *Appl. Opt.* 22: 178-184 (1983).
- [35] M. A. Scobey, R. I. Seddon, J. W. Seeser, R. R. Austin, P. M. LeFebvre and B. W. Manley, Optical Coating Laboratory, Inc "Magnetron sputtering apparatus and process", US Patent 4,851,095 [1989].
- [36] D. Ristau and T. Groß, "Ion beam sputter coatings for laser technology," *Proc. SPIE* 5963: 13(2010).
- [37] T. W. Jolly and R. Lalezari, "Ion beam sputter deposition techniques for the production of optical coatings of the highest quality," *Proc. SPIE* 1892: 250-254 (1992).
- [38] J. M. Mackowski, L. Pinard, L. Dognin, P. Ganau, B. Lagrange, C. Michel and M. Morgue, "Different approaches to improve the wavefront of low-loss mirrors used in the VIRGO gravitational wave antenna," in *Optical Interference Coatings*: 18-20 (1998).
- [39] R. A. Negres, C. J. Stolz, M. D. Thomas and M. Caputo, "355-nm, nanosecond laser mirror thin film damage competition," *Proc. SPIE* 10447: 104470X (2017).
- [40] M. Lappschies, T. Groß, H. Ehlers and D. Ristau, "Broadband optical monitoring for the deposition of complex coating designs," *Proc. SPIE* 5250: 637-645 (2004).
- [41] I. M. Thomas, "Sol-gel coatings for high power laser optics – past, present and future," *SPIE* 2114: 232-242 (1994).

- [42] C. J. Brinker, G. C. Frye, A. J. Hurd and C. S. Ashley, "Fundamentals of sol-gel dip coating," *Thin solid films* 201: 97-108 (1991).
- [43] C. J. Stolz, J. Adams, M. D. Shirk, M. A. Norton and T. L. Weiland, "Engineering meter-scale laser resistant coatings for the near IR," in *Advances in Optical Thin Films II*, C. Amra, N. Kaiser, and H. A. Macleod, eds., *Proc. SPIE* 5963: 59630Y-1-8 (2005).
- [44] P. M. Pegon, C. V. Germain, Y. R. Rorato, P. F. Belleville and E. Lavastre, "Large area Sol-Gel optical coatings for the Megajoule Laser prototype," *Proc. SPIE* 5250: 170-181 (2004).
- [45] B. Tian, X. Wang, Y. Niu, J. Zhang, Q. Zhang, Z. Zhang, G. Wu, B. Zhou and J. Shen, "Preparation and stress evolution of sol-gel SiO₂ antireflective coatings for small size anisotropic lithium triborate crystals," *AIP Advances* 6: 045208 (2016).
- [46] H. A. McInnes, J. E. Andrew, N. J. Bazin, A. J. Morris and K. J. Porter, "Effects of layer thickness and number of interfaces on the damage threshold of ultra violet sol gel mirrors," *SPIE* 3578: 128-135 (1998).
- [47] L. Martinu, O. Zabeida and J. E. Klemberg-Sapieha, "Plasma-enhanced chemical vapor deposition of functional coatings," *Handbook of Deposition Technologies for Films and Coatings* (third Edition), edited by: Peter M. Martin (2010).
- [48] S. Guenther, M. Fahland, J. Fahlteich, B. Meyer, S. Straach and N. Schiller, "High rate low pressure PECVD for barrier and optical coatings," *Thin Solid Films* 532: 44-49 (2013).
- [49] J. D. Ferguson, A. W. Weimer and S. M. George, "Atomic layer deposition of Al₂O₃ films on Polyethylene particles," *Chem. Mater.* 16: 5602-5609 (2004).
- [50] W. Tsai, R. J. Carter, H. Nohira, M. Caymax, T. Conard, V. Cosnier, S. DeGendt, M. Heyns, J. Petry, O. Richard, W. Vandervorst, E. Young, C. Zhao, J. Maes, M. Tuominen, W. H. Schuller, E. Garfunkel and T. Gustafsson, "Surface preparation and interfacial stability of high-k dielectrics deposited by atomic layer chemical vapor deposition," *Microelectronic Engineering* 65: 259-272 (2003).
- [51] Y. Widjaja and C. B. Musgrave, "Quantum chemical study of the mechanism of aluminum oxide atomic layer deposition," *Applied Physics Letters* 80(18): 3304-3306 (2002).

- [52] W. Chen, Q. Sun, M. Xu, S. Ding, D. W. Zhang and L. Wang, "Atomic layer deposition of hafnium oxide from Tetrakis(ethylmethylamino)hafnium and water precursors," *J. Phys. Chem. C* 111: 6495-6499 (2007).
- [53] T. Suntola and J. Hyvärinen, "Atomic layer epitaxy," *Ann. Rev. Mater. Sci.* 15: 177-195 (1985).
- [54] T. Suntola and J. Antson, "Method for producing compound thin films," United States Patent 4058430 (1977).
- [55] R. L. Puurunen, "A short history of atomic layer deposition: Tuomo Suntola's atomic layer epitaxy," *Chem. Vap. Deposition* 20: 332-344 (2014).
- [56] J. Nishizawa and H. Abe, "molecular layer Epitaxy," *J. Electrochem. Soc.* 132: 1197-1200 (1985).
- [57] T. Suntola, "Atomic layer epitaxy," *Thin Solid Films* 216: 84-89 (1992).
- [58] M. Ritala, "Advanced ALE process of amorphous and polycrystalline films," *Applied Surface Science* 112: 223 (1997).
- [59] M. Ritala, K. Kukli, A. Rahtu, P. I. Raisenen, M. Leskela, T. Sajavaara and J. Keinonen, "Atomic layer deposition of oxide thin films with metal alkoxides as oxygen sources," *Science* 288: 319 (2000).
- [60] M. Ritala, K. Kukli, A. Rahtu, P. I. Raisenen, M. Leskelä, T. Sajavaara and J. Keinonen, "Atomic layer deposition of oxide thin films with metal alkoxides as oxygen sources," *Science* 288: 319-321 (2000).
- [61] D. G. Park, H. J. Cho, K. Y. Lim and C. Lim, "Characteristics of n+ Polycrystalline-Si/Al₂O₃/Si metal-oxide-semiconductor structures prepared by atomic layer chemical vapor deposition using Al(CH₃)₃ and H₂O vapor," *J. Appl. Phys.* 89: 6275-6280 (2001).
- [62] W. S. Yang, Y. K. Kim, S. Y. Yang, J. H. Choi, H. S. Park, S. I. Lee and J. B. Yoo, "Effect of SiO₂ intermediate layer on Al₂O₃ SiO₂ n-poly Si interface deposited using atomic layer deposition (ALD) for deep submicron device applications," *Surface and Coatings Technology* 131: 79-83 (2000).
- [63] Y. Kim, S. M. Lee, C. S. Park, S. I. Lee and M. Y. Lee, "Substrate dependence on the optical properties of Al₂O₃ films grown by atomic layer deposition," *Appl. Phys. Lett* 71(25): 3604-3606 (1997).
- [64] P. Ericsson, S. Bengtsson and J. Skarp, "Properties of Al₂O₃ films deposited on silicon by atomic layer epitaxy," *Microelectronic Engineering* 36: 91-94 (1997).

- [65] C. M. Perkins, B. B. Triplett, P. C. McIntyre, K. C. Saraswat, S. Haukka and M. Tuominen, "Electrical and materials properties of ZrO_2 gate dielectrics grown by atomic layer chemical vapor deposition," *Applied Physics Letters* 78 (16): 2357-2359 (2001).
- [66] K. Kukli, J. Ihanus, M. Ritala and M. Leskela, "Tailoring the dielectric properties of HfO_2 - Ta_2O_5 nanolaminates," *Appl. Phys. Lett.* 68(26): 3737-3739 (1996).
- [67] P. Rouffignac, J. S. Park and R. G. Gordon, "Atomic layer deposition of Y_2O_3 thin films from Yttrium Tris(N,N'-diisopropylacetamidinate) and water," *Chem. Mater.* 17: 4808-4814 (2005).
- [68] R. G. Gordon, J. Becker, D. Hausmann and S. Suh, "Vapor deposition of metal oxides and silicates: possible gate insulators for future microelectronics," *Chem. Mater.* 13: 2463-3464 (2001).
- [69] H. Zhang, R. Solanki, B. Roberds, G. Bai and I. Banerjee, "High permittivity thin film nanolaminates," *Journal of Applied Physics* 87(4): 1921-1924 (2000).
- [70] H. Zhang and R. Solanki, "Atomic layer deposition of high dielectric constant nanolaminates," *Journal of the Electrochemical Society* 148(4): F63-F66 (2001).
- [71] K. Kukli, M. Ritala and M. Leskelä, "Properties of atomic layer deposited $(Ta_{1-x}Nb_x)_2O_5$ solid solution films and Ta_2O_5 - Nb_2O_5 nanolaminates," *Journal of Applied Physics* 86(10): 5656-5662 (1999).
- [72] K. Kukli, M. Ritala and M. Leskelä, "Properties of $(Nb_{1-x}Ta_x)_2O_5$ solid solutions and $(Nb_{1-x}Ta_x)_2O_5$ - ZrO_2 nanolaminates grown by atomic layer epitaxy," *Nanostructured Materials* 8(7): 785-793 (1997).
- [73] H. Kattelus, M. Ylilammi, J. Saarilahti, J. Antson and S. Lindfors, "Layered tantalum-aluminum oxide films deposited by atomic layer epitaxy," *Thin Solid Films* 225: 296-298 (1993).
- [74] J. Aarik, A. Aidla, A. A. Kiisler, T. Uustare and V. Sammelselg, "Effect of crystal structure on optical properties of TiO_2 films grown by atomic layer deposition," *Thin Solid Films* 305: 270-273 (1997).
- [75] J. Aarik, A. Aidla, H. Mändar and T. Uustare, "Atomic layer deposition of titanium dioxide from $TiCl_4$ and H_2O : investigation of growth mechanism," *Applied Surface Science* 172: 148-158 (2001).

- [76] J. Aarik, A. Aidla, V. Sammelselg and T. Uustare, "Effect of growth conditions on formation of TiO₂-II thin films in atomic layer deposition process," *Journal of Crystal Growth* 181: 259-264 (1997).
- [77] J. Aarik, A. Aidla, T. Uustare and V. Sammelselg, "Morphology and structure of TiO₂ thin films grown by atomic layer deposition," *Journal of Crystal Growth* 148: 268-275 (1995).
- [78] A. Suisalu, J. Aarik, H. Mändar and I. Sildos, "Spectroscopic study of nanocrystalline TiO₂ thin films grown by atomic layer deposition," *Thin Solid Films* 336: 295-298 (1998).
- [79] A. Tarre, A. Rosental, V. Sammelselg and T. Uustare, "Comparative study of low-temperature chloride atomic-layer chemical vapor deposition of TiO₂ and SnO₂," *Applied Surface Science* 175-176: 111-116 (2001).
- [80] K. Kukli, A. Aidla, J. Aarik, M. Schuisky, A. Harsta, M. Ritala and M. Leskelä, "Real-time monitoring in atomic layer deposition of TiO₂ from TiI₄ and H₂O-H₂O₂," *Langmuir* 16: 8122-8128 (2000).
- [81] A. Rahtu, K. Kukli and M. Ritala, "In situ mass spectrometry study on atomic layer deposition from metal (Ti, Ta and Nb) ethoxides and water," *Chem. Mater.* 13: 817-823 (2001).
- [82] B. D. Piercy, C. Z. Leng and M. D. Losego, "Variation in the density, optical polarizabilities, and crystallinity of TiO₂ thin films deposited via atomic layer deposition from 38 to 150 °C using the titanium tetrachloride-water reaction," *J. Vac. Sci. Technol. A* 35(3): 03E107 (2017).
- [83] K. Kukli, M. Ritala, M. Leskelä and R. Lappalainen, "Niobium oxide thin films grown by atomic layer epitaxy," *Chem. Vap. Deposition* 4(1): 29-34 (1998).
- [84] M. Ritala and M. Leskelä, "Zirconium dioxide thin films deposited by ALE using zirconium tetrachloride as precursor," *Applied Surface Science* 75: 333-340 (1994).
- [85] K. Kukli, M. Ritala and M. Leskelä, "Low-temperature deposition of zirconium oxide-based nanocrystalline films by alternate supply of Zr[OC(CH₃)₃]₄ and H₂O," *Chem. Vap. Deposition* 6(6): 297-302 (2000).
- [86] K. Kukli, K. Forsgren, J. Aarik, T. Uustare, A. Aidla, A. Niskanen, M. Ritala, M. Leskelä and A. Harsta, "Atomic layer deposition of zirconium oxide from

- zirconium tetraiodide, water and hydrogen peroxide,” *Journal of Crystal Growth* 231: 262-272 (2001).
- [87] D. Riihelä, M. Ritala, Raija Matero and M. Leskelä, “Introducing atomic layer epitaxy for the deposition of optical thin films,” *Thin Solid Films* 289: 250-255 (1996).
- [88] K. Kukli, J. Aarik, A. Aidla, O. Kohan, T. Uustare and V. Sammelselg, “Properties of tantalum oxide thin films grown by atomic layer deposition,” *Thin Solid Films* 260: 135-142 (1995).
- [89] J. W. Klaus, A. W. Ott, A. C. Dillon and S. M. George, “Atomic layer controlled growth of Si_3N_4 films using sequential surface reactions,” *Surface Science* 418: L14-L19 (1998).
- [90] M. Ritala, M. Leskelä, L. Niinistö, T. Prohaska, G. Friedbacher and M. Grasserbauer, “Development of crystallinity and morphology in hafnium dioxide thin films grown by atomic layer epitaxy,” *Thin Solid Films* 250: 72-80 (1994).
- [91] K. Kukli, M. Ritala, T. Sajavaara, J. Keinonen and M. Leskelä, “Atomic layer deposition of hafnium dioxide films from hafnium tetrakis(ethylmethanamide) and water,” *Chem. Vap. Deposition* 8(5): 199-204 (2002).
- [92] K. Kukli, M. Ritala, M. Leskelä, T. Sajavaara, J. Keinonen, A. C. Jones and J. L. Roberts, “Atomic layer deposition of hafnium dioxide films from 1-methoxy-2-methyl-2-propanolate complex of hafnium,” *Chem. Mater.* 15: 1722-1727 (2003).
- [93] M. Putkonen, M. Nieminen, J. Niinistö and L. Niinistö, “Surface-controlled deposition of Sc_2O_3 thin films by atomic layer epitaxy using β -Diketonate and organometallic precursors,” *Chem. Mater.* 13: 4701-4707 (2001).
- [94] M. Putkonen, T. Sajavaara, L. S. Johansson and L. Niinistö, “Low-temperature ALE deposition of Y_2O_3 thin films from β -Diketonate precursors,” *Chem. Vap. Deposition* 7(1): 44-50 (2001).
- [95] T. Asikainen, M. Ritala and M. Leskelä, “Growth of Indium-Tin-Oxide thin films by atomic layer epitaxy,” *J. Electrochem. Soc.* 142(10): 3538-3541 (1995).
- [96] M. Ritala, T. Asikainen and M. Leskelä, “Enhanced growth rate in atomic layer epitaxy of Indium Oxide and Indium-Tin Oxide thin films,” *Electrochemical and Solid-state Letters* 1(3): 156-157 (1998).
- [97] K. Kukli, M. Ritala, V. Pore, M. Leskelä, T. Sajavaara, R. I. Hegde, D. C. Gilmer, P. J. Tobin, A. C. Jones and H. C. Aspinall, “Atomic layer deposition and

- properties of Lanthanum oxide and lanthanum-aluminum oxide films,” *Chem. Vap. Deposition* 12: 158-164 (2006).
- [98] R. L. Puurunen, “Surface chemistry of atomic layer deposition: a case study for the trimethylaluminum/water process,” *Journal of Applied Physics* 97: 121301 (2005).
- [99] K. Pfeiffer, S. Shestaeva, A. Bingel, P. Munzert, L. Ghazaryan, C. Helvoirt, W. M. M. Kessels, U. T. Sanli, C. Grevent, G. Schutz, M. Putkonen, I. Buchanan, L. Jensen, D. Ristau, A. Tunnermann and A. Szeghalmi, “Comparative study of ALD SiO₂ thin films for optical applications,” *Optical Materials Express* 6(2): 660-670 (2016).
- [100] L. Han and Z. Chen, “High-quality thin SiO₂ films grown by atomic layer deposition using tris(dimethylamino)silane (TDMAS) and ozone,” *ECS Journal of Solid State Science and Technology* 2(11): N228-N236 (2013).
- [101] B. B. Burton, S. W. Kang, S. W. Rhee and S. M. George, “SiO₂ atomic layer deposition using Tris(dimethylamino)silane and hydrogen peroxide studied by in situ transmission FTIR spectroscopy,” *J. Phys. Chem. C* 113: 8249-8257 (2009).
- [102] T. Pilvi, K. Arstila, M. Leskelä and M. Ritala, “Novel ALD process for depositing CaF₂ thin films,” *Chem. Mater.* 19: 3387-3392 (2007).
- [103] T. Pilvi, T. Hatanpää, E. Puukilainen, K. Arstila, M. Bischoff, U. Kaiser, N. Kaiser, M. Leskelä and M. Ritalaa, “Study of a novel ALD process for depositing MgF₂ thin films,” *J. Mater. Chem.* 17: 5077-5083 (2007).
- [104] T. Pilvi, E. Puukilainen, U. Kreissig, M. Leskelae and M. Ritala, “Atomic layer deposition of MgF₂ thin films using TaF₅ as a novel fluorine source,” *Chem. Mater.* 20: 5023-5028 (2008).
- [105] J. Aarik, A. Aidla, A. A. Kiisler, T. Uustare and V. Sammelselg, “Influence of substrate temperature on atomic layer growth and properties of HfO₂ thin films,” *Thin Solid Films* 340: 110-116 (1999).
- [106] J. Aarik, A. Aidla, H. Mändar, T. Uustare, K. Kukli and M. Schuisky, “Phase transformations in hafnium dioxide thin films grown by atomic layer deposition at high temperatures,” *Applied Surface Science* 173: 15-21 (2001).
- [107] K. Kukli, J. Aarik, A. Aidla, H. Siimon, M. Ritala and M. Leskelä, “In situ study of atomic layer epitaxy growth of tantalum oxide thin films from Ta(OC₂H₅)₅ and H₂O,” *Applied Surface Science* 112: 236-242 (1997).

- [108] K. Kukli, M. Ritala and M. Leskelä, "Atomic layer epitaxy growth of Tantalum oxide thin films from $\text{Ta}(\text{OC}_2\text{H}_5)_5$ and H_2O ," *J. Electrochem. Soc.* 142(5): 1670-1675 (1995).
- [109] J. Aarik, K. Kukli, A. Aidla and L. Pung, "Mechanisms of suboxide growth and etching in atomic layer deposition of tantalum oxide from TaCl_5 and H_2O ," *Applied Surface Science* 103: 331-341 (1996).
- [110] K. Kukli, J. Aarik, A. Aidla, O. Kohan, T. Uustare and V. Sammelselg, "Properties of tantalum oxide thin films grown by atomic layer deposition," *Thin Solid Films* 260: 135-142 (1995).
- [111] A. Szeghalmi, M. Helgert, R. Brunner, F. Heyroth, U. Gösele and M. Knez, "Atomic layer deposition of Al_2O_3 and TiO_2 multilayers for applications as bandpass filters and antireflection coatings," *Appl. Opt.* 48(9): 1727-1732 (2009).
- [112] K. Pfeiffer, U. Schulz, A. Tunnermann and A. Szeghalmi, "Antireflection coatings for strongly curved glass lenses by atomic layer deposition," *Coatings* 7(118): 1-12 (2017).
- [113] Y. Wei, H. Liu, O. Sheng, Z. Liu, S. Chen and L. Yang, "Laser damage properties of $\text{TiO}_2/\text{Al}_2\text{O}_3$ thin films grown by atomic layer deposition," *Appl. Opt.* 50(24): 4720-4727 (2011).
- [114] Y. Li, W. Shen, X. Hao, T. Lang, S. J and X. Liu, "Rugate notch filter fabricated by atomic layer deposition," *Appl. Opt.* 53(4): A270-A275 (2014).
- [115] J. Mouchart, "Thin film optical coatings. 2: Three-layer antireflection coating theory," *Appl. Opt.* 16(10): 2722-2728 (1977).
- [116] L. O. Jensen, H. Mädebach, J. Maula, K. Gürtler and D. Ristau, "Laser induced damage threshold and optical properties of TiO_2 and Al_2O_3 – Coatings prepared by atomic layer deposition," *Proc. SPIE* 8530: 853010 (2012).
- [117] Z. Liu, S. Chen, P. Ma, Y. Wei, Y. Zheng, F. Pan, H. Liu and G. Tang, "Characterization of 1064 nm nanosecond laser induced damage on antireflection coatings grown by atomic layer deposition," *Opt. Express* 20(2): 854-863 (2012).
- [118] Y. Wei, F. Pan, Q. Zhang and P. Ma, "Atomic layer deposition for fabrication of $\text{HfO}_2/\text{Al}_2\text{O}_3$ thin films with high laser-induced damage thresholds," *Nanoscale Research Letters* 10(44): 1-7 (2015).

- [119] E. A. Davis and N. F. Mott, "Conduction in non-crystalline systems V. conductivity, optical absorption and photoconductivity in amorphous semiconductors," *Philosophical Magazine A* 22(179): 903-921 (1970).
- [120] M. Ozvold, V. Bohac, V. Gasparik, G. Leggieri, S. Luby, A. Luches, E. Majkova and P. Mrafko, "The optical band gap of semiconducting iron disilicide thin films," *Thin Solid Films* 263: 92-98 (1995).
- [121] G. G. Stoney, "The tension of metallic films deposited by electrolysis," *Proc. R. Soc. Lond. A* 82: 172-175 (1909).
- [122] G. C. A. M. Janssen, M. M. Abdalla, F. Van Keulen, B. R. Pujada and B. Van Venrooy, "Celebrating the 100th anniversary of the Stoney equation for film stress: developments from polycrystalline steel strips to single crystal silicon wafers," *Thin Solid Films* 517: 1858-1867 (2009).
- [123] ISO 11551: 2003, Optics and optical instruments – Lasers and laser-related equipment – Test method for absorptance of optical laser components.
- [124] U. Willamowski, D. Ristau, and E. Welsch, " Measuring the absolute absorptance of optical laser components," *Appl. Opt.* 37, 8362 (1998).
- [125] ISO 21254: 2011, Lasers and laser-related equipment – Test methods for laser-induced damage threshold.
- [126] K. Kukli, M. Ritala, T. Sajavaara, J. Keinonen and M. Leskelae, "Atomic layer deposition of hafnium dioxide films from hafnium tetrakis (ethylmethanamide) and water," *Chem. Vap. Deposition* 8(5): 199 (2002).
- [127] D. M. Hausmann, E. Kim, J. Becker and R. G. Gordon, "Atomic layer deposition of hafnium and zirconium oxides using metal amide precursors," *Chem. Mater.* 14: 4350-4358 (2002).
- [128] R. G. Gordon, D. Hausmann, E. Kim and J. Shepard, "A kinetic model for step coverage by atomic layer deposition in narrow holes or trenches," *Chem. Vap. Deposition* 9(2): 73-78 (2003).
- [129] X. Liu, S. Ramanathan, A. Longdergan, A. Srivastava, E. Lee, T. E. Seidel, J. T. Barton, D. Pang and R. G. Gordon, "ALD of Hafnium oxide thin films from tetrakis(ethylmethanamino) hafnium and ozone," *Journal of the electrochemical society*, 152(3): G213-G219 (2005).
- [130] T. Kent, K. Tang, V. Chobpattana, M. A. Negara, M. Edmonds, W. Mitchell, B. Sahu, R. Galatage, R. Droopad, P. McIntyre and A. C. Kummel, "The influence of

- surface preparation on low temperature HfO₂ ALD on InGaAs (001) and (110) surfaces,” *The Journal of Chemical Physics* 143: 164711 (2015).
- [131] D. W. McNeill, S. Bhattacharya, H. Wadsworth, F. H. Ruddell, S. J. N. Mitchell, B. M. Armstrong and H. S. Gamble, “Atomic layer deposition of hafnium oxide dielectrics on silicon and germanium substrates,” *J Mater Sci: Mater Electron* 19: 119-123 (2008).
- [132] D. Tantraviwat, Y. H. Low, P. T. Baine, S. J. N. Mitchell, D. W. McNeill, B. M. Armstrong and H. S. Gamble, “Electrical characterization of ALD Al₂O₃ and HfO₂ films on Germanium,” *ECS Transitions* 28(1): 201-207 (2010).
- [133] Y. W. Kim, Y. Roh, Ji-Beom Yoo and Hyongsu Kim, “Characteristics of atomic layer deposition grown HfO₂ films after exposure to plasma treatments,” *Thin solid films* 515: 2984-2989 (2007).
- [134] N. K. Oh, J. T. Kim, J. K. Ahn, G. Kang, S. Y. Kim and J. Y. Yun, “The effects of thermal decomposition of tetrakis-ethylmethylaminohafnium (TEMAHf) precursors on HfO₂ film growth using atomic layer deposition,” *Appl. Sci. Converg. Technol.* 25(3): 56-60 (2016).
- [135] R. F. Berg, “Apparatus to measure the vapor pressure of slowly decomposing compounds from 1 Pa to 10⁵ Pa,” *J. Chem. Eng. Data* 60: 3483-3495 (2015).
- [136] M. Mero, J. Liu, W. Rudolph, D. Ristau and K. Starke, “Scaling laws of femtosecond laser pulse induced breakdown in oxide films,” *Physical Review B* 71, 115109 (2005).
- [137] Oxford Instruments plc, “Ion beam deposition of Al₂O₃,” www.oxfordplasma.de/process/ibsal2o3.htm (2005).
- [138] L. Jensen, M. Mende, H. Blaschke, D. Ristau, D. Nguyen, L. Emmert and W. Rudolph, “Investigations on SiO₂/HfO₂ mixtures for nanosecond and femtosecond pulses,” *Proc. SPIE* 7842: 748207 (2010).
- [139] A. P. Ghosh, L. J. Gerenser, C. M. Jarman and J. E. Fornalik, “Thin-film encapsulation of organic light-emitting devices,” *Applied Physics Letters* 86: 223503 (2005).
- [140] P. F. Carcia, R. S. McLean and M. H. Reilly, “Permeation measurements and modeling of highly defective Al₂O₃ thin films grown by atomic layer deposition on polymers,” *Applied Physics Letters* 97: 221901 (2010).

- [141] P. F. Carcia, R. S. McLean, M. H. Reilly, M. D. Groner and S. M. George, "Ca test of Al₂O₃ gas diffusion barriers grown by atomic layer deposition on polymers," *Applied Physics Letters* 89: 031915 (2006).
- [142] E. Langereis, M. Creatore, S. B. S. Heil, M. C. M. van de Sanden and W. M. M. Kessels, "Plasma-assisted atomic layer deposition of Al₂O₃ moisture permeation barriers on polymers," *Applied Physics Letters* 89: 081915 (2006).
- [143] M. D. Groner, S. M. George, R. S. McLean and P. F. Carcia, "Gas diffusion barriers on polymers using Al₂O₃ atomic layer deposition," *Applied Physics Letters* 88: 051907 (2006).
- [144] P. F. Carcia, R. S. McLean, M. D. Groner, A. A. Dameron and S. M. George, "Gas diffusion ultrabarriers on polymer substrates using Al₂O₃ atomic layer deposition and SiN plasma-enhanced chemical vapor deposition," *Journal of Applied Physics* 106: 023533 (2009).
- [145] S. Ferrari, F. Perissinotti, E. Peron, L. Fumagalli, D. Natali and M. Sampietro, "Atomic layer deposited Al₂O₃ as a capping layer for polymer based transistors," *Organic Electronics* 8: 407-414 (2007).
- [146] J. Schmidt, A. Merkle, R. Brendel, B. Hoex, M. C. M. van de Sanden and W. M. M. Kessels, "Surface passivation of high-efficiency silicon solar cells by atomic-layer-deposited Al₂O₃," *Prog. Photovolt: Res. Appl.* 16: 461-466 (2008).
- [147] W. J. Potscavage, S. Yoo, B. Domercq and B. Kippelen, "Encapsulation of pentacene/C₆₀ organic solar cells with Al₂O₃ deposited by atomic layer deposition," *Applied Physics Letters* 90: 253511 (2007).
- [148] P. Johansson, K. Lahtinen, J. Kuusipalo, T. Kääriäinen, P. Maydannik and D. Cameron, "Atomic layer deposition process for barrier applications of flexible packaging," in: *Tappi 2010 PLACE Conference, TAPPI, 2010*.
- [149] S. S. Kim, N. T. Gabriel, W. B. Song and J. J. Talghader, "Encapsulation of low-refractive-index SiO₂ nanorods by Al₂O₃ with atomic layer deposition," *Optics Express* 15 (24): 16285-16291 (2007).
- [150] D. Ristau, H. Ehlers, T. Gross and M. Lappschies, "Optical broadband monitoring of conventional and ion processes," *Appl. Opt.* 45(7): 1495-1501 (2006).
- [151] K. Oura, V. G. Lifshits, A. A. Saranin, A. V. Zotov and M. Katayama, "Surface Science: An introduction," Springer-Verlag Berlin Heidelberg (2003).

- [152] www.materion.com/resource-center/product-data-and-related-literature/inorganic-chemicals/oxides/aluminum-oxide-al2o3-for-opticalcoating.
- [153] J. K. Hirvonen, "Ion beam assisted thin film deposition," *Materials Science Reports* 6(6): 215-274 (1991).
- [154] C. J. Stolz, "The National Ignition Facility: the world's largest optical system," *Proc. SPIE* 6834: 683402 (2007).
- [155] N. W. Hopps, T. H. Bett, N. Cann, C. N. Danson, S. J. Duffield, D. A. Egan, S. P. Elsmere, M. T. Girling, E. J. Harvey, D. I. Hillier, D. J. Hoarty, P. M. R. Jinks, M. J. Norman, S. J. F. Parker, P. A. Treadwell and D. N. Winter, "Overview of project Orion," *Proc. SPIE* 7916: 79160C (2011).
- [156] C. J. Stolz, "Status of NIF mirror technologies for completion of the NIF facility," *Proc. SPIE* 7101: 710115 (2008).
- [157] R. Zacharias, E. Bliss, S. Winters, R. Sacks, M. Feldman, A. Grey, J. Koch, C. Stolz, J. Toepfen, L. V. Atta and B. Woods, "Wavefront control of high power laser beams in the National Ignition Facility (NIF)," *Proc. SPIE* 3889: 332-343 (2000).
- [158] D. M. Aikens, "The origin and evolution of the optics specifications for the National Ignition Facility," *SPIE* 2536: 2-12 (1995).
- [159] S. Padin, "Spatial spectrum analysis of wave front correction with a segmented mirror," *Appl. Opt.* 42(19): 3721-3725 (2003).
- [160] J. H. Campbell, R. A. Hawley-Fedder, C. J. Stolz, J. A. Menapace, M. R. Borden, P. K. Whitman, J. Yu, M. Runkel, M. O. Riley, M. D. Feit and R. P. Hackel, "NIF optical materials and fabrication technologies: an overview," *Proc. SPIE* 5341: 84-101 (2004).
- [161] D. Ristau, X. C. Dang and J. Ebert, "Interface and bulk absorption of oxide layers and correlation to damage threshold at 1.064 μm ," *NBS Spec. Publ.* 727: 298-312 (1984).
- [162] C. J. Stolz, L. M. Sheehan, S. M. Maricle, S. Schwartz, M. R. Kozlowski and R. T. Jennings, "Laser conditioning methods of hafnia silica multilayer mirrors," *Proc. SPIE* 3264: 105-111 (1998).
- [163] D. Ristau and T. Gross, "Ion beam sputter coatings for laser technology," *Proc. SPIE* 5963: 596313 (2005).

- [164] R. A. Negres, C. J. Stolz, M. D. Thomas and M. Caputo, "355-nm, nanosecond laser mirror thin film damage competition," Proc. SPIE 10447: 104470X (2017).
- [165] M. Bischoff, T. Nowitzki, O. Voss, S. Wilbrandt and O. Stenzel, "Postdeposition treatment of IBS coatings for UV applications with optimized thin film stress properties," Appl. Opt. 53(4): A212-A220 (2014).
- [166] Y. Pu, Z. Qiao, G. Wang, F. Qiu, P. Ma and S. Wang, "Stress reduction and structural properties of Ta₂O₅/SiO₂ mixture films produced by ion-beam sputtering," Proc. SPIE 9683: 968323 (2016).
- [167] V. P. Filippova, S. A. Kunavin and M. S. Pugachev, "Calculation of the parameters of the Lennard Jones potential for pairs of identical atoms based on the properties of solid substances," Inorganic Materials 6(1): 1-4 (2015).
- [168] O. L. Nelson and D. E. Anderson, "Potential barrier parameters in thin film Al-Al₂O₃-Metal diodes," Journal of Applied Physics 37(1): 77-82 (1966).
- [169] J. Solyom, "Fundamentals of the physics of solids: Volume 1: Structure and Dynamics," Springer Berlin Heidelberg (2007).
- [170] M. Finnis, "Interatomic forces in condensed matter," Oxford University Press (2003).
- [171] S. Kirkpatrick, C. D. Gelatt and M. P. Vecchi, "Optimization by simulated annealing," Science 220(4598): 671-680 (1983).
- [172] A. E. Ennos, "Stresses developed in optical film coatings," Appl. Opt. 5 (1): 51-61 (1966).
- [173] G. N. Strauss, "Mechanical stress in optical coatings," Optical Interference Coatings: 207-209 (2003).
- [174] M. Jupe, M. Lappschies, L. Jensen, K. Starke, D. Ristau, A. Melninkaitis and W. Rudolph, "Mixed oxide coatings for advanced fs-laser applications," Proc. SPIE 6720: 67200U (2007).
- [175] L. Jensen and D. Ristau, "Coatings of Oxide Composites," Proc. SPIE 8530: 853013 (2012).
- [176] O. Stenzel, S. Wilbrandt, M. Schuermann, N. Kaiser, H. Ehlers, M. Mende, D. Ristau, S. Bruns, M. Vergoehl, M. Stolze, M. Held, H. Niederwald, T. Koch, W. Riggers, P. Burdack, G. Mark, R. Schaefer, S. Mewes, M. Bischoff, M. Arntzen, F. Eisenkraemer, M. Lappschies, S. Jakobs, S. Koch and B. Baumgarten, "Tailored

- Nanocomposite Coatings for Optics,” in Optical Interference Coatings, OSA Technical Digest (Optical Society of America, 2010), Paper MD2.
- [177] T. Willemsen, P. Geerke, M. Jupe, L. Gallais and D. Ristau, “Electronic quantization in dielectric nanolaminats,” Proc. SPIE 10014: 100140C (2016).
- [178] T. Willemsen, M. Jupe, L. Gallais, D. Tetzlaff and D. Ristau, “Tunable optical properties of amorphous Tantalum layers in a quantizing structure,” Opt. Letters. 42(21): 4502-4505 (2017).
- [179] T. Willemsen, M. Jupe, M. Gyamfi, S. Schlichting and D. Ristau, “Enhancement of the damage resistance of ultra-fast optics by novel design approaches,” Opt. Express. 25(25): 31948-31959 (2017).
- [180] M. Hentschel, R. Kienberger, Ch. Spielmann, G. A. Reider, N. Milosevic, T. Brabec, P. Corkum, U. Heinzmann, M. Drescher, and F. Krausz, “Attosecond metrology,” Nature 414 (6863): 509-513 (2001).
- [181] E. Goulielmakis, V. S. Yakovlev, A. L. Cavalieri, M. Uiberacker, V. Pervak, A. Apolonski, R. Kienberger, U. Kleineberg, and F. Krausz, “Attosecond control and measurement: lightwave electronics,” Science 317 (5839): 769-775 (2007).
- [182] R. L. Fork, O. E. Martinez, and J. P. Gordon, “Negative dispersion using pairs of prisms,” Optics Letters 9(5): 150-152 (1984).

List of original publications

- [1] H. Liu, L. Jensen, H. Mädebach, P. Ma and D. Ristau, "Comparison of ALD and IBS $\text{HfO}_2/\text{Al}_2\text{O}_3$ anti-reflection coatings for the harmonics of the Nd: YAG laser," Proc. SPIE 10691: 106911B (2018).
- [2] H. Liu, L. Jensen, P. Ma and D. Ristau, "ALD anti-reflection coatings at 1ω , 2ω , 3ω and 4ω for high-power ns-laser application," Adv. Opt. Techn. 2018: 1-9 (2018).
- [3] H. Liu, L. Jensen, J. Becker, M. C. Wurz, P. Ma and D. Ristau, "Comparison of ALD and IBS Al_2O_3 films for high power lasers," Proc. SPIE 10014: 1001421 (2016).
- [4] Y. Willer, H. Liu, I. Balasa and D. Ristau, "Calibration accuracy of laser calorimetry for common crystal geometries," Proc. SPIE 10447: 104471V (2017).

Appendix I – Damped harmonic oscillator

1. Solution of damped harmonic oscillator

A simple harmonic oscillator consists of a mass m , which experiences a single force F . The force pulls the mass in the direction of the point $r=0$ and depends only on the mass's position and a constant k . Balance of forces for the system is:

$$F = ma = m \frac{d^2 r}{dt^2} = -kr \quad (28)$$

The solution is described by:

$$r(t) = A \cdot \cos(\omega_0 t + \phi) \quad (29)$$

Where $\omega_0 = \sqrt{k/m}$ is the angular frequency of oscillation, the phase ϕ determines the starting point on the sine wave, A is determined by the initial condition.

A damped harmonic oscillator is slowed down by friction, or damping. Due to the friction force, the velocity decreases in proportion to the acting frictional force. The frictional force F_f can be modeled as being proportional to the velocity v of the object: $F_f = -c_d v$, where c_d is called the viscous damping coefficient. Balance of forces for damped harmonic oscillators is then:

$$F = ma = m \frac{d^2 r}{dt^2} = -kr - c_d \frac{dr}{dt} \quad (30)$$

This equation can be rewritten into the form:

$$\frac{d^2 r}{dt^2} + 2\zeta\omega_0 \frac{dr}{dt} + \omega_0^2 r = 0 \quad (31)$$

Where $\omega_0 = \sqrt{k/m}$ is the undamped angular frequency of the oscillator, and $\zeta = c_d / 2\sqrt{mk}$ is the damping ratio. The solution is described by:

$$r(t) = A \cdot e^{-\zeta\omega_0 t} \cdot \sin\left(\sqrt{1-\zeta^2}\omega_0 t + \phi\right) \quad (32)$$

Where Φ and A are determined by the initial condition mentioned in chapter 8:

$$\begin{aligned} r|_{t=0} &= r_0 \\ \frac{dr}{dt}|_{t=0} &= v_0 \end{aligned} \quad (33)$$

The potential as well as the initial conditions are illustrated in Fig. 73. The solution is:

$$r(t) = \frac{v_0 + r_0 \zeta \omega_0}{\omega_0 \sqrt{1 - \zeta^2}} e^{-\zeta \omega_0 t} \sin(\sqrt{1 - \zeta^2} \omega_0 t) + r_0 e^{-\zeta \omega_0 t} \cos(\sqrt{1 - \zeta^2} \omega_0 t) \quad (34)$$

The traces of the oscillator with different initial velocities are illustrated in Fig. 74.

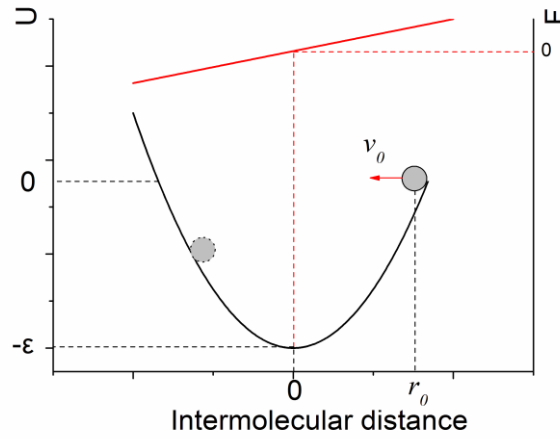


Fig. 73. The damped harmonic oscillator with initial conditions.

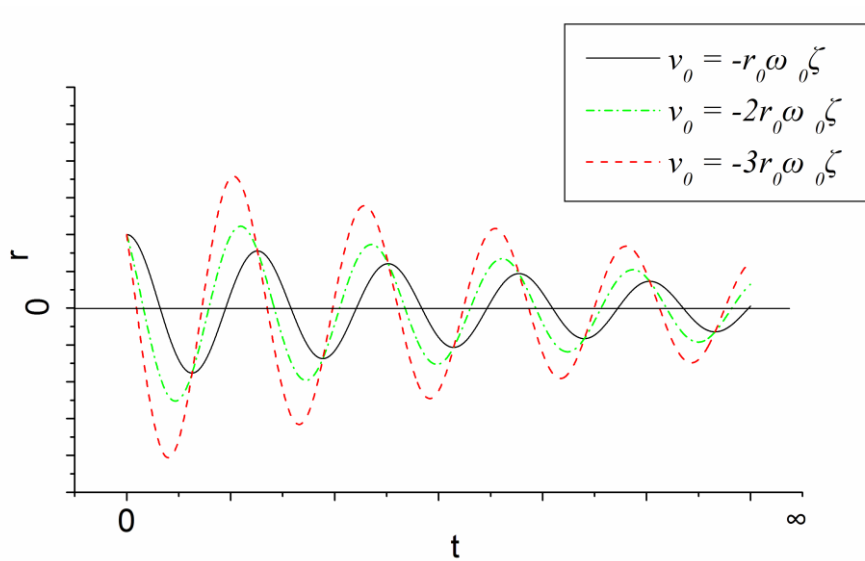


Fig. 74. Solution of the damped harmonic oscillator. The initial velocity plays a key role in the trace of the oscillator.

There are several features about the oscillation:

- ♦ The initial velocity v_0 plays a key role in determining the amplitude of the second peak. The larger the initial velocity v_0 , the larger amplitude the molecule oscillates.
- ♦ The oscillating amplitude damps from the second peak, and reaches eventually zero.

2. Mean position of the oscillator

It is more sensible to consider the mean position of the oscillator during damping rather than the transient position. The mean position after time t could be expressed as:

$$\langle r(t) \rangle = \frac{1}{t} \int_0^t r(t) dt \quad (35)$$

In which the two important integrals are:

$$\begin{aligned} \int_0^t e^{-\zeta\omega_0 t} \sin(\sqrt{1-\zeta^2}\omega_0 t) dt &= \frac{1}{\omega_0} \left[\sqrt{1-\zeta^2} - \sqrt{1-\zeta^2} \cdot e^{-\zeta\omega_0 t} \cdot \cos(\sqrt{1-\zeta^2}\omega_0 t) - \zeta e^{-\zeta\omega_0 t} \cdot \sin(\sqrt{1-\zeta^2}\omega_0 t) \right] \\ \int_0^t e^{-\zeta\omega_0 t} \cos(\sqrt{1-\zeta^2}\omega_0 t) dt &= \frac{1}{\omega_0} \left[\zeta + \sqrt{1-\zeta^2} \cdot e^{-\zeta\omega_0 t} \cdot \sin(\sqrt{1-\zeta^2}\omega_0 t) - \zeta e^{-\zeta\omega_0 t} \cdot \cos(\sqrt{1-\zeta^2}\omega_0 t) \right] \end{aligned} \quad (36)$$

The mean position is deployed as:

$$\begin{aligned} \langle r(t) \rangle &= \frac{v_0 + r_0 \zeta \omega_0}{t \cdot \omega_0^2 \sqrt{1-\zeta^2}} \left[\sqrt{1-\zeta^2} - \sqrt{1-\zeta^2} \cdot e^{-\zeta\omega_0 t} \cdot \cos(\sqrt{1-\zeta^2}\omega_0 t) - \zeta \cdot e^{-\zeta\omega_0 t} \cdot \sin(\sqrt{1-\zeta^2}\omega_0 t) \right] \\ &+ \frac{r_0}{t \cdot \omega_0} \left[\zeta + \sqrt{1-\zeta^2} \cdot e^{-\zeta\omega_0 t} \cdot \sin(\sqrt{1-\zeta^2}\omega_0 t) - \zeta \cdot e^{-\zeta\omega_0 t} \cdot \cos(\sqrt{1-\zeta^2}\omega_0 t) \right] \end{aligned} \quad (37)$$

It is reasonable to choose t as integer multiples of the oscillating cycle for intuitive explicitness.

$$\omega_0 t \sqrt{1-\zeta^2} = n_{osc} \cdot 2\pi \quad (38)$$

Equation (37) is therefore:

$$\langle r(t) \rangle = \frac{v_0 + 2r_0 \zeta \omega_0}{t \cdot \omega_0^2} (1 - e^{-\zeta\omega_0 t}) \quad (39)$$

Notice that v_0 is minus as illustrated in Fig. 73. The sign of mean position is dependent on the initial velocity v_0 . If the absolute velocity is small, $|v_0| < 2r_0 \zeta \omega_0$, the mean position is positive, otherwise, the mean position would be negative, as illustrated in Fig. 75.

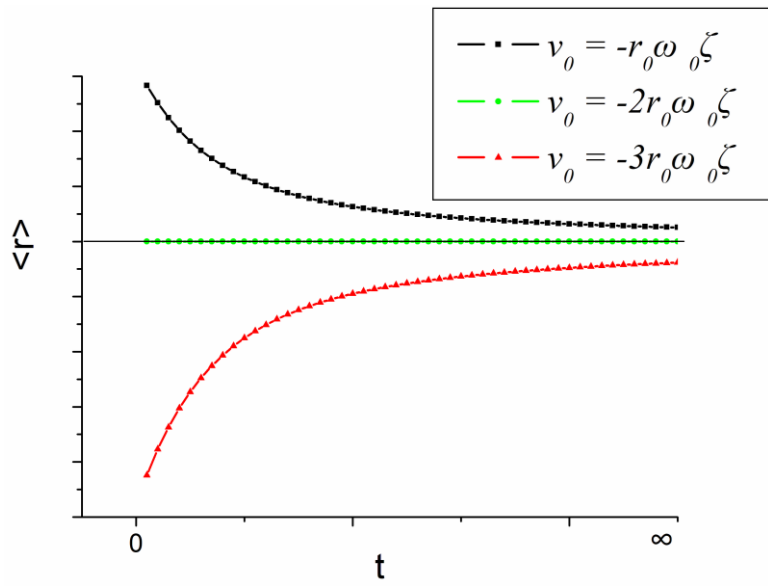


Fig. 75. Mean position of the damped harmonic oscillator.

Declaration

I declare that I have written this dissertation independently. I have specified all the sources and aids used. This dissertation has not previously been used as a thesis or master's thesis.

Hannover, 10.Oct, 2018

Curriculum

Personal information

Name	Hao Liu
Birthday	27. March 1986 in Hubei, China
Marital status	Married – 0 kinder
Nationality:	China

Education

1992-1996	Primary school, Hubei, China
1996-2002	Middle school, Hubei, China
09/2002 – 06/2006	College of Science, Wuhan U. of Tech. Degree: Bachelor of Science
09/2006 – 06/2008	Huazhong U. Sci. & Tech. Degree: Master of Engineering
09/2014 – Present	physics and mathematics, Leibniz U. of Hannover Doctoral Candidate

Industry

2008-2014	Chengdu Fine Optical Engineering and Research Center Optical Coating Engineer
-----------	--

Acknowledgements

The research studies reported in this thesis was carried out during the years 2014-2018 in the Laboratory of Nano and Quantum Engineering in the Leibniz University of Hannover. It has been a period of intense learning for me. I would like to reflect on the people who have supported and helped me so much throughout this period.

Firstly, I owe my deepest gratitude to my supervisor at LZH, Prof. Detlev Ristau. Thank you for your excellent cooperation and for all the opportunities I was given to conduct my research and communicate with experts over the world. Secondly, I would like to thank Prof. Ma Ping in FOERC. You supported me greatly and were always willing to help me. Particularly, I would like to thank my tutor in LZH, Dr. Lars Jensen. Your wealth of knowledge and patient feedback concerning my work are highly appreciated.

I am grateful to my colleagues in PZH, LZH and LNQE for their expertise and fruitful collaboration. Many thanks go to Jürgen Becker for maintaining the ALD equipment and the valuable discussions on the techniques. Many thanks also go to Istvan, Eugen, Mark, Heiner, Marco, Thomas and many colleagues for the valuable help on experiments. I had a great time during these years working with you.

I appreciate my parents and my wife. You are always there for me. I would like to thank my friends for their help and accompany in my life. We were not only able to support each other, but also happy by talking about things other than work.

Thank you very much, everyone!

Hao Liu

Hannover, Oct. 10th, 2018.